

# RegClim

## Regional Climate Development Under Global Warming

*General Technical Report No. 7*

Presentations from Spring Seminar  
15 - 16 May 2003, Oslo, Norway

Edited by Trond Iversen and Magne Lystad



Institute of  
Marine  
Research



Nansen Environmental  
and Remote Sensing  
Center



University  
of Bergen



University  
of Oslo



Norwegian  
Meteorological Institute  
*met.no*

## Contents

	Page
<b>Full names and addresses of participating institutions</b> .....	<b>2</b>
<b>Names and e-mail addresses of central personnel</b> .....	<b>3</b>
<b>Preface, by Trond Iversen</b> .....	<b>5</b>
<b>Presentations</b> .....	<b>7</b>
Simulation of the Eemian interglacial with the coupled ocean-atmosphere circulation model ECHO-G, by F. Kaspar, U. Cubasch, S. Lorenz .....	<b>9</b>
Evaluation of MPI and Hadley simulations with HIRHAM and sensitivity to integration domains, by Jan Erik Haugen and Viel Ødegaard .....	<b>19</b>
An evaluation of the most recent A2 and B2 climate scenarios from various GCMs, by Rasmus E. Benestad .....	<b>31</b>
Change in annual and seasonal runoff in Norway in a scenario period compared to a control period, by Torill Engen Skaugen .....	<b>39</b>
Adapting the Regional Ocean Model System for dynamic downscaling, by Bjørn Ådlandsvik and W. Paul Budgell .....	<b>49</b>
Improvements in the sea ice module of the regional coupled atmosphere-ice-ocean model and the strategy and method for the coupling of the three spheres, by Jens Debernard, Morten Ødegaard Køltzow, Jan Erik Haugen and Lars Petter Røed .....	<b>59</b>
Parameterization of sea ice albedo in climate models, by Morten Køltzow .....	<b>71</b>
Regional Uncertainties in Climate Projections due to Sensitivity of the Atlantic Meridional Overturning Circulation (AMOC), by Asgeir Sorteberg, Helge Drange and Nils Gunnar Kvamstø .....	<b>77</b>
Climate response to anthropogenic aerosol forcing using the Oslo version of NCAR CCM3 coupled to a slab ocean, by Jón Egill Kristjánsson, Trond Iversen, Alf Kirkevåg, Øyvind Seland, Jens Debernard, Lars Petter Røed .....	<b>93</b>
Optimal Forcing Perturbations for the Atmosphere, by Trond Iversen, Jan Barkmeijer and Tim N. Palmer .....	<b>107</b>
<b>Appendix A Seminar Programme</b> .....	<b>137</b>
<b>Appendix B List of Participants</b> .....	<b>143</b>

**Full names and addresses of participating institutions**

- met.no : Norwegian Meteorological Institute  
P.O. Box 43 Blindern  
N-0313 OSLO  
NORWAY
- Gfi-UiB : Geophysical Institute  
University of Bergen  
Allégt. 70  
N-5007 BERGEN  
NORWAY
- IfG-UiO : Department of Geosciences  
University of Oslo  
P.O. Box 1022 Blindern  
N-0315 OSLO  
NORWAY
- IMR : Institute of Marine Research  
P.O. Box 1870 Nordnes  
N-5024 BERGEN  
NORWAY
- NERSC : Nansen Environmental and Remote Sensing Center  
Edv. Griegsvei 3A  
N-5037 SOLHEIMSVIKEN  
NORWAY

**For questions regarding the project, please contact:**

Magne Lystad  
Norwegian Meteorological Institute  
P.O. Box 43 Blindern  
N-0313 OSLO  
Phone: +47 22 96 33 23  
Fax: +47 22 69 63 55  
e-mail: magne.lystad@met.no

## Names and e-mail addresses of central personnel in RegClim Phase III|

### Project management group:

### E-mail address:

#### Leaders:

Trond Iversen, IfG-UiO  
 Sigbjørn Grønås, Gfi-UiB  
 Eivind A. Martinsen, met.no

trond.iversen@geo.uio.no  
 sigbjorn@gfi.uib.no  
 eivind.martinsen@met.no

#### Scientific secretary:

Magne Lystad, met.no

magne.lystad@met.no

#### Principal investigators:

**PM1** Eirik Førland

eirik.forland@met.no

**PM2** Bjørn Ådlandsvik

bjorn@imr.no

**PM3** Nils Gunnar Kvamstø

nilsg@gfi.uib.no

**PM4** Jon Egill Kristjansson

j.e.kristjansson@geo.uio.no

**PM5** Trond Iversen

trond.iversen@geo.uio.no

#### Contact person at NERSC:

Helge Drange

helge.drange@nersc.no



## **Preface**

*Trond Iversen*

*Project leader of RegClim Phase III*

The 2003 spring seminar of RegClim took place 15.-16. May at the University of Oslo, Norway. This was the first meeting in Phase III of the project, and our external advisors. Prof. Erland Källén, MISU, Stockholm and Prof. Ulrich Cubasch were present. We also had visitors from our Nordic colleagues at the Rosby Centre (SMHI), from the Danish Climate Centre (DMI), and from the Finnish Meteorological Institute (FMI). The meeting followed immediately after a workshop for the Nordic RESMoNA-project (Regional Earth System Modelling Network for the Arctic). Several RegClim-papers were also presented at that workshop.

Phase III started on January 1<sup>st</sup> 2003, as a continuation of earlier RegClim-phases initiated in the autumn 1997. The project has in earlier phases been a characteristic pioneering activity, or rather an ensemble of pioneering activities, in Norway. Competence on climate modelling has been built up both globally and regionally, and there have been periods with trial and error. Nevertheless, important results have come out of the project, both in the form of data that are applicable in impact studies, in the form of improved understanding and perception of the climate system, and in the form of powerful modelling tools that can be further utilized in RegClim and in other projects and activities.

RegClim Phase III is therefore a much more focused project than earlier phases. And in the main focus is “risk and uncertainties”. With risks we mean changes in the probabilities of weather events, and we mean risks of climate developments that may occur in our region in particular and for which present global climate models are uncertain. Uncertainty in RegClim therefore reflects such regional processes in particular, in addition to sampling uncertainty due to natural internal variability in the climate system. Two types of uncertain processes in climate models are addressed: processes in the North Atlantic Ocean and in the Arctic; and aerosol-cloud-radiation interactions.

The presentations at the spring workshop by RegClim scientists all addressed different aspects of the risk-and-uncertainties issue. In addition an interesting presentation by Ulrich Cubasch on paleoclimatic modelling (the Eemian interglacial) was presented. All presentations are included in this report. Some of the papers are intended for publication and should therefore not be cited and quoted until further notice.

Oslo, Norway

November 2003

Trond Iversen

Project Leader of RegClim

# **Presentations**



# **Simulation of the Eemian interglacial with the coupled ocean-atmosphere circulation model ECHO-G**

by

**F. Kaspar<sup>1</sup>, U. Cubasch<sup>2</sup>, S. Lorenz<sup>1</sup>**

<sup>1</sup>: Max-Planck-Institute for Meteorology, Model and Data Group, Hamburg, Germany

<sup>2</sup>: Institute for Meteorology, Freie Universität Berlin, Germany

## **ABSTRACT**

A coupled ocean-atmosphere climate model was used to study the response of the climate system to orbitally induced changes in insolation during and at the end of the Eemian interglacial, which was the last interglacial before the present one. Simulations have been performed for 125,000 years and 115,000 years before present (BP). These dates represent maximum and minimum summer insolation on the northern hemisphere. In the simulation for 125,000 years BP the model responds with an amplification of seasonal temperatures. A comparison with reconstructed data shows a remarkable agreement particularly in the data-rich regions. In the simulation for 115,000 years BP a significant cooling of the northern hemisphere can be observed combined with a long-term increase in sea ice coverage.

## 1. Introduction

On a long-term timescale, climate variations are believed to be driven by changes in insolation as a result of variations in Earth's orbit around the sun. An interglacial is an uninterrupted warm interval during which global climate reaches at least the pre-industrial level of the global mean temperature (Berger and Loutre, 2002). The coupled ocean atmosphere model ECHO-G has been used to simulate the climate during and at the end of the last interglacial (Eemian). Orbital parameters and greenhouse gas concentrations have been adapted to conditions at 125 kaBP and 115 kaBP.

The zone centered on 65° North is generally considered to be of great importance in the mechanism of ice sheet growth (Bradley, 1999). The selected dates represent periods with maximum and minimum summer insolation in that zone. The last warm phase with low ice volume seen in marine isotopes (sub stage MIS 5e) peaked at 125 kyBP. It is assumed that this episode is linked to the Eemian warm stage observed in European land data (Kukla, 2000).

The disappearance of forests all over Europe that is seen in the data between 115 kyBP and 117 kyBP supports the assumption that this date marks the start of the last glacial (Kukla, 2000).

## 2. The model

The ECHO-G model (Legutke and Voss, 1999; Legutke et al., 1999) consists of the ECHAM4 atmosphere model (Roeckner et al., 1992) coupled to the HOPE ocean model (Wolff et al., 1997). The atmospheric component is a spectral model with a horizontal resolution given by a triangular truncation at zonal wave number 30 (T30) which is transformed into a Gaussian grid of about 3.75°, and a vertical hybrid  $\sigma$ -p coordinate system with 19 levels. The ocean model operates on a T42 Arakawa E-Grid (approx. 2.8°). The resolution increases towards the equator to 0.5° in order to be able to simulate the ENSO events. The atmospheric and oceanic components are coupled with a flux correction in order to minimize a climate drift of the coupled system away from the climatologies of the uncoupled models.

The model has been used in a number of studies, e.g. to examine the influence of anthropogenic changes of greenhouse gases. It was also used in the simulation of the last 500 years with special focus on the “Late Maunder Minimum” (Fischer-Bruns et al., 2002). In their study the model was forced by solar variability, volcanism and greenhouse gases.

### 3. Boundary conditions

Three simulations have been performed with modified orbital parameters and greenhouse gas concentrations. They represent conditions of 125 kyBP, 115 kyBP and pre-industrial times. Orbital parameters are calculated following Berger (1978); data for greenhouse gas concentrations (CO<sub>2</sub>, CH<sub>4</sub>, N<sub>2</sub>O) are based on Vostok ice cores (Petit et al., 1999; Sowers, 2001). Table 1 shows the values of the parameters. The differences in the concentration of the greenhouse gases are small and it can be assumed that they do not have a relevant impact on the results. Therefore the only significant difference between the simulations are the orbital parameters.

Figure 1 illustrate the distribution of insolation over latitudes and seasons for 125 kyBP and 115 kyBP. At 125 kyBP significantly higher insolation than today occurred in the northern hemisphere in summer, while it is smaller in winter. The combined effect of greater obliquity and eccentricity, together with the fact that perihelion occurred in northern hemisphere summer caused an amplification of the seasonal cycle of insolation. At 115 kyBP the summer insolation is significantly lower than today (figure 1 (right)). The overall annual solar radiation received by the earth does not change significantly between both dates. For all the

	125 ky BP	115 ky BP	pre-indust.
Eccentricity	0.0400	0.0414	0.0167
Obliquity	23.79	22.41	23.44
Precession	127.3	290.9	282.7
CO <sub>2</sub> conc.	270 ppm	265 ppm	280 ppm
CH <sub>4</sub> conc.	630 ppb	520 ppb	700 ppb
N <sub>2</sub> O conc.	260 ppb	270 ppb	265 ppb

**Table 1:** Orbital parameters and greenhouse gas concentrations of the simulation runs. Orbital parameters are calculated following Berger (1978). Greenhouse gas concentrations are based on Vostok ice cores (CO<sub>2</sub> and CH<sub>4</sub>: Petit et al. (1999); N<sub>2</sub>O: Sowers (2001))

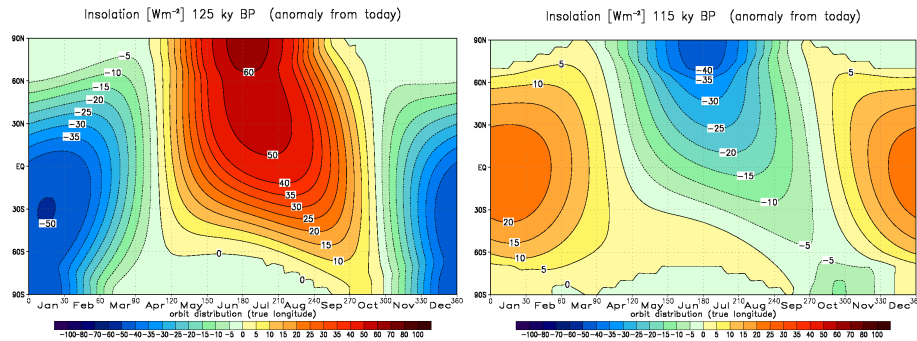


**Figure 1:** Insolation at 125,000 years BP (left) and 115,000 years BP (right) plotted as anomalies from today [ $\text{W}/\text{m}^2$ ]. At 125 kyBP amplified seasons with enhanced summer insolation occurred on the northern hemisphere. At 115 kyBP northern hemisphere's summer insolation was lower than today.

remaining boundary conditions present-day conditions are used.

## 4. The model runs

### Stability of the simulations

The 125 kyBP run started from conditions of an equilibrium run for current climatic conditions and was integrated over 2000 years. After approximately 1000 years the simulation became stable (e.g. quasi-stationary with respect to oceanic overturning circulation and sea ice extent). The year 1000 of the 125 kyBP simulation was used as initial state of the 115 kyBP simulation. In that run the oceanic circulation is stabilizing after approximately 800 years, but sea ice is still increasing after 1800 years (see figure 4).

### Temperature in the 125 kyBP simulation

In the 125 kyBP simulation the model responds with a warmer mean climate than in the pre-industrial simulation. In figure 2 (upper part) average January and July temperatures have been calculated for a period of 50 years and the simulated pre-industrial values have been subtracted. The period starts with year 1200 of the simulation. The selection of a different period does not have a significant impact on the results.

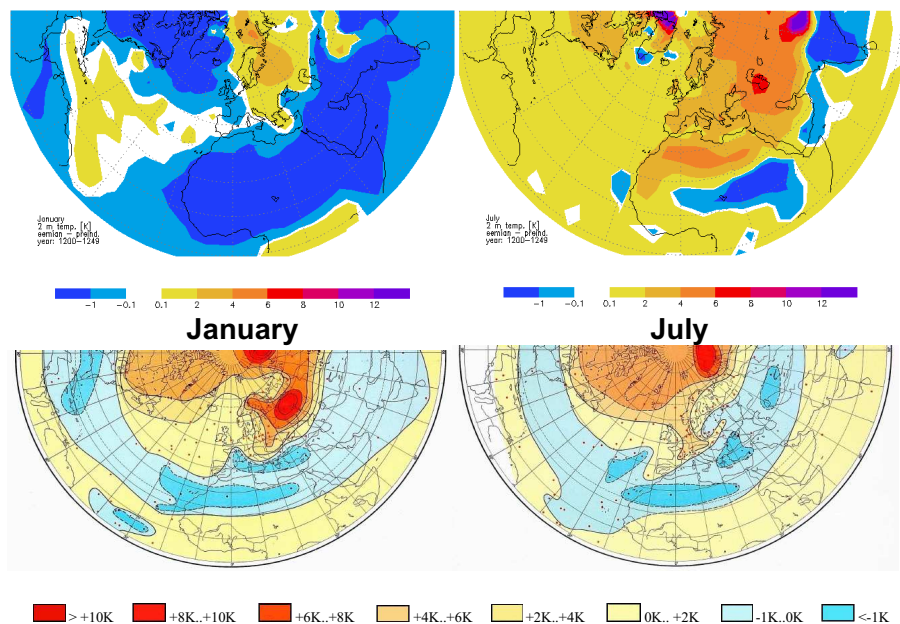


**Figure 2:** Simulated and reconstructed Eemian temperatures of the northern hemisphere (left: January, right: July). The simulation has been performed with the ECHO-G model with orbital parameters adapted to the values of 125 kyBP. The near-surface temperature is shown as difference to pre-industrial values (upper part of the figure). The lower part of the figure shows reconstructed temperatures according to Velichko et al. (1992). The values refer to the ‘last interglacial’ and are plotted as anomalies from today.

The figure shows that the seasons are intensified on large parts of the northern hemisphere. The summer temperature is higher especially over the continents, values greater than +4°C are reached over large areas of Asia. A belt with cooler temperatures at 20°N over Africa and Asia occurs which is related to increased precipitation. The winter temperature is lower over the continents with the exception of the area between Eastern Europe to Siberia, where higher temperature prevail. This reflects changes of sea ice in the Arctic Sea.

The lower part of figure 2 shows the reconstructed temperatures according to Velichko et al. (1992). These maps of the northern hemisphere are based on data from land and the deep sea. On land the reconstructions are derived from fossil plants. In the oceanic regions planktonic foraminifera have been used. Approximately 100 data sites were available for the construction of each map. The density of data sites is highest in Europe, the North Atlantic and the North

East Pacific. In summer positive anomalies can be seen in similar areas (circumpolar, including high and mid-latitudes) as in the simulation. A latitudinal belt with negative anomalies occurs in the reconstruction as well as in the simulation, but is located at higher latitudes in the reconstructed data. A possible explanation for this difference is the prescribed vegetation of the model. Additional vegetation in the Sahara might lead to enhanced precipitation and consequently to lower temperatures.

Reconstructed and simulated winter temperature anomalies are in good agreement over Europe, Asia and Africa (left part of figure 2). Over North America simulated and reconstructed winter anomalies have opposite sign, but for this area the reconstruction is based on a very limited number of samples.

Abundances of pollen have been used to reconstruct the temperature for different phases of the Eemian (Kühl, 2003) with a method based on probability density functions over Europe in the Corylus and the Carpinus phase. The Corylus phase is thought to represent the period of the insolation maximum and should therefore be used for the comparison with the simulation results. The January temperature anomaly shows a west-east gradient over Europe, with negative anomalies in France and Britain towards increasing positive anomalies in the area of Germany, Poland and Scandinavia. A similar gradient occurs in the simulation results. Reconstructed temperature anomalies for July are positive on large areas over Europe with some exceptions in the south. The simulated anomaly is almost homogeneously positive over Europe and therefore also in acceptable agreement with these reconstructions.

### **The 115 kyBP Simulation**

The Simulation for 115 kyBP shows a long term cooling trend, that is still visible after 1800 years of simulation. Figure 3 shows temperature anomalies of that simulation. Again the average of 50 years has been calculated for the summer months and pre-industrial values have been subtracted. With the exception of very limited areas temperature anomalies are negative, especially on the continental areas of the northern hemisphere. In the higher northern latitudes anomalies of more than  $-10^{\circ}\text{C}$  occur over the land areas. This cooling trend is related with continuously increasing sea ice volume as illustrated in figure 4. This behavior is consistent

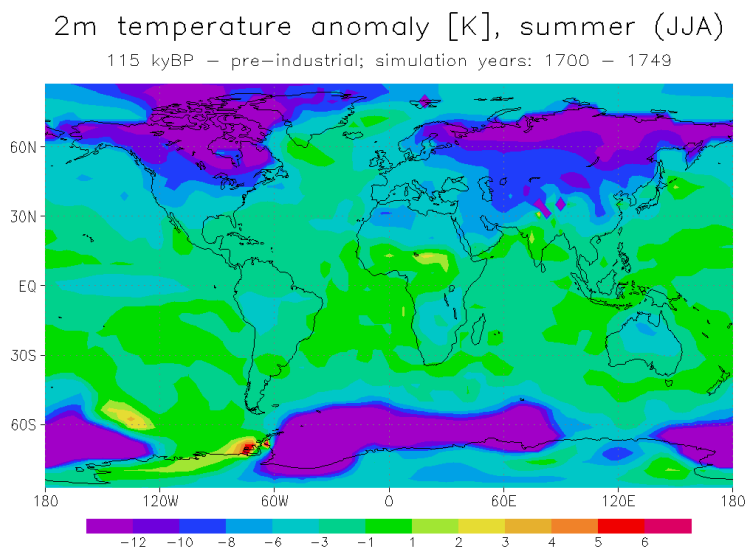


**Figure 3:** Difference in near surface summer temperature between the 115 kyBP and the pre-industrial simulation. The summer months have been averaged over 50 years (1700 years after the start of each simulation).

with the assumption that this date marks approximately the start of the glacial. At the current stage of the simulation (1800 years) the North American continent still remains free of snow in the summer months. The constant vegetation cover of the model might be responsible for this effect. The increase of albedo due to snow is lower in forest areas than in open landscapes. Therefore a modification of the vegetation might lead to an additional cooling. This will be investigated in additional experiments.

## 5. Discussion and conclusion

The comparison of simulated temperature anomalies for 125 kyBP with reconstructions of the northern hemisphere showed that they agree over wide areas. Especially over Europe, where the reconstructions are based on the highest density of data sites, modeled winter and summer anomalies are both in good agreement with the data. Therefore we can conclude that insolation change due to orbital variation is the most relevant driving force.

Inconsistencies between modeled and reconstructed data might be caused by an insufficient data coverage, or by a missing representations of feedback mechanisms in the model. One possibility is

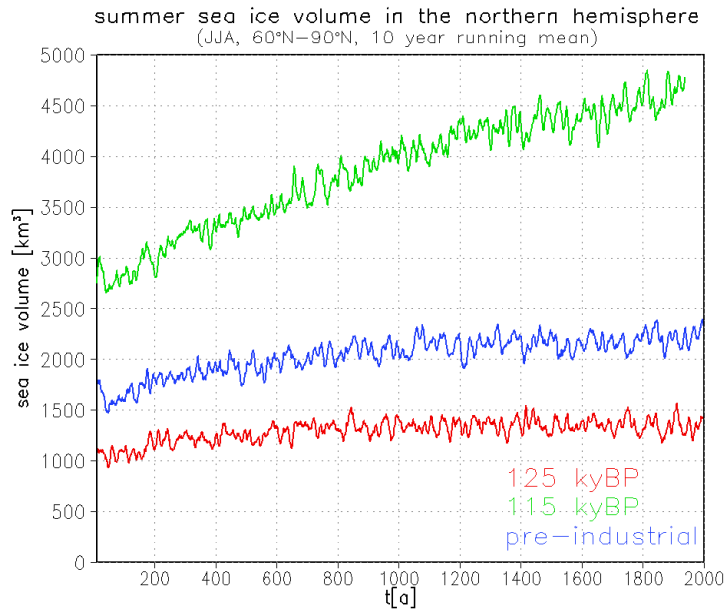


**Figure 4:** Change in summer sea ice volume in the high latitudes of the northern hemisphere. The values are 10-year averages over the latitudes 60°N-90°N.

the lack of a dynamical vegetation, an assumption supported by the study of Harrison et al. (1995), who calculated substantial changes in biome distribution for the last interglacial.

In the 115 kyBP simulation the modified insolation leads to a long-term cooling trend that is consistent with the assumption that the glacial inception at that time.

## Acknowledgement

This work has been performed within the framework of the ongoing DEKLIM-EEM project, which is financially supported by the German Ministry for Education and Research (BMBF). The simulations were run at the German Climate Computing Center (DKRZ, Hamburg).

## References

- Berger, A. L. (1978): Long-term variations of daily insolation and Quaternary climate changes. *Journal of Atmospheric Science*, **35**, 2362-2367.
- Berger, A. L.; Loutre, M. F. (2002): An exceptionally long interglacial ahead? *Science*, **297**, 1287-1288.

- Bradley, R. S. (1999): *Paleoclimatology – Reconstructing climates of the Quaternary*. Second Edition. International Geophysics Series **68**. Harcourt Academic Press, San Diego.
- Fischer-Bruns, I.; Cubasch, U.; von Storch, H.; Zorita, E.; Gonzales-Ruoco, F.; Luterbacher, J. (2002): Modelling the Late Maunder Minimum with a 3-dimensional OAGCM. RegClim – General Technical Report No. **6**, Oslo, Norway.
- Harrison, S. P.; Kutzbach, J. E.; Prentice, I. C.; Behling, P. J.; Sykes, M. T. (1995): The response of northern hemisphere extratropical climate and vegetation to orbitally induced changes in insolation during last interglaciation. *Quaternary Research*, **43**, 174-184.
- Kühl, N. (2003): Die Bestimmung botanisch-klimatologischer Transferfunktionen und die Rekonstruktion des bodennahen Klimazustandes in Europa während der Eem-Warmzeit. *Dissertationes Botanicae* **375**.
- Kukla, G. J. (2000): The last interglacial. *Science*, **287**, 987-988.
- Legutke, S.; Maier-Reimer, E. (1999): Climatology of the HOPE-G Global Ocean - Sea Ice General Circulation Model, Technical Report **21**, DKRZ, Hamburg, Germany.
- Legutke, S.; Voss, R. (1999): The Hamburg Atmosphere-Ocean Coupled Circulation Model ECHO-G. Technical Report **18**, DKRZ, Hamburg, Germany (available at: <http://www.dkrz.de/forschung/reports.html>)
- Petit, J. R.; Jouzel, J.; Raynaud, D.; Barkov, N. I.; Barnola, J. M.; Basile, I.; Bender, M.; Chappellaz, J.; Davis, J.; Delaygue, G.; Delmotte, M.; Kotlyakov, V. M.; Legrand, M.; Lipenkov, V. M.; Lorius, C.; Pépin, L.; Ritz, C.; Saltzman, E.; Stievenard, M. (1999): Climate and atmospheric history of the past 420,000 years from the Vostok ice core – Antarctica. *Nature*, **399**, 429-436.
- Roeckner, E.; Arpe, K.; Bengtsson, L.; Brinkop, S.; Dümenil, L.; Esch, M.; Kirk, E.; Lunkeit, F.; Ponater, M.; Rockel, B.; Sausen, R.; Schlese, U.; Schubert, S.; Windelband, M. (1992): Simulation of the present-day climate with the ECHAM model: Impact of model physics and resolution. Report No. **93**, Max-Planck-Institute for Meteorology, Hamburg, Germany.
- Sower, T. (2001): N<sub>2</sub>O record spanning the penultimate deglaciation from the Vostok ice core. *JGR atmospheres*, **106** (D23), 31,903-31,914
- Velichko, A. A.; Grichuk, V. P.; Gurtovaya, E. E.; Zelikson, E. M.; Barash, M. S.; Borisova, O. K. (1992): Climates during the last interglacial. In: Frenzel, B.; Pécsi, M.; Velichko, A. A. (1992): Atlas of paleoclimates and paleoenvironments of the northern hemisphere, Late pleistocene – holocene. Gustav Fischer Verlag, Stuttgart (data also available on <http://www.pangea.de/Projects/PKDB/PaleoAtlas.html>)
- Wolff, J.O.; Maier-Reimer, E.; Legutke, S. (1997): The Hamburg Ocean Primitive Equation Model HOPE, Technical Report No. **13**, DKRZ, Hamburg, Germany (available at: <http://www.dkrz.de/forschung/reports.html>)



# **Evaluation of MPI and Hadley simulations with HIRHAM and sensitivity to integration domains**

**by**

**Jan Erik Haugen and Viel Ødegaard**

Norwegian Meteorological Institute, Oslo

## **Abstract**

The simulations carried out with the HIRHAM regional climate model during RegClim are described and some results from recent work summarized. Sensitivity to the integration domain of HIRHAM has been carried out with the MPI IS92a and ERA-15 data. A first attempt to analyze the RegClim MPI IS92a results during phase I and II with the new Hadley A2 simulation in phase III has been made, where a scaling procedure according to the trend in surface temperature is applied.

## 1. Available HIRHAM simulations

During RegClim phase I and II, two main simulations were carried out with the HIRHAM regional climate model; a control run forced by ERA-15 data (ECMWF re-analyses 1979-1993) and a 70 year (1980-2049) climate change simulation forced by MPI GSDIO data (MPI ECHAM4/OPYC3 IS92a scenario run 1860-2050). They were all carried out for the largest HIRHAM domain in Fig.1 and with 55km horizontal resolution (and 19 vertical levels). Prescribed sea surface temperature and ice cover from the respective global data were used in both runs. Greenhouse gas concentrations in the MPI run were tabulated according to the IPCC IS92a data. A new feature of the MPI GSDIO run was that the forcing from aerosols (direct and indirect effects) was taken into account. Consequently, the global warming rate in this run was lower than in earlier MPI scenarios (and in the low end of available IPCC IS92a scenarios). In addition, this run also gave a quite realistic simulation of the present-day climate periods compared to other available global scenario runs. The presented results concerning expected regional climate change signals were mainly based on the HIRHAM data from the two time-slices 1980-1999 and 2030-2049 (2x20 years).

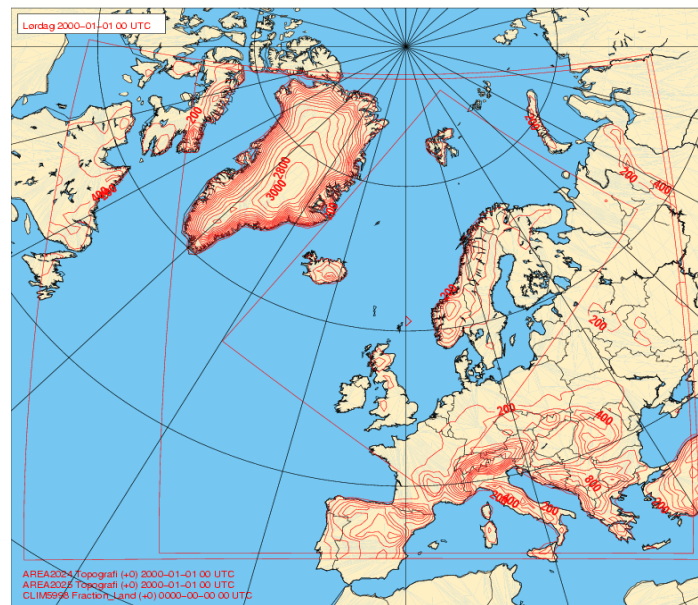


**Figure 1.** The 3 HIRHAM integration domains (named large, medium and small) used for 55km horizontal resolution (and 19 vertical levels) simulations with ERA-15 and MPI GSDIO data. The high-resolution (22km/31levels) domain overlaps with the smallest 55km domain. The contours display the height of the model orography for the 55km models.

During the last year a number of additional simulations have been carried out with the ERA-15 and MPI GSDIO data. The simulations were repeated for two smaller integration domains (medium and small), also shown in Fig. 1. This was motivated by the fact that the large scale circulation seemed not to be sufficiently controlled by the driving model and can be analyzed in terms of sensitivity to the choice of integration domain using the same regional climate model and identical forcing data. In addition, some of the simulations will form a reference for planned future high resolution repeated runs with the HIRHAM model.

Although a number of interesting results have been presented during RegClim phase I and II, the conclusions about regional climate signals have so far suffered from the fact that only one realization is available for a limited time period of 2x20 years. In particular, the natural variability is far from captured in these data, and the conclusions about expected changes in precipitation and surface wind are to some extent relatively insignificant compared to the variability in recent and present regional climate. In RegClim phase III, a number of new scenario runs will be carried out in order to focus on the uncertainty of the results from regional climate models and to quantify the risk of extremes in a future climate. So far, one additional run has been carried out on the small domain. The forcing data are the Hadley A2 scenario run (HadCM3). The time-slices are 1961-1990 and 2071-2100 (2x30 years). Although data for comparable time periods could benefit the analysis, the choice was made due to limited available data. However, there are indications that in some respects the differences between the global models are more significant than the actual time periods considered within each global simulation. A preliminary analysis to take into account the difference in time-slices is presented in the following section. In this section horizontal maps of the temperature and precipitation response during winter for the two simulations are shown in Fig. 2 and 3. The temperature response expressed in C/decade shows comparable rates over southern inland areas of Norway, a somewhat higher rate in coastal areas for the Hadley simulation except in Northern Norway and a general larger increase in northern areas for the MPI simulation closer to the ice border and the Arctic (with a general large variability in the expected response of global scenarios). The precipitation response, expressed in mm/day, shows some large-scale qualitative common features, e.g. large areas of increasing values in southern Scandinavia. However, for the winter precipitation response, there is quantitatively a large spread in the results from the two simulations. The reason is mainly due to differences in the large scale circulation patterns for the simulated periods, but may also partly be due to

differences in the global climate model or the ocean state.

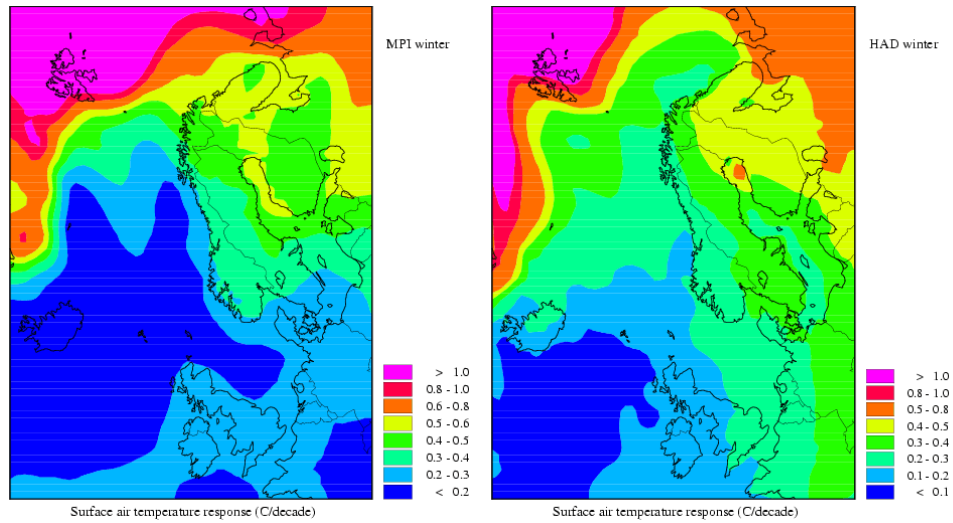


**Figure 2:** The surface temperature response during the winter from the HIRHAM simulations with the MPI IS92a (left) and Hadley A2 (right) data in unit °C/decade.

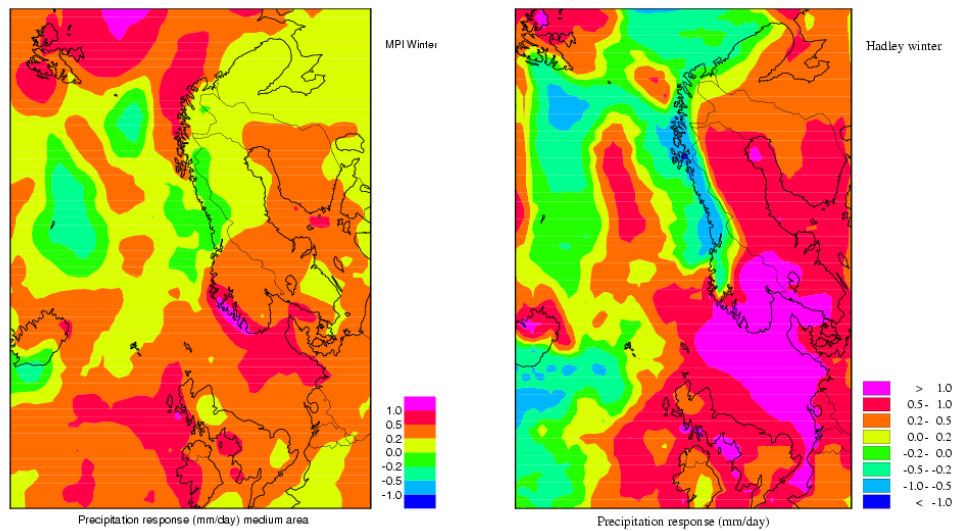


**Figure 3:** The precipitation response during the winter from the HIRHAM simulations with the MPI IS92a (up to year 2050) (left) and Hadley A2 (up to year 2100) (right) data in unit mm/day.

The use of different integration domains in HIRHAM for the MPI data showed a sensitivity in the regional response of e.g. the spatial distribution of the seasonal precipitation amounts. Relatively small systematic errors in the simulation of the North-Atlantic storm tracks consequently will influence the quantitative precipitation along the west-coast of Norway. This is a feature of both the global and regional models. The integration domain of the regional climate model should be chosen so that increased systematic errors in the storm tracks are avoided compared to the global data. We have so far not made any new recommendations concerning integration domain from the sensitivity tests. An example of sensitivity is shown in Figure 4 and 5. The winter precipitation in Fig. 4 for the ERA-15 simulation shows that the small domain is preferable, since the quantitative distribution is closer to the ECMWF values (daily 00UTC+24 hour forecasts). Some time series for the period Jan-Mar 1979 (average over Scandinavian sub-domain) in Fig. 5 show that with the medium area, the data cannot be compared from day to day with corresponding daily values, (in contrast with the small domains) and any analysis has to be based on frequency distributions and seasonal averages. A new development during phase III will be a higher resolution HIRHAM model, tentatively with 22km horizontal resolution and 31 vertical levels. A one year integration from the ERA-15 period (1979) has been made, with only minor modifications in the physical parameterization compared with the lower resolution version. The result was included in Fig. 5 and the preliminary analysis shows that the low and high resolution daily values on the small domain are very similar. Further comparison with observations is needed for this simulation. The run was carried out with the present Eulerian semi-implicit time scheme, but we are opting for a two-time-level semi-Lagrangian advection scheme. Some preliminary results are available, but further development is needed before this version can be used for production runs.

## **2. Comparison of the scenarios from MPI and the Hadley center**

The results of the downscaling are analyzed on a monthly basis where the Norwegian land area is partitioned into five regions. The scope is to present a common analysis of the data. The regions are defined on the basis of model climate, which shows large variation over Norway, from inland to coast, from north to south and from the western to the eastern side of the mountains in southern Norway.

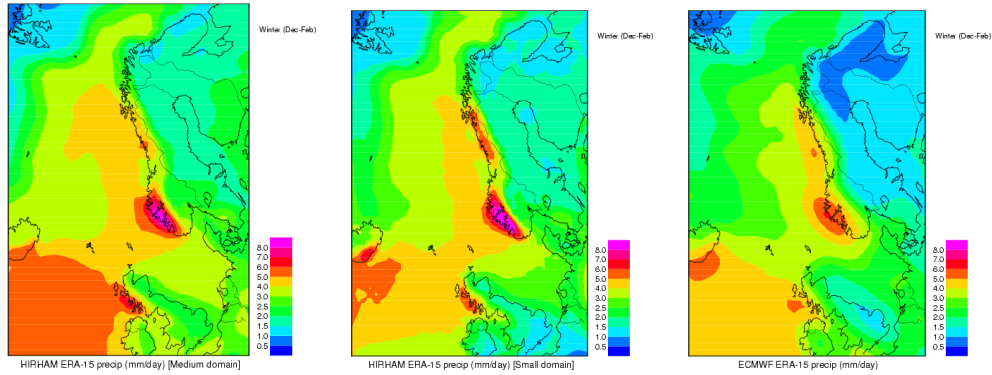


**Figure 4:** The winter precipitation in HIRHAM ERA-15 simulation in mm/day for the medium domain (left) and small domain (middle) compared to ECMWF ERA-15 (right).

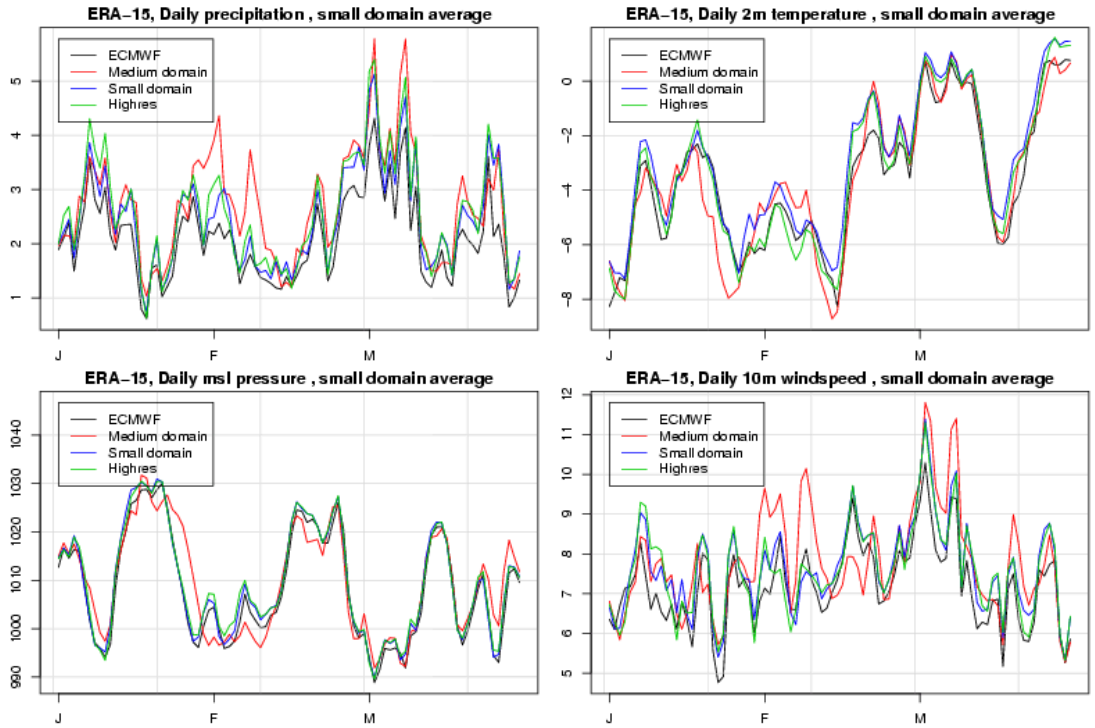


**Figure 5:** Comparison of daily HIRHAM output with ECMWF data for Jan-Mar 1979 ERA-15 data, average values over Scandinavian sub domain. The parameters are precipitation in mm/day (upper left), 2 meter temperature in °C (upper right), mean sea level pressure in hPa (lower left) and 10m wind speed in m/s (lower right). ECMWF values in black, HIRHAM values for medium, small and high resolution domain are shown in red, blue and green, respectively.

In order to compare the results valid for different time periods it has been suggested to scale the data from the Hadley simulations in time to the periods of the MPI simulations. The global 2m temperature tendency has been suggested (Christensen et al., 2001) as a scaling factor. The monthly tendencies of 2m temperature are compared between the regions and to tendencies in 10m wind speed and precipitation rate. The tendency in 2m temperature is positive in all regions and all months, but is highest in the winter and in the most northern regions. The tendencies in 10m wind speed and precipitation rate are close to zero and negative in some regions and some months. For example the tendencies are negative at the southern coastal region of western Norway from July to September (Figure 6). Therefore it was chosen to use the local monthly 2m temperature tendency as a scaling factor for the 2m temperature from the runs forced with the Hadley Center data, while precipitation rate and wind speed are kept non-scaled.

Negative tendencies in 10m wind force and precipitation rate are seen in the Hadley runs in August and September in the southern coastal region and in January in the northern coastal region corresponding to different mslp-patterns in the two scenarios. This is a part of the uncertainty in the simulations of future climate in Norway. For the variation to be described in terms of standard deviation we would like the monthly means to have a nearly normal distribution. This is unfortunately not the case, neither when looking at the separate data sets nor the combined data set. In particular when combining the simulations forced by the two different models we find that the frequency distribution of monthly mean precipitation rate is bi-modal in some regions and some months. Figure 8 shows the distribution of monthly means in August for each of the two downscaling simulations and the combination of them.

The mean and the variation of present and future climate in the simulations are therefore presented in terms of median and quantiles for each region. Common for the scenarios from the two downscaling simulations is a prediction of increased 2m temperature. The inter-quantile range of present and future 10m wind speed, 2m temperature and precipitation rate is larger in the winter months in all regions. The variation in data for future summer temperatures is larger than in corresponding data for present climate. Only results from the southern coastal region are shown (Figure 8).

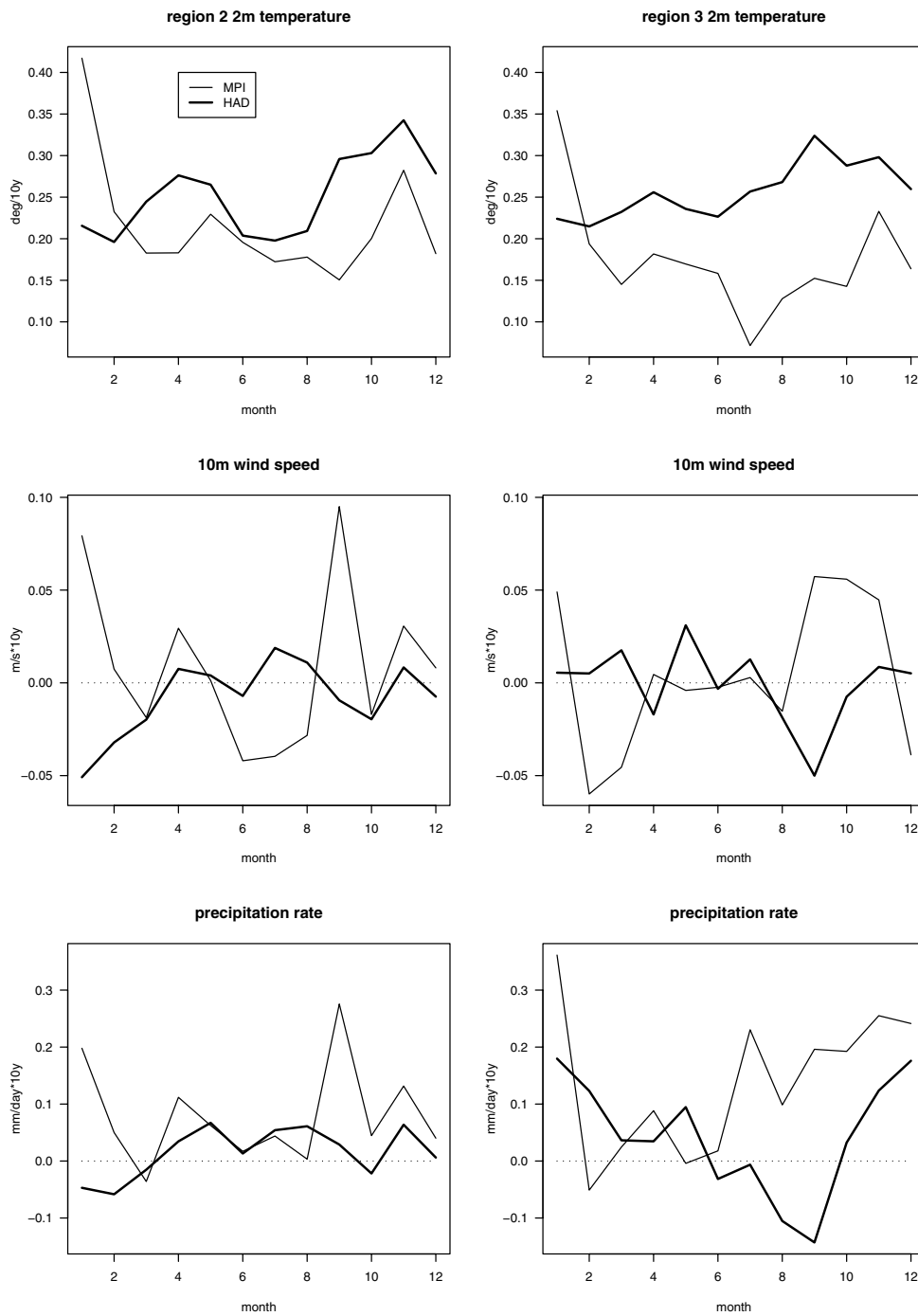


**Figure 6:** Monthly tendencies of 2m temperature, 10m wind speed and precipitation rate in HIRHAM forced by MPI and HadCM3 in region 2 (northern coastal area) and region 3 (southern coastal area).

### 3. Conclusions

Extending the results that have been presented during RegClim phase I and II with an additional HIRHAM simulation forced with HadCM3 has focused the fact that the natural variability is far from captured in these data. Even if a larger variability is predicted, expected changes in precipitation and surface wind from the different simulations are to some extent relatively insignificant compared to the variability in recent and present regional climate. The variation in present and future climate expressed in terms of means and quantiles is larger for 10m wind speed and precipitation rate than for 2m temperature. The result is particularly valid when we look into smaller regions. In RegClim phase III, a number of new scenario runs will be carried out in order to focus on the uncertainty of the results from regional climate models and to quantify the risk of extremes in a future climate.

### References

- Allen, M. R., P. A. Scott, J. F.B. Mitchell, R. Schnur, and Delworth, T. L., 2000: Quantifying the Uncertainty in Forecasts of Anthropogenic Climate Change', *Nature* **407**, 617-620.
- Bjørge, D., Haugen, J.E., and Nordeng, T.E., 2000: Future Climate in Norway. Dynamical Downscaling Experiments within the RegClim Project. DNMI Res. Rep. 103. Available from Norwegian Meteorological Institute, P.O. Box 43 Blindern, 0313 Oslo, Norway.
- Christensen, J. H. et al., 2001: A Synthesis of Regional Climate Change Simulations - A Scandinavian Perspective, *Geophys. Res. Lett.* **28**, 1003-1006.
- Haugen, J.E., D. Bjørge and Nordeng, T. E., 1999: A 20-year Climate Change Experiment with HIRHAM, using MPI Boundary Data, *RegClim Techn. Rep. No. 3*, 37-43. Available from NILU, P.O. Box 100, N-2007 Kjeller, Norway.

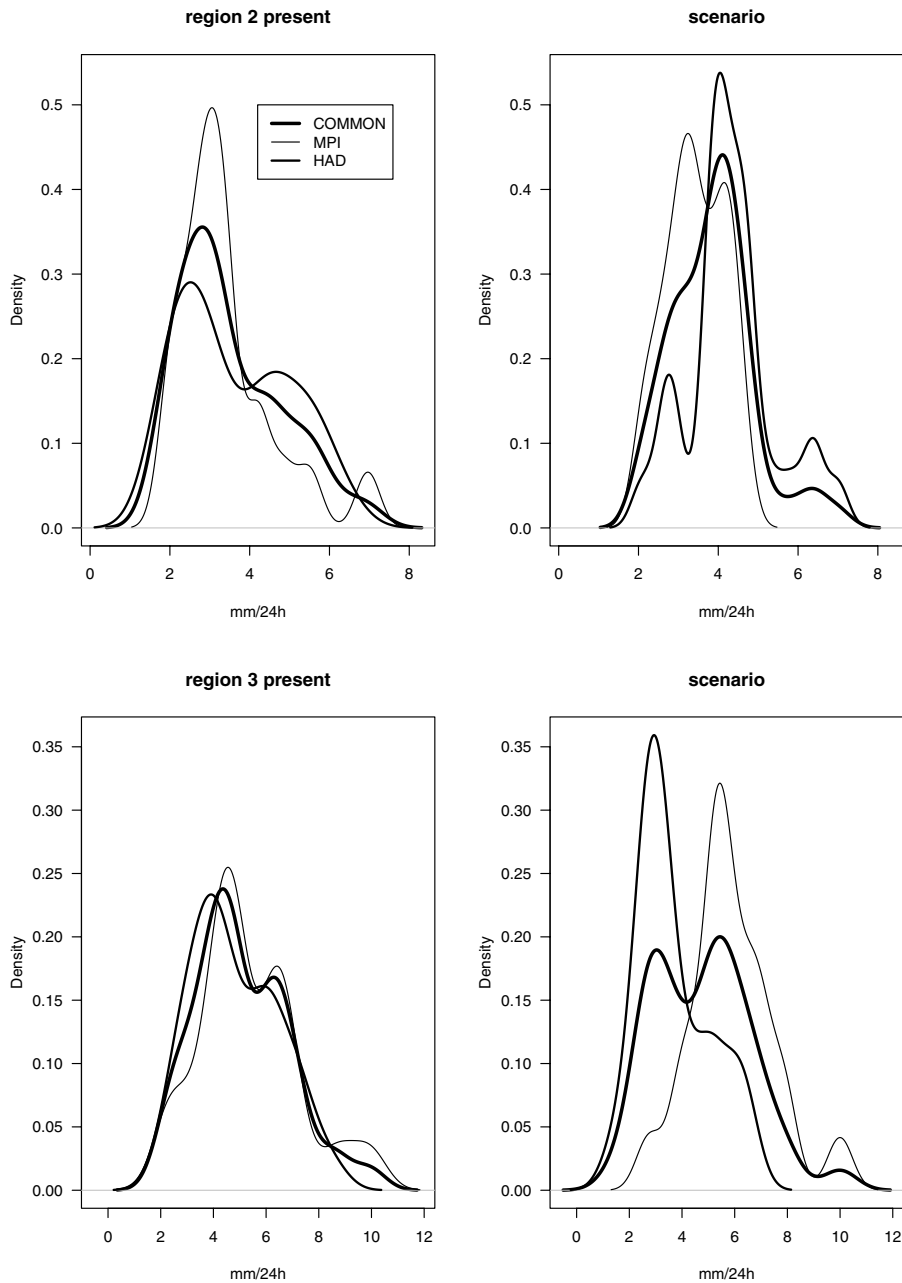


**Figure 7:** Distribution of precipitation amounts in HIRHAM forced by MPI and HADCM3 and common for both datasets, in region 2, northern coastal area (top) and region 3, southern coastal area (bottom). Left panels show distributions in present climate while right panels show distribution in future climate.

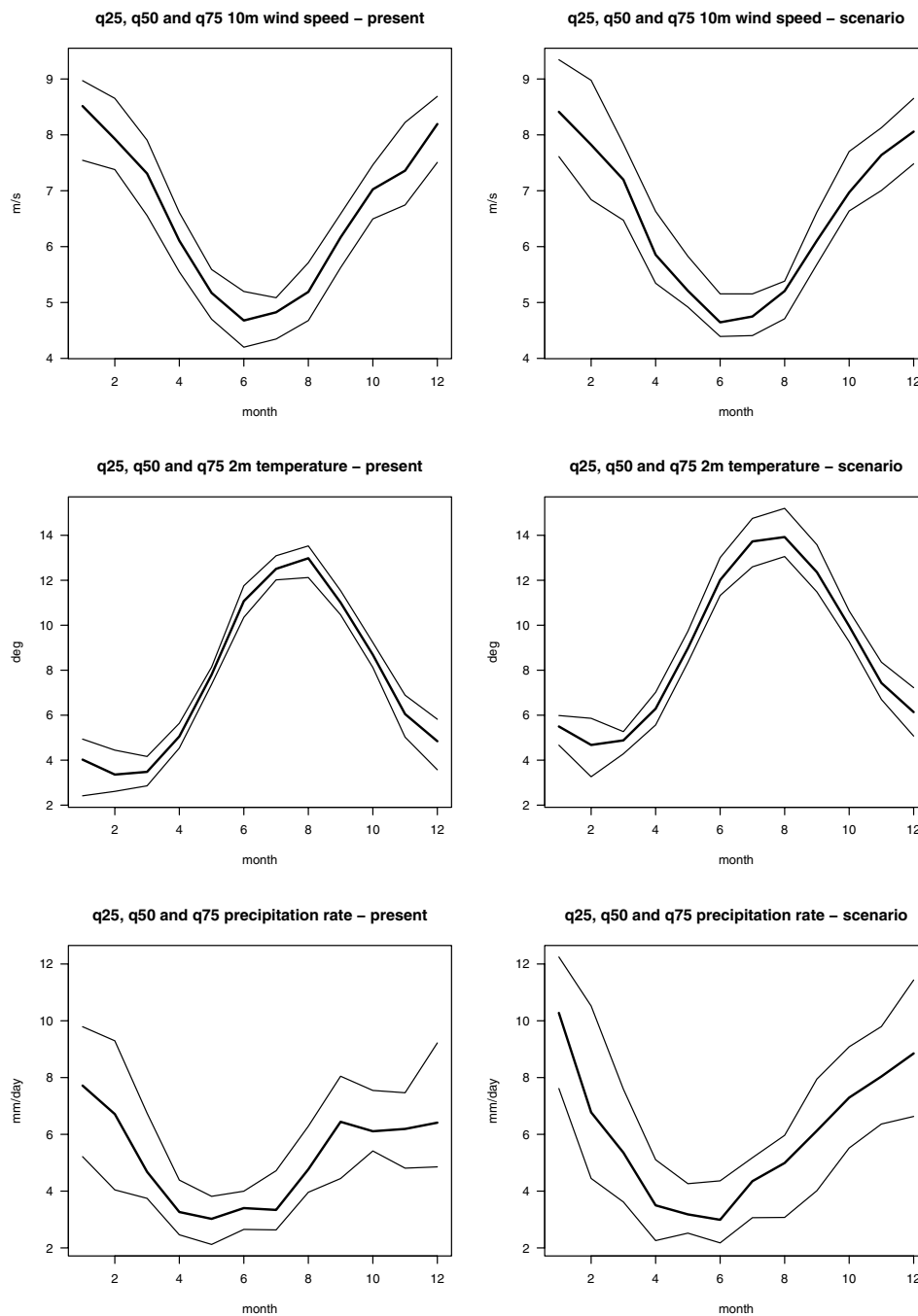


**Figure 8:** Median and quantiles of monthly means in the combined data from HIRHAM forced with MPI and HadCM3 for region3 (southern coastal area). Present climate left panels, scenarios right panels, top 10m wind speed, middle 2m temperature (HadCM3 scaled to MPI periods with the monthly and local temperature tendency) and bottom precipitation rate.



# An evaluation of the most recent A2 and B2 climate scenarios from various GCMs

by

**Rasmus E. Benestad**

Norwegian Meteorological Institute, Oslo

## 1. Introduction

In the new phase of the RegClim programme, the intention is to downscale several global climate models in order to obtain more reliable local and regional climate scenarios as well as assessing the uncertainties associated with these. The previous analysis will furthermore be repeated for the most recent global climate model (GCM) results that follow the Intergovernmental Panel on Climate Change (IPCC) emission scenarios: Special Report on Emissions Scenarios (SRES)<sup>1</sup>. In order to analyze the SRES-based climate scenarios, the data had to be retrieved and pre-processed. The preparation of the GCM data and a first-order quality control are described in Benestad (2003).

Before applying the downscaling analysis to the new GCM results, it is useful to examine the data directly.

## 2. Methods

The data were analyzed in a free-ware<sup>2</sup> software called R (R is a GNU version of Splus), and an R-package referred to as *clim.pact* (Benestad, 2003b,c) was used for making the plots. The trends in temperature and precipitation were computed through a regression against time (e.g. in R: `trend <- lm(y ~ x)`, where  $y$  is the T(2m) or precipitation record and  $x_i <- year_i + month_i/12 - year_1$  and  $i <- 1 \dots length(y)$ ). The EOF analysis adopted here is also known as common EOF analysis (Barnett, 1999), and involves a merging of anomalous SLP from four different GCMs (the mean is subtracted before merging the data, but the data was not detrended). The  $\chi^2$ -test was based on the formula for two binned data sets by Press *et al.* (1989):

---

<sup>1</sup><http://www.grida.no/climate/ipcc/emission/>

<sup>2</sup>Freely available from <http://cran.r-project.org/>

p. 517 equation 13.5.2. The 2D-space was divided into 9\*9 bins, for which a count of points falling into each was kept. The matrix describing the counts in the 9\*9 bins was transformed into a vector, on which the  $\chi^2$ -test was applied.

### 3. Results

Figure 1 shows the geographical distribution of the mean 2-metre temperature [T(2m)] and the precipitation from the results of the ECHAM4/OPYC3 model, for both the B2 and the A2 scenarios. These maps suggest that the GCM produces realistic results. Similar maps of the linear temperature trend are presented in Figures 2 and 3. For the period 2000-2049, the B2 scenario implies stronger warming than the A2 scenario (Figure 2), which at first sight may seem surprising. The explanation for the stronger warming in the B2 scenario for this time interval is that the A2 and B2 scenarios involve different descriptions for the aerosol loading, with greater aerosol loadings in the A2 scenario. The A2 scenario “catches up” with B2 after 2050, and Figure 3 shows that the warming over the 2000-2099 interval is stronger in A2.

The highest precipitation amounts in the GCM results are found in the tropics in the vicinity of the convergence zones (not shown) and the greatest changes in the rainfall are also associated with these weather systems. The precipitation trends in the tropics tend to swamp the extra-tropical trends, and in order to examine the GCM results for Nordic countries, the tropics should be excluded. Figure 4 shows maps of precipitation trends for the interval 2000-2049 for Europe. The ECHAM4/OPYC3 A2 and B2 scenarios indicate similar large-scale spatial patterns in the linear precipitation trends, with an increase over parts of the Norwegian Sea and Fennoscandia and a reduction in the vicinity of the Iberian Peninsula. For comparison, a similar analysis is shown for the HadCM3 results, and the picture is quite different: drier conditions over the Norwegian Sea and southern Norway and more precipitation over Spain in the course of the 2000-2049 period. The differences between the GCM results can be related to their description of the sea level pressure (SLP) (not shown). The ECHAM4/OPYC3-based scenarios tend to indicate a deepening of the SLP around Iceland, whereas the HadCM3 results suggest a weakening of the Iceland-Azores SLP dipole, e.g. higher SLP around Iceland and lower SLP over the Azores in the future. The differing accounts on the SLP evolution has been noted before (e.g. Benestad 2002), and it is important to keep in mind this spread when considering the uncertainty associated with the precipitation scenarios for the future. Furthermore, one cannot get a reliable scenario for the future

precipitation from one GCM alone. It is essential to improve our understanding of the physical processes relevant for the circulation patterns, and the North Atlantic Oscillation (NAO) and the Arctic Oscillation (AO) in particular. As long as there is a knowledge gap regarding the response of the atmospheric circulation patterns to climate change, one remedy is to use many GCMs and construct probability distributions for the precipitation trends. The temperature is less affected by the circulation pattern, and hence the multi-model ensemble shows a smaller spread.

Figure 5 shows a phase-space diagram of the large-scale atmospheric circulation patterns represented in terms of the two leading common EOFs for the January mean SLP from 4 different GCMs: CCCma, CSIRO, ECHAM4/OPYC3 and HadCM3. The results from NCAR-CSM were initially included, but the NCAR-CSM results gave bad results. The reason for why the NCAR-CSM being bad, is presumed to be related to the pre-processing of the NCAR-CSM data (i.e. conversion from the GRIB to netCDF format). The NCAR-CSM data were excluded for now, but the data will be examined in more detail and corrected later if it turns out that errors were introduced in the preparation of the data. This plot shows a joint distribution of the truncated 2D atmospheric state for each of the GCM, and the contours indicate the density of points for the four-GCM ensemble.

	CC 1	CC 2	CS 1	CS 2	EH 1	EH 2	HC 1	HC 2
CC 1	0	0.00	0.00	0.00	0.00	0.04	0.48	0.08
CC 2		0	0.00	0.00	0.08	0.29	0.94	0.40
CS 1			0	0.00	0.00	0.01	0.75	0.20
CS 2				0	0.00	0.01	0.28	0.08
EH 1					0	0.00	0.39	0.00
EH 2						0	0.26	0.00
HC 1							0	0.31
HC 2								0

**Table 1:** Probabilities associated with a  $\chi^2$ -test on the two-dimensional distribution of the points shown in Figure 5. Near-zero values indicate similar distribution. The CCCma model is referred to as 'CC', whereas 'CS' denotes CSIRO, 'EH' stands for ECHAM4/OPYC3, and 'HC' refers to HadCM3. The number after these acronyms refer to the intervals: '1'=2000-2049 and '2'= 2050-2099.

None of the GCMs indicated significant difference between the distribution in Figure 5 of the points for the two intervals 2000-2049 and 2050-2099, except for HadCM3. The distribution between the CCCma and CSIRO models were statistically similar. The CC 2 results were different to the corresponding ECHAM4/OY3, but all GCMs were different to the HadCM3

results for 2000-2049. It is interesting to note that the 2049-2099 distribution for HadCM3 is statistically similar to both the ECHAM4/OPYC3 distributions.

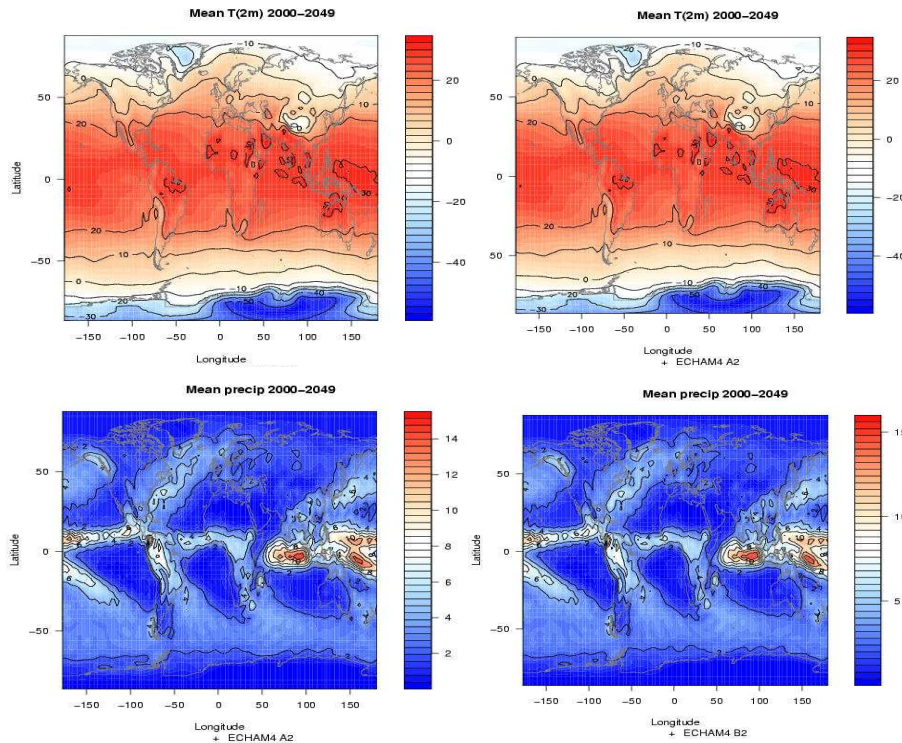


**Fig.1.** Maps of the 2000-2049 mean 2-metre temperature (upper) and precipitation from the ECHAM4/OPYC3 B2 and A2 SRES scenarios. Units: deg C and mm/day.

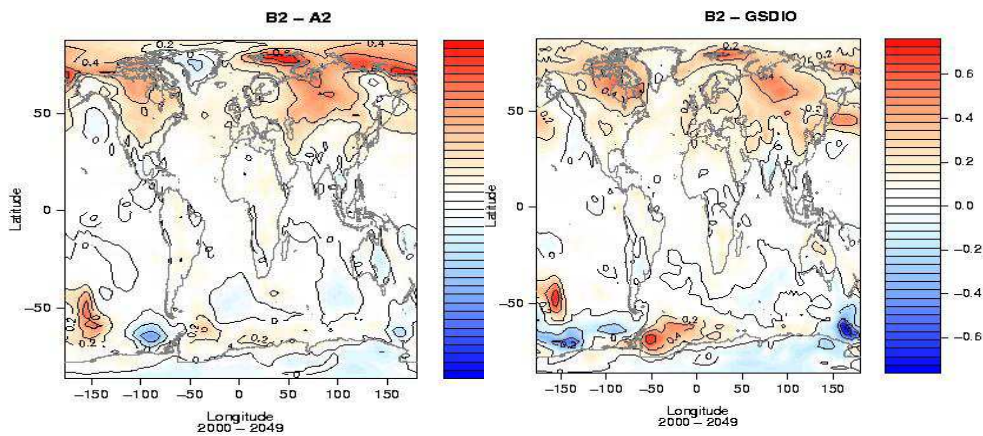


**Fig.2.** Maps of the differences between 2000-2049 trends in the 2-metre temperature from the ECHAM4/OPYC3 B2 and A2 and GSDIO scenarios respectively. Units: deg C/decade.

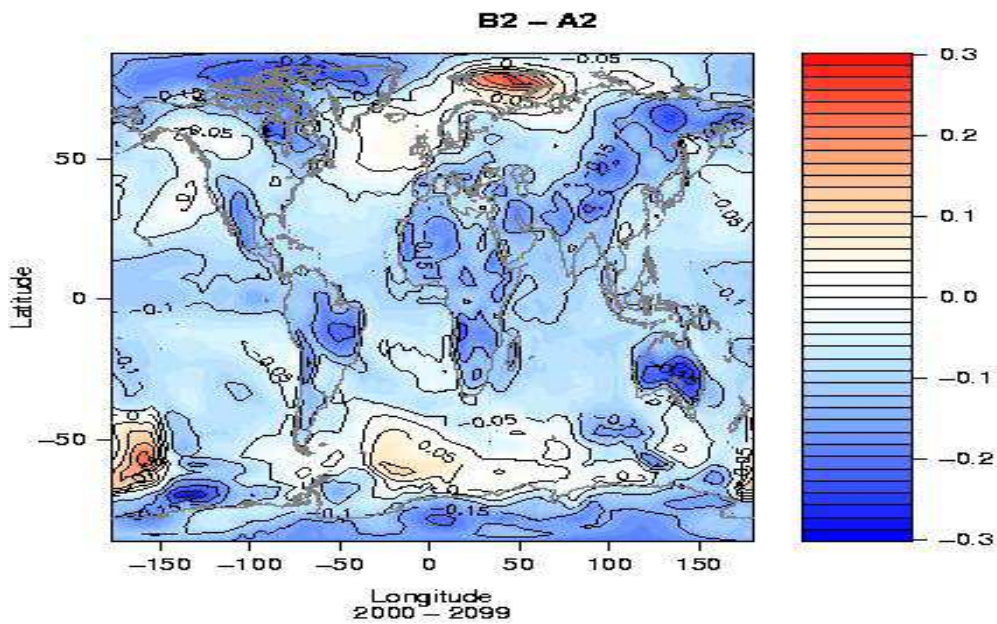


**Fig.3.** Map of the differences between 2000-2099 trends in the 2-metre temperature from the ECHAM4/OPYC3 B2 and A2 scenarios. Units: deg C/decade.

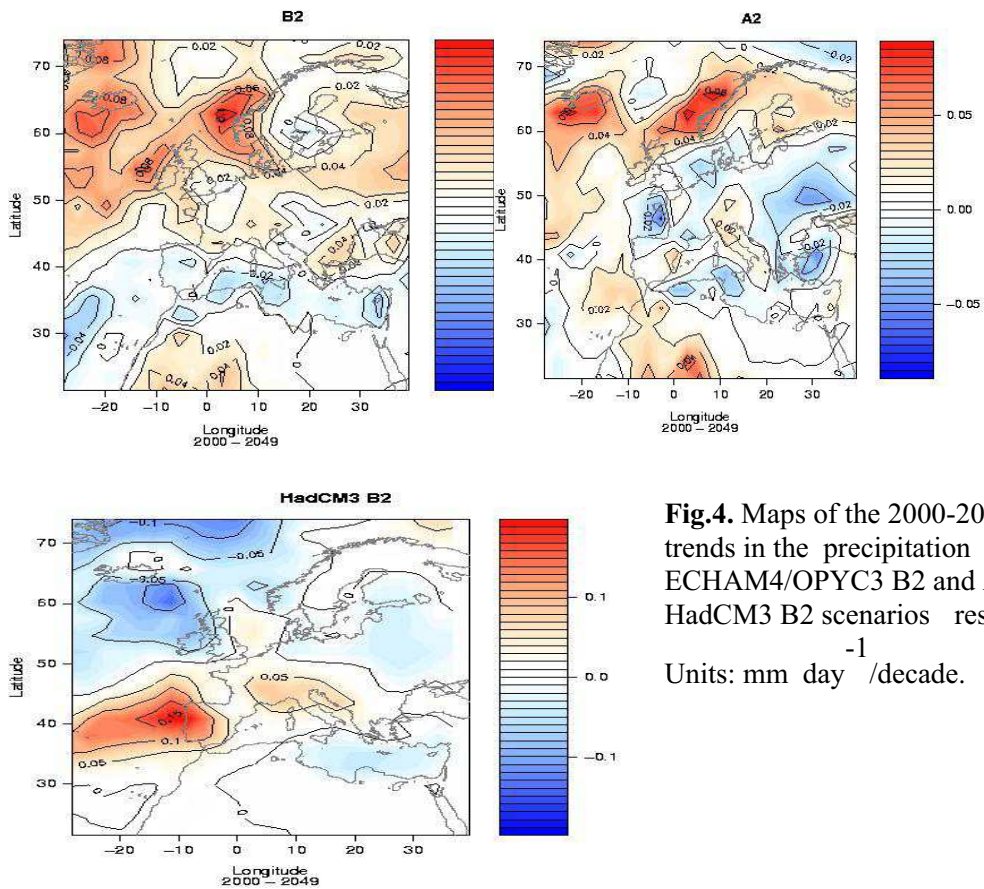


**Fig.4.** Maps of the 2000-2049 trends in the precipitation from the ECHAM4/OPYC3 B2 and A2 and HadCM3 B2 scenarios respectively. Units: mm day<sup>-1</sup>/decade.

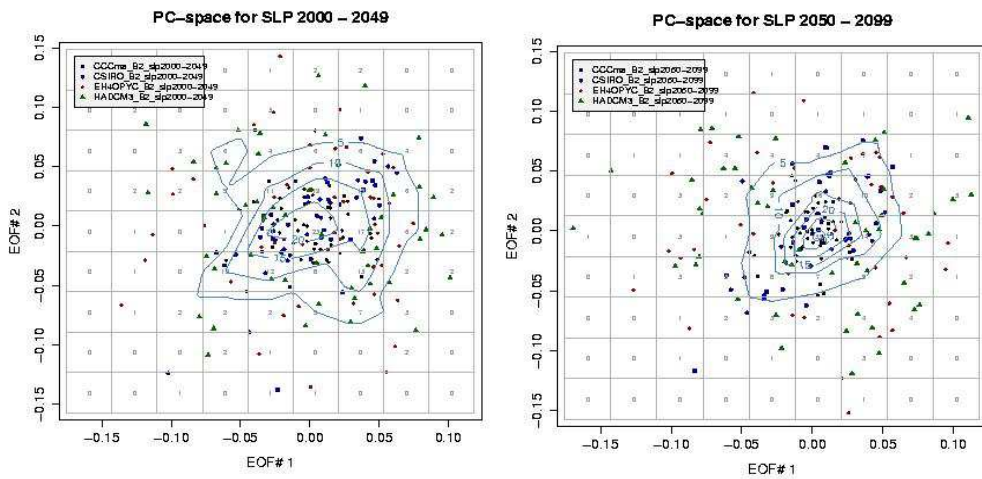


**Fig.5.** The dominating large-scale January mean circulation patterns represented by the two leading EOFs of the January mean SLP for four different GCMs: CCCma, CSIRO, ECHAM4/OPYC3 and HadCM3.

#### 4. Discussion and Conclusion

Inspection of the pre-processed SRES scenarios suggests that the GCMs in general can reproduce the known climatic features with a high degree of realism. The B2 scenario gives stronger initial warming due to different scenarios for aerosols, but the A2 scenario produces the strongest warming in the long run. The precipitation scenarios differ greatly amongst the GCMs because the various GCMs give different description of the future trends in SLP. Hence, the HadCM3 results indicate drier future conditions where the ECHAM4/OPYC3 points to wetter climates. For the two intervals 2000-2049 and 2050-2099, it is only the HadCM3 that suggests a statistical significant change in the large-scale circulation pattern described by the two leading SLP modes common for the four GCMs: CCCma, CSIRO, ECHAM4 and HadCM3. The clustering of SLP modes in the HadCM3 furthermore tends to differ to those of the other three models. The HadCM3 model is not flux corrected, whereas the other are. This may conceivably be one reason for why HadCM3 behaves differently to the others. Furthermore, the CCCma and CSIRO models have lower resolution than the ECHAM4/OPYC3 and HadCM3, one may speculate whether this explains why they give the most similar distributions in Table 1.

## Appendix

### Description of the SRES scenarios

The A2 scenario describes a “differentiated” world: The world “consolidates” into a series of economic regions. Self-reliance in terms of resources and less emphasis on economic, social, and cultural interactions between regions are characteristic for this future. Economic growth is uneven and the income gap between now-industrialized and developing parts of the world does not narrow.

The B2 story line assumes a world community with more concern for environmental and social sustainability than the A2 storyline. Increasingly, government policies and business strategies at the national and local levels are influenced by environmentally aware citizens. A trend toward local self-reliance and stronger communities is assumed. International institutions decline in importance, and there is a shift toward local and regional decision-making structures and institutions. Human welfare, equality, and environmental protection all have high priority, and they are addressed through community-based social solutions in addition to technical solutions, although implementation rates vary across regions.

### References

- Barnett, TP (1999) Comparison of Near-Surface Air Temperature Variability in 11 Coupled Global Climate Models, *Journal of Climate*, **12**, 511-518
- Benestad R.E. (2003) A first-order evaluation of climate outlooks based on the IPCC A2 and B2 SRES emission scenarios, met.no, KLIMA, 03/03, pp. 23
- Benestad R.E. (2003b) clim.pact-V1.0, met.no, KLIMA, 04/03, pp. 85
- Benestad R.E. (2003c) Downscaling analysis for daily and monthly values using clim.pact-V0.9, met.no, KLIMA, 01/03, pp. 45
- Benestad R.E. (2002), Empirically downscaled multi-model ensemble temperature and precipitation scenarios for Norway, *Journal of Climate* **Vol 15**, No. 21, 3008-3027.
- Gentleman R. and Ihaka R. (2000) Lexical Scope and Statistical Computing, *Journal of Computational and Graphical Statistics*, **9**, 491—508<sup>3</sup>

---

<sup>3</sup> <http://www.amstat.org/publications/jcgs/>

Press W.H., Flannery B.P., Teukolsky S.A and Vetterling W.T. (1989) Numerical Recipes in Pascal, *Cambridge University Press*

# **Change in annual and seasonal runoff in Norway in a scenario period compared to a control period**

**by**

**Torill Engen Skaugen**

Norwegian Meteorological Institute, P.O.Box 43 Blindern, N-0313 Oslo, Norway

## **Abstract**

Results from dynamical downscaled temperature and precipitation data from the AOGCM from Max-Planck institute in Hamburg (ECHAM4/OPYC3 with the GSDIO integration) are used as input in the HBV-model. Two modes of the HBV-model are available; the original catchment version and a gridded HBV version (the GWB model). The results are presented with the use of a spatial Geographical Information System (GIS).

Annual runoff is projected to increase all over Norway. Mean runoff along the coast is projected to increase most during winter. There will be a reduction in runoff during summer. At the inland area in southern Norway and at Finnmarksvidda, the runoff during spring is projected to increase. Mean runoff in autumn is projected to increase all over the country. Snow storage per 1st April is projected to increase in the high land. Evapotranspiration is projected to increase all over the country, and most along the coast.

## **1. Introduction**

Runoff is of large importance in Norway; power production is mainly based on hydropower (97 %). The hydropower basins are usually at the lowest regulated level in the spring, and at the highest regulated level in autumn (after snow melting and autumn rainfall). Changes in this regime may lead to changes in the power marked. Runoff is of large importance concerning the availability of drinking water as well. And changes in the frequency of large floods may concern existing and planning of future infrastructure.

A hydrological scenario is obtained by the use of a rainfall-runoff model based on scenarios of temperature and precipitation. The rainfall-runoff model used is the HBV-model developed at the Swedish Meteorological Institute (SMHI) (Bergström 1976). A gridded version of the HBV model (GWB) is used as well. The HBV-model utilises daily station data of temperature and precipitation.

## **2. Meteorological and hydrological data**

Temperature and precipitation scenarios are obtained by dynamical downscaling. The HIRHAM model from Max-Planck Institute in Hamburg is used (Bjørge et al., 2000). It is based on the atmospheric-ocean circulation model ECHAM4/OPYC3 with the GSDIO integration, and the IS92a emission scenario. The model covers a limited area in Northern Europe and the time resolution is 6 hourly.

The temperature and precipitation grid values are interpolated to weather station sites. The values had to be adjusted to be representative for these stations locations. The dynamically downscaled values are utilised because of the HBV-models need for daily temperature and precipitation data.

The temperature, precipitation and runoff stations are selected to cover all regions of Norway (Figure 1). Even though many HBV-models had to be recalibrated to our purpose, advantage of existing HBV-models that are in daily use at the operational flood forecast office at NVE was obtained.

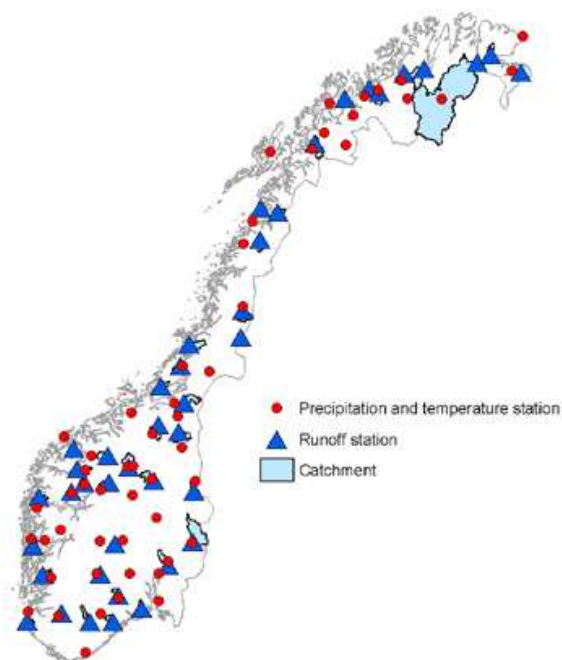


**Figure 1:** Weather and runoff stations used in the study.

The dynamically downscaled temperature and precipitation data represent a grid square covering an area of  $55 \times 55 \text{ km}^2$ . The cubic spline method was used to interpolate the modelled data to the station sites. Three time periods were used:

- Evaluation: HIRHAM run with input from ERA (ECMWF Re-Analysis), 1970 - 1993
- Control period: HIRHAM run with input from AOGCM from the time slice 1980-1999
- Scenario period: HIRHAM run with input from AOGCM for the time slice 2030-2049

During the evaluation period (1970-1993), the HIRHAM model was run with input from ERA. This means that resulting temperature precipitation values should be comparable with observations from the same period. Although there will be differences between downscaled and observed values, the modelled data should preferably come up with the same statistical moments as the observed data.

Interpolated temperature and precipitation data had to be adjusted to represent the station site. The ratio between the sums of observations and the ERA data set within the same period was used as an adjustment factor for precipitation. Such factors were established monthly at each

station. The adjustment factors are used on the interpolated daily data set for the control period, and for the scenario period. The adjustment was found to reconstruct the modelled mean modelled values for the control period quite satisfactory compared to the observations for the same period (see example in Fig. 2 (right)). The increase in precipitation in the scenario period compared to the control period is maintained.

For temperature data, a regression equation was established for each calendar month between the ERA data and the observed data for the same period [ $T_{obs} = a \cdot T_{ERA} + b$ ]. The adjustment reproduces the mean value for the control period satisfactory compared to the observations. An example of adjusted temperature data compared to the observations is presented in Figure 2 (left). The basic idea behind using regression was that the coefficient  $b$  should represent systematic difference (caused by e.g. difference in altitude) while  $a$  would reflect local temperature conditions (inversions etc.). The analysis, however, revealed difficulties concerning the adjustment of the temperature data with regression. When studying the difference between the scenario period and the control period, the temperature increase is changed with a factor corresponding to the regression coefficient  $a$ :  $(a \cdot \text{scenario} + b) - (a \cdot \text{control} + b) = a \cdot (\text{scenario} - \text{control})$ . This would have been a minor problem if the factor  $a$  had varied around 1 for the different stations and for different seasons. It was, however, found that  $a$  always is less than one, thus the temperature difference reported by Bjørge et al. (2000) is reduced. Evaluation of the adjusted dynamically downscaled precipitation and temperature series are documented in Skaugen et al. (2002).

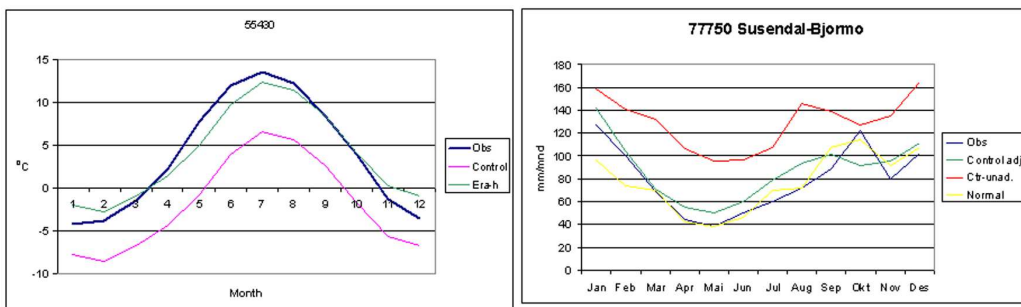


**Figure 2** Observed, modelled and adjusted temperature at station 55430 Bjørkehaug in Jostedal (left) and precipitation at station 77750 Susendal-Bjormo (right) for the control period (1980-99).

### 3. The HBV model

The HBV-modell has gained a widespread use for a large range of applications in Scandinavia and other countries, and a great number of versions have come to exist. The model can be classified as a semi-distributed conceptual model with sub-catchments as primary hydrological units. Each of these units is divided into area-altitude zones with a simple classification of land use (vegetation, lakes and glaciers). The sub-catchment option is used in geographically or climatologically heterogeneous catchments.

The model used in this project is a version of the HBV model developed for the project “Climate Change and Energy Production” (Sælthun et al., 1998). The general model structure can be divided into four modules: the snow module, the soil moisture zone module, the dynamic module and the routing model. The model has a simple structure and the requirements of input data are moderate (precipitation and temperature). Even for the different area-altitude zones, the parameters are generally the same for all sub-models. Interception, snowmelt parameters and soil moisture capacity can however be varied according to vegetation type. Simulations are run on a daily time step. For more information on model structure and algorithms the reader is referred to Sælthun (1996).

The HBV-model is also established in a spatially distributed version called the Gridded Water Balance (GWB) model (Beldring et al., 2002). The model performs water balance calculations for square grid-cell (1x1 km<sup>2</sup>) landscape elements, which are characterised by their altitude and land use. Each grid cell may be divided into two land-use zones with different vegetation, a lake area and a glacier area. The model is run with daily time steps, using precipitation and air temperature data as input. It has components for accumulation: sub-grid scale distribution and ablation of snow, interception storage, sub-grid scale distribution of soil moisture storage, evapotranspiration, groundwater storage and runoff response, lake runoff response and glacier mass balance. The model considers the effects of seasonally varying vegetation characteristics on potential evaporation. Daily precipitation and temperature values for the model grid cells are determined by inverse distance interpolation of observations from the three closest precipitation stations and the two closest temperature stations. Differences caused by elevation are corrected by site-specific precipitation altitude gradients and fixed temperature lapse rates for days with and without precipitation. The algorithms of the model are described in Sælthun (1996).

#### 4. Change in mean seasonal and annual runoff

Annual runoff for the normal period shows the same geographical pattern as for precipitation in Norway. Finnmark and inner parts of southern Norway are driest (runoff < 500mm/year) while western Norway and the coastal area in Nordland are wettest (runoff > 2000 mm/year). Figure 3 presents the projected change in the annual mean runoff in Norway in the scenario period (2030-2049) compared to the control period (1980-1999). This map is obtained by using modeled data with the GWB model. The mean annual runoff is projected to increase all over the country. The exception is the areas where the runoff is lowest. Wet areas of Norway will have even wetter conditions; the runoff will increase by between 100 and 1100 mm/year.

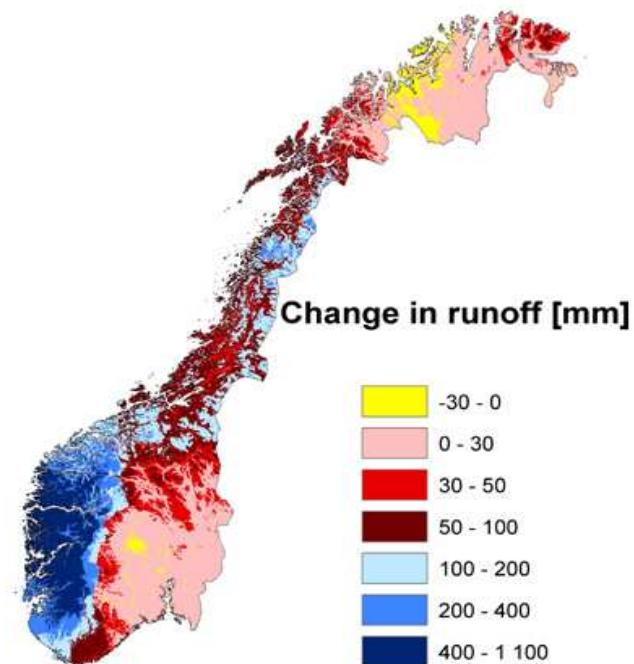


**Figure 3** Change in mean annual runoff in the scenario period (2030-2049) compared to the control period (1980-1999).

Results from the HBV-models calibrated with respect to catchments show similar change in annual runoff in the scenario period compared to the control period (Figure 4). The change is here presented as relative change. (The length of the yellow pile in the legend represents a change of 45%). Mean seasonal changes are presented as well. Autumn runoff will increase all over the country due to increased rainfall. Coastal areas will have largest increase in runoff during winter. Finnmark and inner parts of southern Norway will have the largest increase in runoff during spring. It also seems to be a decrease in runoff during summer. The major part of the snow melting usually occurs in summer in these areas. Higher temperatures may, however lead to earlier snowmelt (from summer to spring).

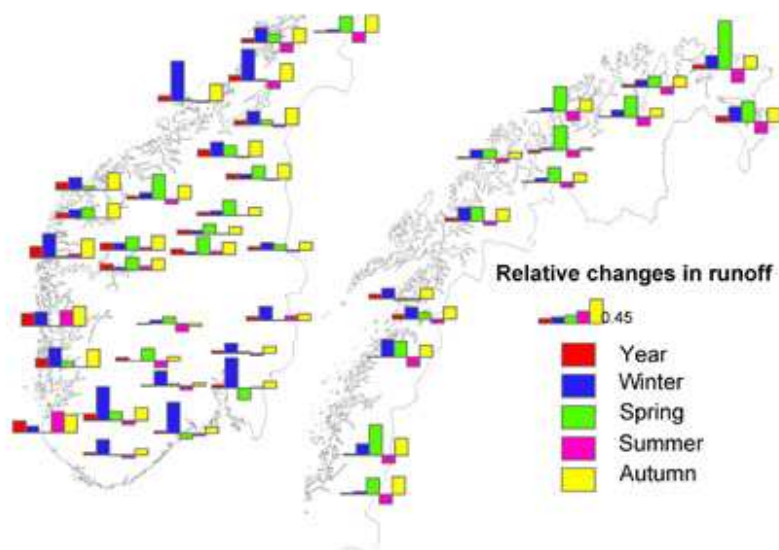


**Figure 4** Change in mean annual and seasonal runoff in the scenario period (2030-2049) compared to the control period (1980-1999).

## 5. Change in mean annual snow storage and evapotranspiration

An estimate of the change in snow storage in the spring (per 1st April) is obtained with GWB (Figure 5). High mountain areas in southern Norway and northernmost areas are projected to have an increase in snow storage; the rest of the country will have a reduction. The central areas in western Norway and mountain areas in Nordland will have the largest decrease (> 560 mm). Coastal areas have minor snow to day and will therefore have minor or no change in snow storage per the 1st of April.

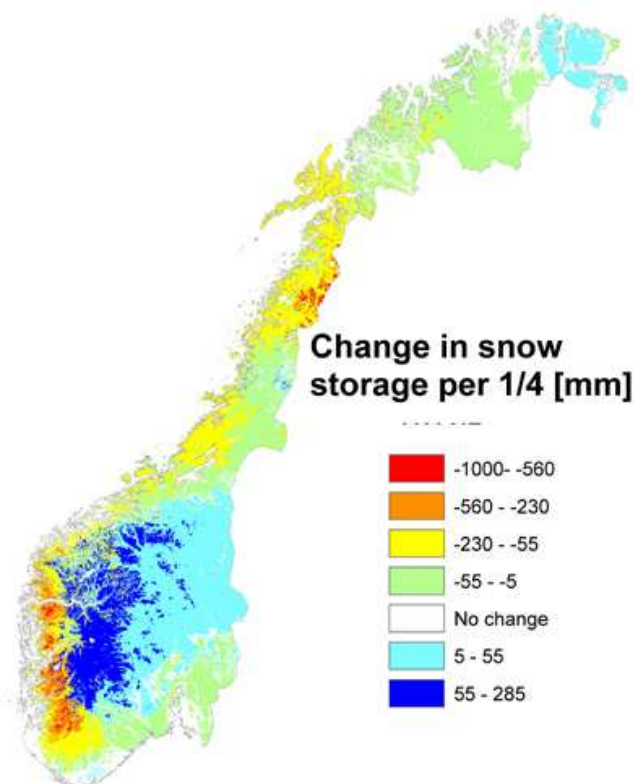


**Figure 5** Change in snow storage per 1<sup>st</sup> April in the scenario period (2030-2049) compared to the control period (1980-1999).

Evapotranspiration is projected to increase (30-100 mm/year) in the coastal area from Nordland to southern Norway and at the southernmost part of the country (Figure 6). The driest areas of Norway will have the lowest increase in evapotranspiration (0-30 mm/year).

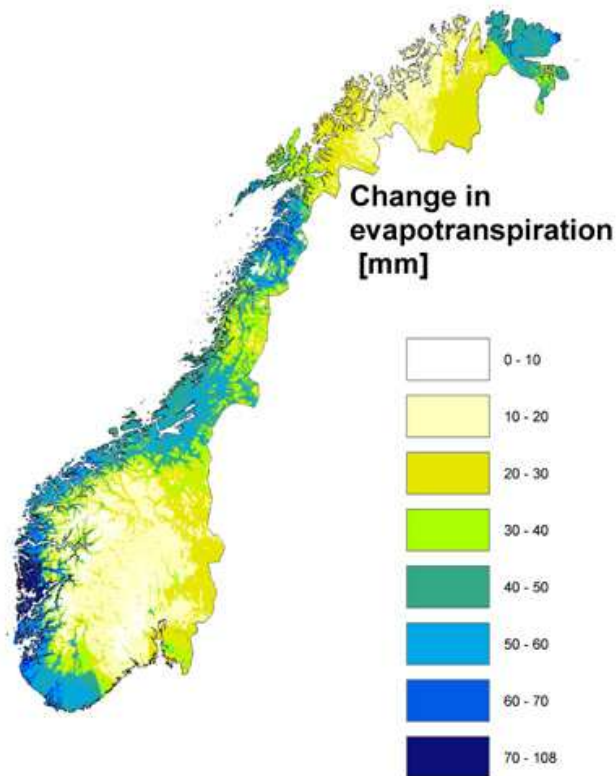


**Figure 6** Change in annual evapotranspiration in the scenario period (2030-2049) compared to the control period (1980-1999).

### Acknowledgement

The present study is performed in collaboration with the Norwegian Water Resources and Energy Directorate (NVE). This study is partly funded by the Norwegian Electricity Industry Association (EBL-Kompetanse AS) and the Research Council of Norway. The study is fully reported in Roald et al. (2003).

### References

Beldring S, LA Roald & A Voksø (2002) Avrenningskart for Norge. Årsmiddelverdier for avrenning 1961-1990, NVE-Dokument 2-2002, 49 pp.

- Bergström S (1976) Development and Application of a Conceptual Runoff Model for Scandinavian Basins. Report RH07, Swedish Meteorological and Hydrological Institute, Norrköping.
- Bjørge D, JE Haugen & TE Nordeng (2000) Future climate in Norway, DNMI Research report No. 103, 41 pp.
- Roald L, TE Skaugen, S Beldring, T Væringstad & EJ Førland (2003) Scenarios of annual and seasonal runoff for Norway based on meteorological scenarios for 2030-2049. Norwegian Water Resources and Energy Directorate, Oppdragsrapport A nr. 10-2002 / met.no Report 19/02 KLIMA, 56 pp.
- Skaugen TE, EJ Førland & I Hanssen-Bauer (2002) Adjustment of dynamically downscaled temperature and precipitation data in Norway, met.no Report 20/02 KLIMA 48 pp.
- Sælthun NR, P Aittonemi, S Bergström, K Einarsson, T Jóhannesson, G Lindström, PE Ohlsson, T Thomsen, B Vehviläinen & KO Aamodt (1998) Climate change impacts on runoff and hydropower in the Nordic countries. Final report from the project "Climate Change and Energy Production. TemaNord 1998:552. ISBN 92-893-0212-7. ISSN 0908-6692. Copenhagen.
- Sælthun NR (1996) The Nordic HBV model. Norwegian Water Resources and Energy Administration, Publication 7. 26 pp.

# **Adapting the Regional Ocean Model System for dynamic downscaling**

**by**

**Bjørn Ådlandsvik and W. Paul Budgell**

Institute of Marine Research, Bergen

## **1. Introduction**

Knowledge on the future marine climate on the continental shelf areas outside Norway is important due to the economically important petroleum and fisheries activities. The shelf sea climate is to a large degree determined by the volume and the properties of the Atlantic Water entering the shelves. This inflow is governed by the larger scale inflow of Atlantic Water to the Nordic Seas, local topographic details, and regional atmospheric conditions affecting the branching of the Atlantic Current.

To study these problems a shelf sea model will be used for dynamic downscaling of future climate scenarios from global coupled ocean-atmosphere models to Norwegian shelf seas. The model chosen for the downscaling is the Regional Ocean Model System (ROMS) developed by Hernan Arango at Rutgers University and Alexander Shchepetkin at UCLA. This report describes some of the work done at the Institute of Marine Research on open boundary conditions and sea ice to adapt the model system for the purpose.

## **2. The Regional Ocean Model System**

The ROMS model is based on the primitive Boussinesq equations. The model uses a terrain-following coordinate system in the vertical direction called "s-coordinate" (Song and Haidvogel, 1994). It can be characterised as a generalised sigma-coordinate, allowing improved resolution near surface and bottom in the deeper parts of the domain. In the

horizontal, general orthogonal curvilinear coordinates are used. The model uses finite differences with a time splitting between the fast 2D barotropic mode and the slower baroclinic 3D mode.

The numerical methods are explained in a series of papers by Shchepetkin and McWilliams (1998, 2003a, 2003b) and Ezer et al. (2002). The ROMS model uses relative high order schemes including a vertical parabolic spline representation. ROMS has been designed for effective parallelisation. The upcoming version 2.0 offers serial, shared memory (OpenMP) and distributed memory (MPI) parallelisation from the same Fortran 95 code. Work is on the way to provide the tangent linear and adjoint models of ROMS (Moore et al., 2003).

### **3. Open Boundary Conditions**

For the purpose of downscaling from global models, the choice of open boundary condition (OBC) is important. The ROMS model system offers a variety of OBCs including clamped, Flather, Chapman, and an adaptive radiation condition. These are described by Marchesiello et al. (2001).

The Flow Relaxation Scheme (FRS) is an OBC that has been used for atmospheric models for years. For ocean modelling, an implementation in a barotropic ocean model is described by Martinsen and Engedahl (1987). Later an implementation in the 3D baroclinic Princeton Ocean Model was done by Engedahl (1995). Experience has proven the FRS to be a robust and well-behaved OBC, permitting outside information to enter the domain without too much reflections of waves generated within the domain. It is therefore natural to consider the FRS boundary condition for marine downscaling. The FRS condition is not among the OBCs provided by the ROMS developers. An implementation of FRS in ROMS 2.0 has therefore been done at IMR. This implementation works with both parallelisation schemes. The theory behind the implementation is mainly lifted from the Bergen Ocean Model (BOM) (Heggelund and Berntsen, 2000; Berntsen, 2002). The details will be reported elsewhere.

The ROMS model code conserves salt and heat. By the continuity equation this is equivalent to conserving salinity and temperature. However, FRS or any other kind of relaxation of the surface elevation breaks the continuity equation. This problem becomes more pronounced in

shallow areas, such as the North Sea. Using FRS for the free surface gave unrealistic high values of salinity in the English Channel. This may be corrected by incorporating the proper source term in the tracer equations.

Abandoning the FRS, the 2D variables including tide is treated by a combination of the Flather condition for the normal component of the depth averaged current and a Chapman condition for the tangential component and the surface elevation. This combination is used with success for nesting a regional model in the Gulf Stream area (H. Arango, pers. comm.). The FRS is retained for 3D current and the salinity and temperature fields.

#### **4. Ice component**

In order to conduct dynamical downscaling exercises for the Barents Sea region, it is essential to include effects of dynamic and thermodynamic ice-ocean interaction processes. This has been accomplished through coupling a dynamic-thermodynamic ice model to version 2.0 of the ROMS. The ice dynamics are based upon the elastic-viscous-plastic (EVP) rheology of Hunke and Dukowicz (1997) and Hunke (2001). Viscous-plastic rheology (Hibler, 1979) has a long history of successful applications in sea-ice climate studies. However, the large viscosities required to represent regions of nearly rigid ice has necessitated the use of implicit, iterative solvers, which prove to be an impediment to efficient parallel computation. The EVP scheme accomplishes the regularization required at low deformation rates through the use of short, explicit, elastic time steps. The EVP scheme that has been coupled to ROMS is found to parallelize very efficiently in both shared memory (OpenMP) and distributed memory (MPI) modes of operation. Both ROMS and the ice model employ orthogonal curvilinear coordinates in the horizontal. For this reason, the ice model is currently being updated to include a correct representation of the internal ice stress terms on a curvilinear grid based on Hunke and Dukowicz (2002).

The ice thermodynamics are based upon Mellor and Kantha (1989) and include two internal ice layers and a snow layer. Internal ice temperature is an advected quantity.

The coupled ice-ocean ROMS has been applied to an area extending from the south of the equator in the Atlantic, north through the Nordic Sea and the Arctic Ocean (Fig. 1). The region is selected both as a test bed for basin-scale calculations and to provide open boundary conditions to the North Sea and Barents Sea regional models used in the dynamical downscaling study. Simulated ice thickness, and ice concentration and velocities from March 28, 1948, are shown in Fig. 2. Every ninth velocity vector is shown. The forcing for the simulation consists of daily mean NCEP surface fluxes corrected for model surface temperatures and ice conditions.

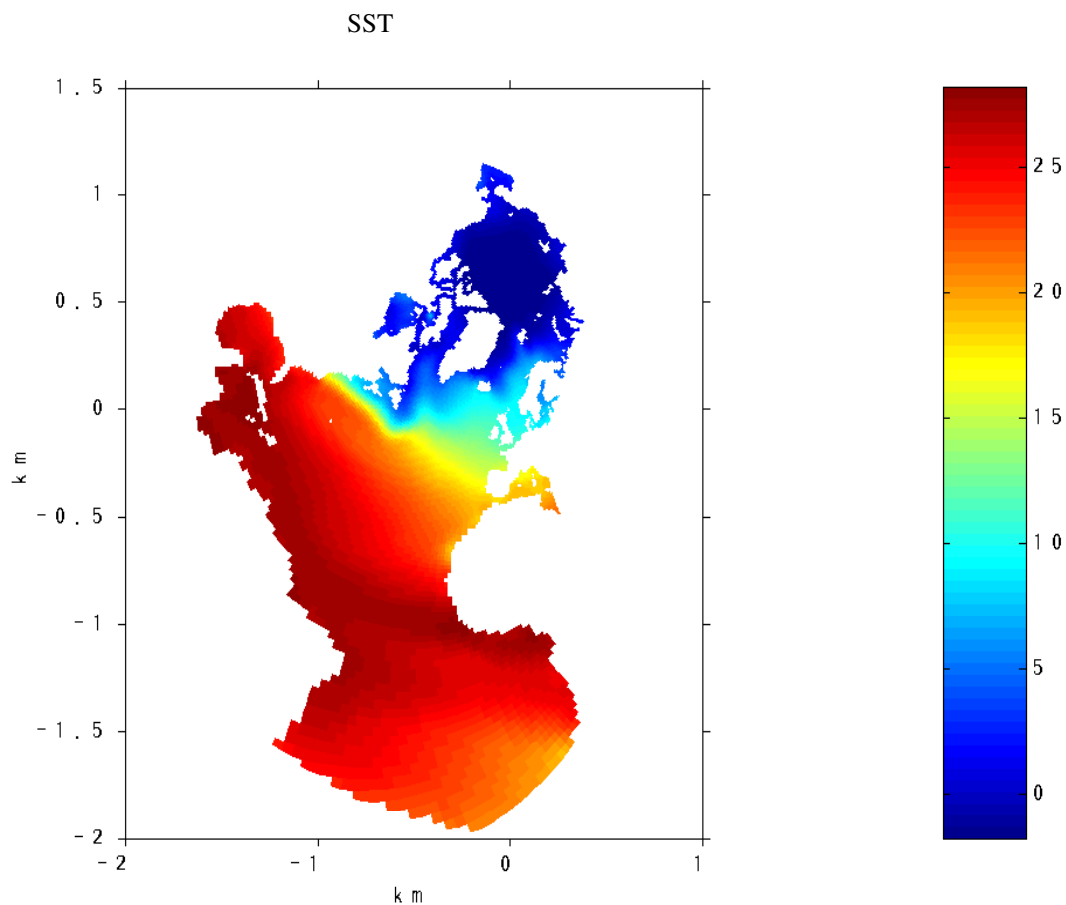


**Figure 1.** The Atlantic scale model domain with sea surface temperature.

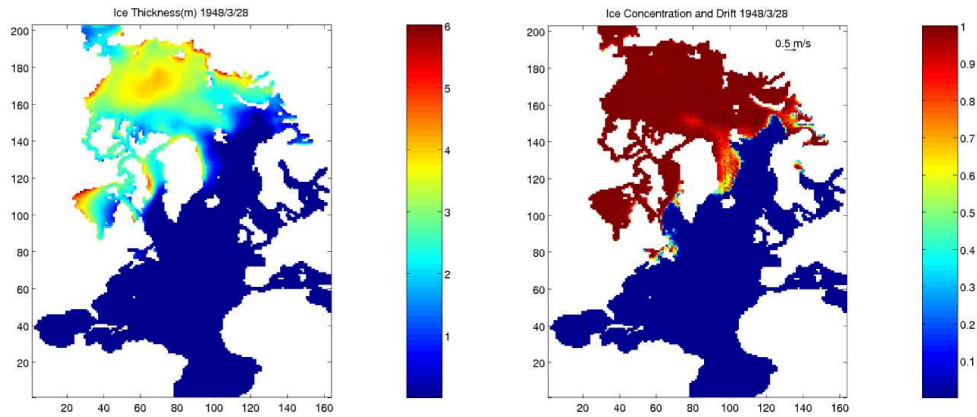


**Figure 2.** Modelled sea ice thickness (left) and ice concentration (right). The right panel also displays the sea ice velocity

## 5. North Sea model set up

The present North Sea model domain as shown in figure 3 has 200 by 175 grid cells with 8 km resolution. In the vertical 32 s-levels is used. The atmospheric forcing of the model is taken from the NCEP reanalysis, and consist presently of wind stress only. Freshwater input is taken from climatological runoff values from 16 major rivers plus the Baltic Sea. The initial conditions and lateral forcing come from the joint diagnostic climatology of met.no and IMR (Engedahl et al., 1998). In addition, four tidal constituents are prescribed at the lateral boundaries.

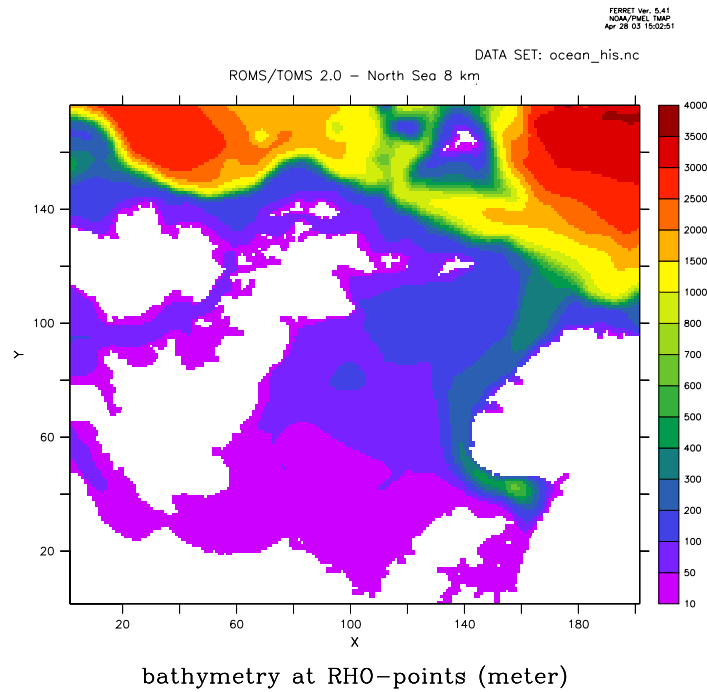


**Figure 3.** The North Sea model domain with bottom topography

## 6. Preliminary results from the North Sea model

Figure 4 shows the sea surface salinity and temperature after 44 days. Both panels show the warm and saline Atlantic Current at the shelf edge with branches into the North Sea. The main inflow is in the western part of the Norwegian Trench and extends into Skagerrak, feeding a cyclonic circulation in this area. There is also a branch of Atlantic Water entering the North Sea between Orkneys and Shetland. These pictures agree qualitatively with the observational picture of the water masses and the circulation in the North Sea.

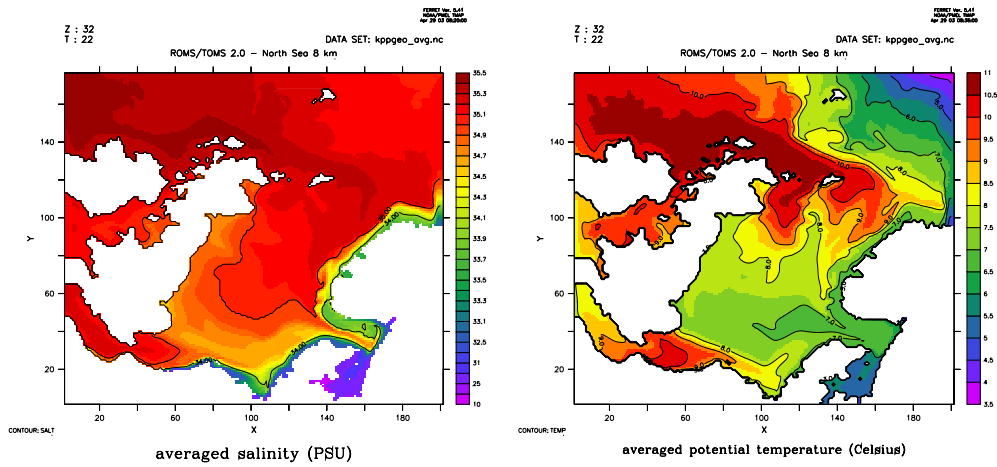


Figure 4. Modelled sea surface salinity and temperature averaged from day 43 to day 45

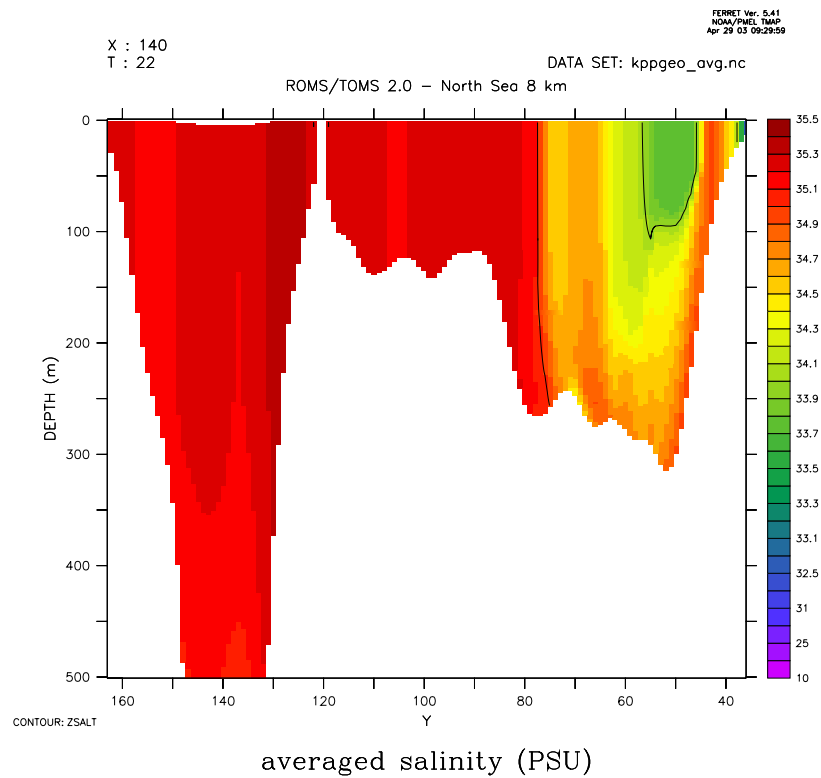


Figure 5. Model salinity section, from the Faeroes (left) to Egersund (right).

However, the Norwegian Coastal Current looks quite narrow. To examine this closer, a vertical salinity section from the Faeroes to Egersund through Shetland is shown in figure 5. The fresh coastal water extends too deep, and the front towards the Atlantic Water is too steep. The reason is probably too strong vertical mixing due to lack of bouyancy forcing. During winter conditions this must be caused by lack of fresh water forcing.

Overall, the model including the OBC seems to be working for the North Sea. However, more work has to be done regarding the forcing. Run off from areas without major rivers, and precipitation on sea will be added.

## 7. Future plans

A similar regional setup of ROMS for the Barents Sea is planned. This will include the sea ice module. This module is now working on larger scale, but some adaptations may be needed for the regional scale. In particular, it is not resolved how to treat the lateral open boundary for sea ice.

In both regions the model setup will be validated and the added value of downscaling assessed for present climate. For the North Sea the Skagex experiment in spring 1990 provides a good dataset for this purpose. In the Barents Sea, the model will be validated against hydrographical data and current measurements from IMR.

## References

- Berntsen, J. 2002. USERS GUIDE for a modesplit sigma-coordinate numerical ocean model, version 3.0, available as <http://www.mi.uib.no/BOM/BOMguide30.ps.gz>
- Engedahl, H., 1995. Use of the flow relaxation scheme in a three-dimensional baroclinic ocean model with realistic topography. *Tellus* 47A, 365-382.
- Engedahl, H., B. Ådlandsvik, and E.A. Martinsen, 1998. Production of monthly mean climatological archives of salinity, temperature, current and sea level for the Nordic Seas, *J. Mar. Syst.*, 14, 1-26.
- Ezer, T., H.G. Arango and A.F. Shchepetkin, 2002. Developments in terrain-following ocean models: intercomparisons of numerical aspects, *Ocean Modelling*, 4, 249-267.
- Heggelund, Y. and J. Berntsen, 2000., A two-way nesting procedure for an ocean model with application to the Norwegian Sea, in Y. Heggelund 2000. Numerical ocean modelling. On local grid refinement and nonhydrostatic physics, Dr.Scient. Thesis, Department of Mathematics, University of Bergen.

- Hibler, W.D. (1979). A dynamic thermodynamic sea ice model. *J. Phys. Oceanogr.*, 9: 817-846.
- Hunke, E.C. (2001). Viscous-plastic sea ice dynamics with the EVP model: Linearization issues. *J. Comput. Phys.*, 170:18-38.
- Hunke, E.C. and J.K Dukowicz (1997). An elastic-viscous-plastic model for sea ice dynamics. *J. Phys. Oceanogr.*, 27:1849-1867.
- Hunke, E.C. and J.K Dukowicz (2002). The elastic-viscous-plastic sea ice dynamics model in general orthogonal curvilinear coordinates on a sphere – Incorporation of metric terms. *Mon. Wea. Rev.*, 130:1848-1865.
- Marchesiello, P., J.C. McWilliams, and A.F. Shchepetkin, 2001. Open boundary conditions for long-term integration of regional ocean models, *Ocean Modelling* , 3,1-20.
- Martinsen, E.A. and H. Engedahl, 1987, Implementation and testing of a lateral boundary scheme as an open boundary condition in a barotropic ocean model, *Coastal Engineering*, 11, 603-627.
- Mellor, G.L. and L. Kantha (1989). An ice-ocean coupled model. *J. Geophys. Res.*, 94:10937-10954.
- Moore, A.M., H.G. Arango, A.J. Miller, B.D. Cornuelle, E. Di Lorenzo and D.J. Neilson, 2003. A Comprehensive Ocean Prediction and Analysis System Based on the Tangent Linear and Adjoint Components of a Regional Ocean Model, Draft, available on internet as [http://marine.rutgers.edu/po/Papers/lat\\_roms\\_om.pdf](http://marine.rutgers.edu/po/Papers/lat_roms_om.pdf)
- Shchepetkin, A.F. and J.C. McWilliams, 1998. Quasi-monotone advection schemes based on explicit locally adaptive dissipation, *Monthly Weather Rev.*, 126, 1541-1580
- Shchepetkin, A.F. and J.C. McWilliams, 2003a. A Method for Computing Horizontal Pressure-Gradient Force in an Oceanic Model with a Non-Aligned Vertical Coordinate, *J. Geophys. Res.*, 108, 1-34
- Shchepetkin, A.F. and J.C. McWilliams, 2003b. The Regional Ocean Modeling System: A split-explicit, free-surface, topography-following coordinates ocean model, Draft, available as <http://marine.rutgers.edu/po/Papers/roms.pdf>
- Song, Y.T. and D.B. Haidvogel, 1994. A semi-implicit ocean circulation model using a generalized topography-following coordinate system, *J. Comput. Phys.*, 115, 228-244



**Improvements in the sea ice module of the regional coupled  
atmosphere-ice-ocean model and the strategy and method for the  
coupling of the three spheres.**

**by**

**Jens Debernard, Morten Ødegaard Køltzow, Jan Erik Haugen and Lars  
Petter Røed**

Norwegian Meteorological Institute, P.O.Box 43 Blindern, 0313 Oslo, Norway

## **Introduction**

The development of a regional coupled atmosphere-ice-ocean model within RegClim is now in its final stages. In this advance the two dominant guiding principles are 1) heat should be conserved, and 2) the heat fluxes responsible for the exchange of heat between the three spheres should be computed only once. Experiments with earlier versions of the Norwegian Meteorological Institute's ice model (MI-IM), one of the components in the coupled system, has shown that in addition to being too stiff (which prompted the implementation of the elastic-plastic-viscous (EVP) rheology to replace the common viscous-plastic rheology, e.g., Sætra et al. 1998, 1999), the ice model also tended to lose too much heat (e.g., Shi et al. 2000). This was later found to be caused by the fact that the model simply did not conserve heat. Thus the first of the above principles encouraged the introduction of a new ice variable, namely the energy needed to melt all the sea ice, for which an additional advection equation is constructed. A description of this improved version of MI-IM is the main theme below.

In addition also the strategy and methods whereby the regional coupling of the three spheres atmosphere, ice, and ocean is to be achieved within the RegClim project is described. In this one of the main problems is the values to be used as input on the open lateral boundaries in the regional ice-ocean model. Here this is accomplished by nesting the regional ice-ocean model into a coarse mesh basin wide Atlantic ice-ocean model.

## **MI-IM improvements**

One important feature of the atmosphere-ocean interface at high latitudes is sea ice. Besides the fact that the sea ice changes the surface albedo, isolates the atmosphere from the ocean, and alters the atmosphere-ocean momentum exchange, it also acts as a heat reservoir. In fact, in places where the atmosphere is cold the heat flux from the ocean surface to the atmosphere is larger than the heat flux from the interior ocean to the surface. This heat deficit is stored as sea ice. Subsequently the ice is advected to another location where it melts. Thus to obtain a conservative heat exchange at the atmosphere-ocean interface it is of utmost importance that the internal thermodynamics of the sea ice model also conserves heat. This was a problem in the earlier versions of met.no's ice model MI-IM (Sætra et al. 1998, 1999). In the new version of MI-IM this problem is solved by introducing a new prognostic variable which simply measures the energy required to melt all ice.

Sea ice differs from freshwater ice by the fact that each time ice is formed a small amount of salt becomes trapped in the ice in the form of pockets which contains a salt solution,

referred to as brine pockets. The small, but most striking consequence is a lowering of the melting temperature of the ice compared to freshwater ice. Given that the salinity of sea ice,  $S_{ice}$ , is between 1 and 8 psu, the melting temperature (in degrees Celsius) is approximated by  $T_{mi} = -\mu S_{ice}$ , where  $\mu = 0.054$  °C. The most important difference however appears for ice colder than the melting point. Since the sea ice consists of both pure ice (similar to freshwater ice) and brine pockets, the specific heat capacity of sea ice becomes

$$c = c_0 - L_0 \frac{T_{mi}}{T^2}, \quad (1)$$

where  $c_0$  is the specific heat capacity and  $L_0$  the latent heat of freshwater ice. Note that the ice temperature,  $T$ , is measured in degrees Celsius. The physics underlying (1) is that any change in the ice temperature gives rise to a transition between the amount of brine volume and the amount of freshwater ice. As a consequence the heat capacity increases considerably as the ice temperature approaches the melting point ( $T_{mi}/T^2 \leq 0$ ).

The energy required to increase the temperature of sea ice from a given initial temperature  $T$  to the melting temperature  $T_{mi}$  is

$$q(T, S_{ice}) = \int_T^{T_{mi}} c dT' = c_0(T_{mi} - T) + L_0 \left(1 + \frac{T_{mi}}{T}\right). \quad (2)$$

Eq. (2) is illustrated in Figure 1. For freshwater ice (dashed line), the energy required to rise the temperature up to the melting temperature is small. However, when the temperature reaches the melting point, a large amount of energy is required simply because the energy needed to change freshwater ice to water is much larger than the energy needed to change its temperature. For sea ice, the picture is somewhat different (solid line) since the heat capacity, as given by (1) is always larger than that of freshwater ice ( $T_{mi}/T^2 \leq 0$ ). Thus when the sea ice temperature increases a large amount of energy actually goes into melting the ice surrounding the brine pockets, that is, to increase the brine volume. As the temperature gets closer to the melting temperature a considerable amount of sea ice is already melted because of this. Therefore, as illustrated in Figure 1, the energy required to melt sea ice close to its melting point is always less than the comparable energy required to melt warm freshwater ice.

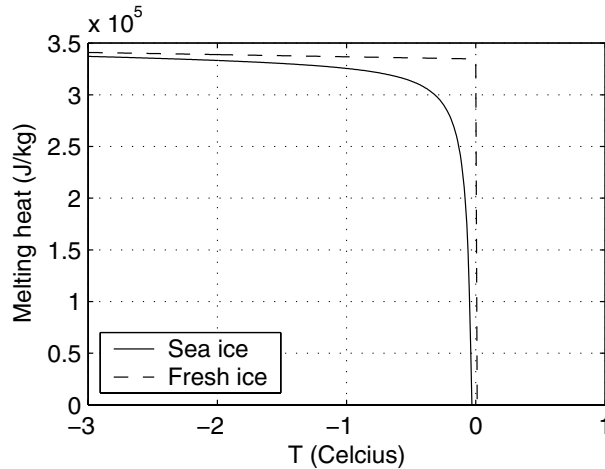


**Figure 1:** Solid line shows the amount of energy required to melt sea ice of salinity 6 psu, while the dashed line shows the energy needed to melt freshwater ice from a given initial temperature. The horizontal axis shows the latter temperature in degrees Celsius, while the vertical axis shows the energy needed in J/kg.

This particular property of sea ice has some important consequences for the design of sea ice models. One of the simplest representations is to treat the ice as pure freshwater ice while neglecting its heat capacity. Then heat storage is in the form of latent heat only, which as revealed by Figure (1) contains most of the effect of the ice as a heat reservoir. It is possible to construct a heat-conserving sea ice model with this approach. However, according to Bitz and Lipscomb (1999), this results in an overestimation of the seasonal variations in ice-thickness. In addition the ice tends to melt too early in spring/summer and to freeze too early in the fall.

If more realistic ice thermodynamics is included, with a salinity dependent heat capacity in accord with (1), then to conserve heat content the internal energy of the ice must be advected in the same manner as the other ice variables. The neglect of this fact was the problem in the earlier versions of MI-IM, in which the thermodynamics were based on the formulations of Mellor and Kantha (1989) and Häkkinen and Mellor (1992). Although a realistic heat capacity was used, an advection of the internal energy in the ice was neglected. In a regional coupled atmosphere-ice-ocean models in which a solid portion of the sea ice formed in the Arctic is actually melted in the East Greenland Current the consequence is that the model tended to loose heat.

To solve this problem, a new thermodynamic variable  $E$ , named the energy required to melt all the ice, is introduced. It is formulated as

$$E = \rho_{ice} h_{ice} A q(T, S_{ice}), \quad (3)$$

where  $A$  is the ice concentration,  $\rho_{ice}$  is the ice density, and  $h_{ice}$  is the mean ice thickness. A conservation law for  $E$  is formulated as

$$\frac{\partial E}{\partial t} + \nabla \cdot (\mathbf{V}_{ice} E) = A(Q_{ai} - Q_{oi}) + (1 - A)(Q_{ao} - Q_{oa}), \quad (4)$$

where  $\mathbf{V}_{ice}$  is the ice drift velocity and the  $Q$ 's denotes the various heat fluxes as displayed in Figure 2. Note that last term on the right-hand side of (4) is a term for the open ocean portion of a unit cell. Under normal circumstances this term vanishes due to a balance between the two fluxes  $Q_{ao}$  and  $Q_{oa}$ . If, however, the sea surface temperature (SST) drops below the freezing point of sea water, an imbalance in these fluxes exists and new ice will grow. This in turn contributes to a change in the heat required to melt all the sea ice, that is,  $E$ .

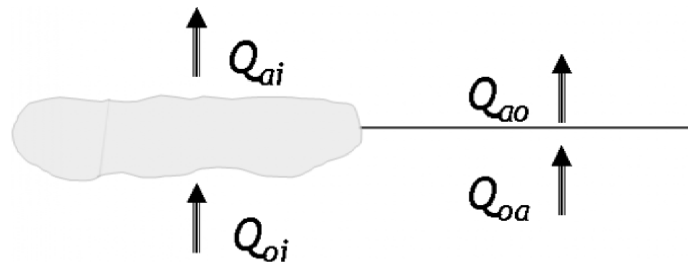


**Figure 2:** Definition of heat fluxes between atmosphere, ice and ocean. The subscript indicates which mediums are involved and such that the first letter indicates which side of the interface the heat flux is calculated. Thus  $Q_{ao}$  is the heat flux from the ocean surface toward the atmosphere and is calculated just above the sea surface, whereas  $Q_{oa}$  is the heat flux from the ocean toward the atmosphere-ocean interface and is calculated just below the surface.

The introduction of  $E$  as the new prognostic variable provides the means by which the internal thermal energy in the sea ice is conserved. For instance, examine the horizontal integral of (4) over a finite domain assuming no advection through the lateral boundaries takes place. Then the total change in  $E$  is exactly matched by any imbalance in the heat fluxes between the atmosphere and the ocean. This conservation property gives the basis for a true heat conservative atmosphere-ocean coupling interface.

### Coupling strategy and method

To establish a coupling strategy for the regional coupled atmosphere-ice-ocean climate model (AORCM) the most stringent principle is that the fluxes exchanging energy between the three spheres are calculated only once. At present the AORCM under development

consists of the atmosphere model HirHam, the sea ice model MI-IM and the ocean model MICOM. By studying the documentation of several different coupled climate models, it is decided to base the development on the suggestions given in the two global models NCAR CCSM2.0 (Kauffman and Large, 2002) and BCM (Furevik et al. 2002), and the regional model RCAO (Döscher et al. 2002).

Based on these studies we have identified the following points that define our strategy for the coupling:

- Fluxes are computed only once.
- Flux conservation is a must
- Fluxes delivered as average values over the coupling time step
- Fluxes are to be delivered weighted on the atmospheric grid (no weighting over land-sea cells)
- Fluxes and parameters delivered in SI units
- The ocean mesh is a multiple of the atmospheric mesh

The last item may be viewed as a convenient principle, but actually it makes the task of conserving fluxes much easier. In principle the three meshes could be arbitrary, but this makes it almost impossible to exactly conserve fluxes. The first 3 points, however, are necessary to ensure a heat conservative coupling interface. Based on the experience from other coupled models, it seems obvious that the natural boundary condition to use on interfaces between coupled models is fluxes of heat, momentum and mass (freshwater). To ensure consistency between the fluxes used by the different models, these fluxes should be calculated only once, and then be distributed to the remaining models. The simplest way to ensure global heat and mass conservation is simply to exchange the average or the accumulated value over the complete coupling time step of the flux in question.

Concerning where the fluxes should be calculated, there are several options available. Generally, the horizontal grid in the atmosphere model is coarser than the ice-ocean mesh. Where the fluxes are to be calculated should preferably be based on physical arguments. Concerning stresses (momentum flux) and the surface heat fluxes (turbulent and upward directed long wave radiation), this is normally done in the model that has the most detailed information about the surface state, which in the present context implies MI-IM. However, due to the internal numerical method and coding of the atmosphere model HirHam, it is difficult to apply these fluxes directly as a boundary condition at the surface without a major recoding of the model. Different approaches are chosen in this respect in the climate models above. In the NCAR CCSM, all surface fluxes are calculated in the ice model or in the

coupler at the grid with highest horizontal resolution. The integral of these fluxes over each atmospheric grid cell is then passed to the atmosphere model. On the other hand, in the BCM, all these fluxes are calculated in the atmosphere model on the coarse grid. They are then passed to the coupler and a sub-grid interpolation method is used to distribute the fluxes in the physically most appropriate manner to the ice/ocean grid. The reason for this difference is probably the difficult task of recoding the ARPEGE atmosphere model used in the BCM. The latter option (as in the BCM) is opted here and probably then for the same reason.

Concerning the heat fluxes an implicit numerical method is utilized for the boundary layer physics in HirHam. This routine uses the surface temperature  $T_s$  as a lower boundary condition for several different surface types (land, ice, and sea). Therefore, it may be cumbersome to rewrite these schemes in such a way that they directly make use of a heat flux as the lower boundary condition. Consequently, our approach is again to calculate the turbulent heat fluxes in the atmosphere model, transfer them MI-IM, and then perform a sub-grid interpolation. Other downward heat fluxes like shortwave radiation and downward long wave radiation is naturally calculated in the atmosphere model due to their physical nature, since they depend on integral properties of the atmosphere. At least for the net short-wave radiation a sub-grid interpolation method should be used.

The transfers of fluxes between the coarse atmosphere grid and the higher resolved ocean grid is generally of two types, integration from ocean to atmosphere grid and sub-grid interpolation from the coarse to the fine grid. Let the respective contribution to the turbulent fluxes from an open sea be denoted  $Q^o$  and that from sea ice  $Q^i$ , then the total heat flux to the atmosphere over an atmospheric grid cell with area  $\Omega$  is defined by the integral

$$\bar{Q}^a = \frac{1}{\Omega} \iint_{\Omega} [A Q^i(x, y) + (1 - A) Q^o(x, y)] dx dy. \quad (5)$$

When the fluxes  $Q^o$  and  $Q^i$  are known, this is well-defined. More challenging is the problem to find  $Q^o$  and  $Q^i$  for a given  $\bar{Q}^a$ . For surface heat fluxes, which are strongly dependent of the surface temperature, this is usually done by approximating the fluxes with a Taylor expansion in the surface temperature, that is,

$$Q^o = \bar{Q}^a + \frac{\partial \bar{Q}^a}{\partial T_s} (T_{SST} - T_s^{ref}), \quad (6)$$

and

$$Q^i = \bar{Q}^a + \frac{\partial \bar{Q}^a}{\partial T_s} (T_{IST} - T_s^{ref}) \quad (7)$$

Here,  $T_{SST}$  and  $T_{IST}$  is the sea surface and ice surface temperatures, respectively, and  $T_s$  denotes the surface temperature used to calculate  $\bar{Q}^a$ . By inserting these expressions into (5) the requirement of heat conservation gives naturally the reference temperature as the area-averaged temperature, that is,

$$T_s^{ref} = \frac{1}{\Omega} \iint_{\Omega} [AT_{IST} + (1-A)T_{SST}] dx dy. \quad (8)$$

For the net short-wave radiation an albedo-weighted sub-grid interpolation is used instead of the Taylor expansion method for surface fluxes, that is,

$$Q_{sw}^o = \frac{1-\alpha^o}{1-\alpha^{ref}} \bar{Q}_{sw}^a \quad \text{and} \quad Q_{sw}^i = \frac{1-\alpha^i}{1-\alpha^{ref}} \bar{Q}_{sw}^a,$$

where the constraint of heat conservation defines the reference albedo as

$$\alpha^{ref} = \frac{1}{\Omega} \iint_{\Omega} [A\alpha^i + (1-A)\alpha^o] dx dy.$$

The fluxes and state variables transferred between the atmosphere model and MI-IM are shown in Table 1.

**Table 1:** Fluxes and state variables exchanged in the AORCM

Flux/parameter	Computed where	Unit	Comment
Long wave radiation (up)	Coupler (MI-IM)	W/m <sup>2</sup>	
Long wave radiation (down)	Atmosphere (HIRHAM)	W/m <sup>2</sup>	
Net short wave radiation	Atmosphere	W/m <sup>2</sup>	
Turbulent heat fluxes	Atmosphere	W/m <sup>2</sup>	
Moment. (stress)	Atmosphere	Pa	
Precipitation (snow, rain)	Atmosphere	m/s	
Evaporation	Atmosphere	m/s	
Runoff	Atmosphere	m/s	
Sea ice concentration ( $A$ )	Coupler (MI-IM)		
Sea ice surface temperature ( $T_{IST}$ )	Coupler (MI-IM)		
Sea surface temperature ( $T_{SST}$ )	Coupler (MI-IM)		
Albedo ( $\alpha$ )	Coupler (MI-IM)		
Cloud fraction (CLF)	Atmosphere		Used in albedo calculation
DQ/dT <sub>s</sub> (turb. fluxes)	Atmosphere		

## **Spin-up strategy for the AORCM**

As mentioned in the introduction a challenge for AORCM simulations is the specification of proper lateral boundary values and initial conditions for the ice-ocean component of the coupled system. Normally, simulations with regional climate models are time-slice experiments where the regional model is compute for a time-period of say approximately 30 years. For the atmospheric part of the model, boundary conditions and initial conditions is simply taken directly from a global climate model due to the short spin-up time of the model. However, for the ocean model, the spin-up time may be hundreds of years. Therefore, it is of importance that the initial condition and boundary data used for the ice-ocean is close to the climate in the global climate model, but at the same time consistent with the interior physics of the ocean component of the chosen AORCM. Because MICOM is an isopycnic coordinate ocean model its vertical grid is very different from the geopotential vertical coordinate grid used in most global climate models. Hence a very wide conversion zone from z-level to density coordinates is required.

Our strategy is to set up a relatively intermediate resolution, basin wide ocean domain, covering the Atlantic Ocean down to about 30 degrees south including the whole Arctic Ocean. On the boundary of this domain, data in geopotential coordinates is used as boundary conditions on temperature, salinity, velocity and surface elevation. In parts of the domain, the density structure of MICOM may be nudged towards the state of global model to force the intermediate model to give a climate very similar to that in the global model. Surface forcing for the model should be taken from the global atmosphere model. This intermediate model should run for the whole or most of the scenario period for the global model, giving an MICOM compatible, and intermediate downscale of the ocean state in the northern part of the Atlantic and the Arctic. It is important that the model have a Meridional Overturning Circulation (MOC) similar to that found in the global ocean model.

An AORCM time-slice experiment with ocean initial and boundary data taken from the intermediate MICOM simulation could then be done.

## **Summary and final remarks**

Above is considered the important items concerning the coupling of the three spheres atmosphere, cryosphere and hydrosphere. The considerations stems from the ongoing development of a coupled atmosphere-ocean regional climate model (AORCM) undertaken as part of the national climate project RegClim. An important aspect in this is to conserve heat

whenever heat is exchanged between the model modules in the system. This has led to an improvement of the ice component in the coupled system along the lines suggested, e.g., in the ice model of the NCAR CCSM2.0 global climate model (Bitz and Lipscomb, 1999). This involves the introduction of the thermal energy required to melt all the sea ice as a new ice prognostic variable for which a conservation equation is implemented in MI-IM (Norwegian Meteorological Institute's ice model).

Other aspects concern the strategy and method whereby the various fluxes (momentum, turbulent heat fluxes, etc.) should be calculated. In the present work the two most important guidelines where the conservation of heat and that the heat fluxes responsible for the exchange of heat between the three spheres should be computed only once. To avoid a major recoding of the atmosphere model HirHam it was decided to compute most of the fluxes in the atmosphere model as for instance done in the accompanying global model RegClim model or the BCM (Furevik et al. 2000).

A final consideration is the lateral boundary conditions and initial condition to be used in the ice-ocean model of the AORCM. In the present development this is achieved by running a coarse mesh version of the ice-ocean model component covering the Arctic Ocean and the Atlantic ocean down to about 30 degrees south into which is nested the finer mesh regional model. The coarse mesh model is then driven by the global scenario atmospheric forcing using the global ocean component as its lateral boundary condition at the southern open boundary.

### **Acknowledgement:**

All authors are in whole (JD) or in part (MØK, JEH, LPR) supported by the Research Council of Norway under the national project RegClim (grant no. 155976/720), and the EU project GLIMPSE (EVK2-2001-00337) (MØK, JEH, LPR).

### **References:**

- Bitz, C.M. & W. H. Lipscomb (1999): An energy-conserving thermodynamic model of sea ice. *J Geophys Res.*, 104(C7), 15,669-15,677.
- Döscher R., Willén U., Jones C., Rutgersson A., Meier H.E.M. and U Hansson (2002): The development of the coupled ocean-atmosphere model RCAO. Rossby Centre, SMHI, S-60176 Norrköping, Sweden.

- Furevik T, Bentsen M, Drange H, Kindem L.K.T., Kvamstø N.G. and A. Sorteberg (2002): Description and Evaluation of the Bergen Climate model: ARPEGE coupled with MICOM. Revised version submitted to Climate Dynamics.
- Häkkinen S. and G.L. Mellor (1989): Modeling the Seasonal Variability of a Coupled Arctic Ice-Ocean System. *J Geophys. Res.*, 97 (C12), 20,285-20,304
- Kauffman B.G and W.G. Large (2002): The CCSM Coupler, Version 5.0, Combined User's Guide, Source Code Reference and Scientific Description. Community Climate System Model, National Center for Atmospheric Research, Boulder, CO, USA. <http://www.cesm.ucar.edu/models>
- Mellor G.L. and L. Kantha (1989): An Ice-Ocean Coupled Model. *J Geophys Res.*, 94 (C8), 10,937-10,954.
- Shi, X. S., M. Ødegaard, Ø. Sætra, J. Albretsen and L. P. Røed, 2000: Some preliminary results coupling a simplified, isopycnic coordinate ocean model (MICOM) to DNMI's ice model (MI\_IM). Reg Clim General Technical Report No. 4., 165-170. (Available from Norwegian Institute for Air Research, P.O. Box 100, N-2007 Kjeller, Norway).
- Sætra, Ø., C. Wettre and L. P. Røed, 1998: Coupled ice-ocean modelling under RegClim. RegClim General Techn. Rep. No. 1, 107-118. (Available from Norwegian Institute for Air Research, P.O. Box 100, N-2007 Kjeller, Norway).
- Sætra, Ø., L. P. Røed and Jon Albretsen, 1999: The DNMI RegClim ice model. RegClim General Techn. Rep. No. 3, 55-65. (Available from Norwegian Institute for Air Research, P.O. Box 100, N-2007 Kjeller, Norway).



## **Parameterization of sea ice albedo in climate models**

**by**

**Morten Køltzow**

Norwegian Meteorological Institute (met.no),Oslo

Albedo may be defined as the reflected solar radiation at the surface divided with the incoming solar radiation. At sea ice surfaces high albedo is present much of the year. However during summer, the albedo decreases and the surface albedo is showing a pronounced annual cycle. During the Surface Heat Budget of Arctic Ocean (SHEBA), components of the surface heat energy budget were measured (Persson et al., 2002). Radiation terms dominates the energy budget at the sea ice surface, and during summer the net energy input in to sea ice is dominated by the solar component. High amount of energy is available, but even during summer large parts are reflected back to the atmosphere. Due to this the surface albedo is an important parameter for the sea ice surface climate.

The surface albedo is dependent on several factors. When snow is present the albedo increases, but the albedo of snow is dependent on grain size, which again is dependent on snow age, if it is wet or dry and temperature (Grenfell et al., 1994, Curry et al., 1996). For bare sea ice and no snow, the albedo may depend on type of ice (young ice, multi year ice), ice thickness, and brine volume and melting/non-melting conditions (Perovich et al., 1981, Curry et al., 1996). In addition, formation of melt ponds during summer decreases the surface albedo. The albedo of melt ponds are dependent on depth, sediments in the water and the under laying ice (Tschudi et al., 2001). Typically values of albedo are 0.7-0.9 for snow, 0.5-0.7 for bare sea ice and 0.2-0.4 for melt ponds. In addition to surface characteristics, the surface albedo also depends on zenith angle and cloud cover (Grenfell et al., 1994, Curry et al., 1996).

In most climate models the sea ice albedo is parameterized in a very simplified manner. The simplest parameterization that exists is just to use a constant value, which is done in several of the ARCMIP simulations (<http://www-pcmdi.llnl.gov/amip>). On a yearly average this can give reasonable results, but the annual cycle is non-existing. A common way to do the

parameterization is however to let the albedo be dependent on the surface temperature. REMO and HIRHAM are examples of models using such a scheme. They have a maximum albedo of 0.85 and 0.75, respectively for -3.0C and -1.5C and colder. The albedo is then reduced linearly to a minimum albedo of 0.55 at the melting point. Other schemes distinguish between snow and ice. Mellor and Kantha (1989) do this, with a snow albedo of 0.82, melting ice 0.64, and non-melting ice with 0.71. Another scheme which distinguishes between snow and ice is the NCAR scheme (Collins et al., 2002). NCAR divide the albedo into two parts, one albedo at visible- and one at near infrared wavelengths. The albedo in each of the wavelengths is dependent on the surface temperature in a similar way as described by HIRHAM and REMO. The NCAR scheme does also distinguish between snow-covered- and bare sea ice. Melia (2002) is an example of how snow age can be used as an input to the albedo scheme. After a heavy snow fall the albedo is increased to a maximum albedo (0.85) and then decreases to new snow falls or a minimum value (0.50) is reached. When no snow is present they just distinguish between melting (0.50) and non-melting ice (0.71).

To test the different schemes described above (not the constant ones), they were forced with observations from the SHEBA data set (<http://sheba.apl.washington.edu/>). Figure 1 shows observed and simulated albedo. The two thick black lines are observed albedo. The highest observed albedo is taken at the SHEBA tower, while the other is an average albedo for a 200m long line observed during summer. This last albedo is a good estimate of the area albedo as it includes melt ponds (Perovich et al., 2002). Comparison with simulated values is therefore done with the line albedo when this is available and with the tower albedo during winter/spring.

In winter and spring HIRHAM has too low albedo, while the other schemes seem more reasonable, but do not show the same variability as the observations. In June when the snow melts, HIRHAM and REMO underestimate the albedo while the three other schemes are too high. In the summer all simulations overestimates the albedo by up to 30%. That no schemes include melt ponds may explain some of this overestimation.

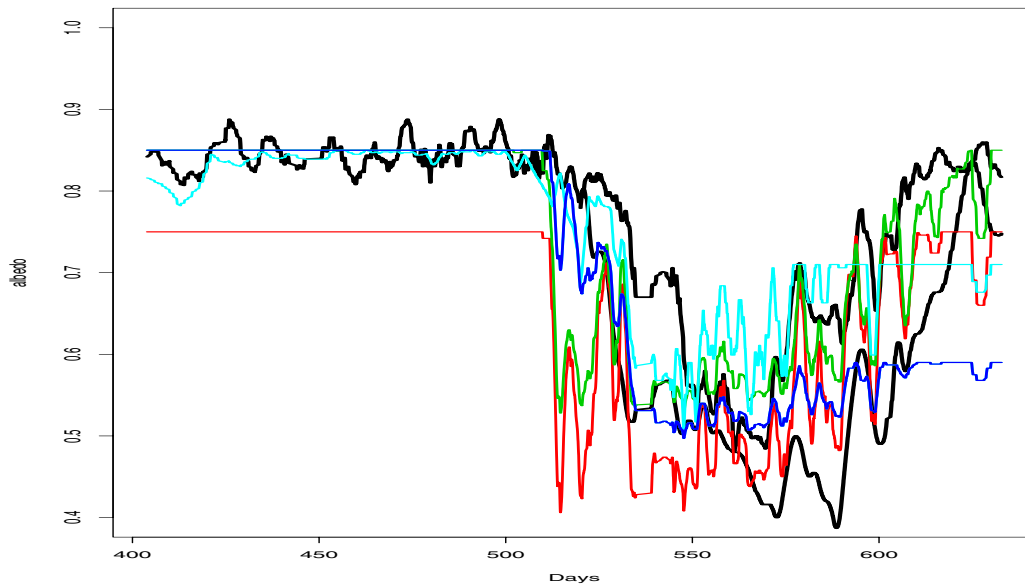


**Figure 1.** Simulated albedo and observed albedo at SHEBA. Observed (black) albedo at tower and albedo line (representative of an area, lower black curve during summer). Simulated albedo from HirHam (red), REMO (green), NCAR (dark blue) and Melia (light blue). Mellor & Kantha (1989) not shown.

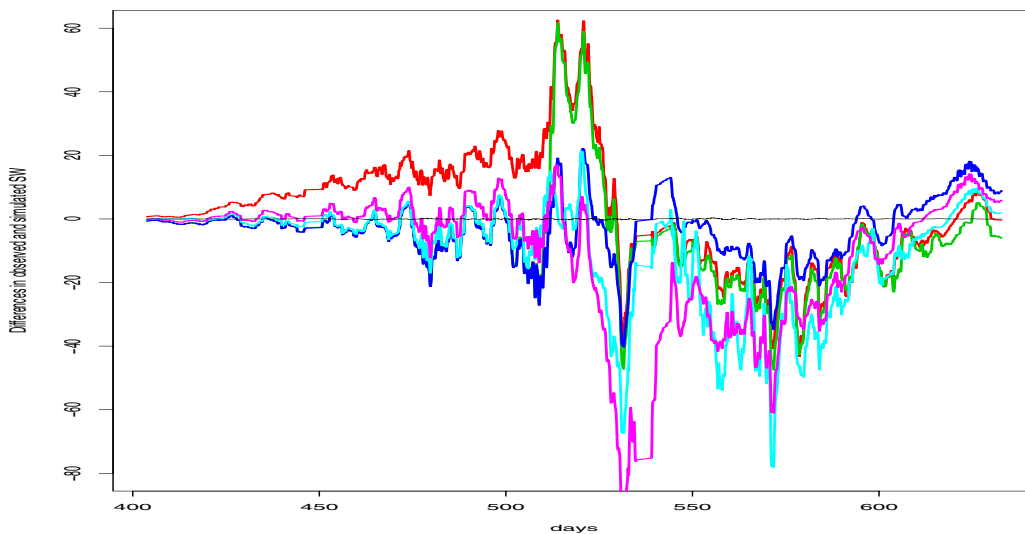


**Figure 2.** Differences between absorbed solar radiation observations and absorbed solar radiation by using albedo from HIRHAM (red), REMO (green), NCAR (dark blue), Melia (light blue) and Mellor & Kantha (pink).

The impact each scheme has on the surface energy budget is shown in figure 2 and table 1. Regarding total energy input to the sea ice, HIRHAM seems to have the best scheme. However in this scheme, too much energy is put into the sea ice in winter and spring, which is

compensated by too little input in summer. In general it looks like the NCAR scheme has a better annual cycle, but in average too high albedo and too little energy absorbed. Melia (2002) and the Mellor and Kantha (1989) schemes has in the summer very high albedo and underestimates the absorbed energy by 30-40 W/m<sup>2</sup> in monthly means.

	Obs	HirHam	Remo	NCAR	Melia	M&K
February	0.0	1.4	-1.2	-1.2	-0.3	-0.4
March	0.0	6.1	-1.1	-1.2	-0.4	1.0
April	0.0	11.9	-2.2	-2.3	-1.5	2.1
May	0.0	15.7	-4.8	-5.1	-3.8	1.4
June	0.0	22.9	6.6	-11.0	-10.4	-11.9
July	0.0	-9.3	-12.6	-7.3	-27.7	-43.9
August	0.0	-22.3	-24.6	-14.2	-38.8	-34.0
September	0.0	-7.1	-9.4	2.2	-8.5	-3.3
Total	0.0	2.4	-7.8	-5.1	-11.2	-11.1

**Table1.** Monthly means of differences between observed absorption of solar radiation (W/m<sup>2</sup>) and simulated values using the different albedo schemes. Positive values imply that the albedo schemes absorb more solar energy than measured. The observed absorption use the tower albedo from February to May and the line albedo from June to September (best estimate of observed surface albedo).

In summary this test shows that none of the tested schemes behave convincing, and that especially in the summer too much solar radiation is reflected at the surface. The positive bias in albedo in summer may be explained with the fact that none of the schemes include melt ponds.

The work with sea ice albedo will continue with the aim of developing a new and better scheme suitable for use in coupled climate models.

### **Acknowledgement:**

This work is partly supported by the Research Council of Norway under the national project RegClim (grant no. 155976/720), the EU project GLIMPSE (EVK2-2001-00337) and the EU project EUROCLIM (IST-2000-28766).

## References:

- Collins, W. D., J. J. Hack, B. A. Boville, P. J. Rasch, D. L. Williamson, J. T. Kiehl, B. Briegleb, J. R. McCauley, C. Bitz, S.-J. Lin, R. B. Rood, M. Zhang and Y. Dai, 2002, Description of the NCAR Community Atmosphere model (CAM2).
- Curry J. A., W. B. Rossow, D. Randall and J. L. Schramm, 1996, Overview of Arctic Cloud and Radiation Characteristics. *Journal of Climate*, 1996, 1731-1764
- Grenfell T. C., S. G. Warren and P. C. Mullen, 1994, Reflection of solar radiation by the Antarctic snow surface at ultraviolet, visible, and near-infrared wavelengths. *Journal of Geophysical Research*, Vol 99, D9, 18669-18684.
- Melia, S., 2002, A global coupled sea-ice-ocean model, *Ocean Modelling*, 4, 137-172.
- Mellor, G. L. & L. Kantha, 1989, An Ice-Ocean Coupled Model, *Journal of Geophysical Research*, vol 94., C8, 10937-10954.
- PCMDI, 2003, The PCMDI home page, <http://www-pcmdi.llnl.gov/amip>
- Perovich, D. K and T. C. Grenfell, 1981, Laboratory studies of the optical properties of young sea ice, *Journal of Glaciology*, vol. 27, no. 96.
- Perovich, D. K., T. C. Grenfell, B. Light, P. V. Hobbs, 2002, Seasonal evolution of the arctic sea ice albedo. *Journal of Geophysical Research*, vol 107, NO. C10, 8044, doi: 10.1029/2000JC000438, 2002.
- Persson, P. O. G., C. W. Fairall, E. L. Andreas, P. S. Guest and D. K. Perovich, 2002, Measurements near the Atmospheric Surface Flux Group tower at SHEBA: Near-surface conditions and surface energy budget. *Journal of Geophysical Research*, Vol. 107, NO.C10, 8045, doi:10.1029/2000JC000705, 2002.
- SHEBA, 2001, The SHEBA home page, <http://sheba.apl.washington.edu/>
- Tschudi, M., J.A. Curry, and J.M. Maslanik, 2001, Airborne observations of summertime surface features and their effect on surface albedo during FIRE/SHEBA. *J. Geophys. Res.*, Vol 106, no. D14, 15,335-15,344.



# Regional Uncertainties in Climate Projections due to Sensitivity of the Atlantic Meridional Overturning Circulation (AMOC)

by

Asgeir Sorteberg<sup>1</sup>, Helge Drange<sup>1,2,3</sup> and Nils Gunnar Kvamstø<sup>1,2</sup>

<sup>1</sup>Bjerknes Climate Research Centre, University of Bergen, Norway.

<sup>2</sup>Geophysical Institute, University of Bergen, Norway.

<sup>3</sup>Nansen Environmental and Remote Sensing Center, Norway

## Abstract

Four simulations with a 1% per year increase in CO<sub>2</sub> (CMIP2 run) have been performed with the coupled Bergen Climate Model (BCM). The runs were started in different phases of the thermohaline circulation to assess possible uncertainties in climate change scenarios to the initial state and fate of the AMOC.

The two simulations started at high AMOC experienced a strong AMOC reduction (approx. 5 Sv reduction at doubling of CO<sub>2</sub>) while the two started close to minimum AMOC showed a weaker response (approx. 1 Sv reduction). However subtracting the AMOC of the control integration for the same time period for the different CMIP2 runs showed that the response due to increased CO<sub>2</sub> was quite similar in all four simulations (1.8-2.6 Sv reduction at doubling of CO<sub>2</sub>). This indicates that the fate of the AMOC in an increased CO<sub>2</sub> scenario is rather dependent on the initial state of the ocean.

Large scale temperature and precipitation changes were relatively similar in the four simulations, however simulated north Atlantic/north European climate change in general showed a stronger response in the low AMOC initial state/low AMOC response simulations. This might be explained by the fact that the heat transport in the ocean was less reduced in the low AMOC initial state/low AMOC response simulations and therefore to a lesser extent counteracted the general temperature increase due to increased CO<sub>2</sub> in this region. However there are also indications that the low AMOC response gave a long-term (several decades) feedback back on the north Atlantic atmospheric winter circulation giving a stronger long-term (several decades) increase in NAO when the AMOC response was low. This stronger NAO response will then feed back on the AMOC response. If this is the case, the AMOC response might both influence the oceanic and atmospheric northward heat transport in this region. The integrated effect of these changes will have a pronounced effect on the strength of the warming and the intensification of the water cycle in the area.

## 1. INTRODUCTION

There are three main processes that make the oceans circulate: tidal forces, wind stress, and density differences. The density of seawater is controlled by its temperature (thermo) and its salinity (haline), and the circulation driven by density difference thus called the thermohaline circulation.

The critical part of the thermohaline circulation (THC/AMOC) is the sinking in the North Atlantic Ocean. This occurs here (and not in the North Pacific) because the Atlantic is much more saline (and hence, denser). It is more saline because it is warmer (more evaporation of fresh water increases the salinity of the sea water). It is warmer in the North Atlantic because warm water is brought by the thermohaline circulation from the tropical and South Atlantic. To some extent, therefore, the AMOC appears to be self-sustaining. And if some event occurs to break this self-sustaining chain of processes, then there is the potential for the circulation to break down rapidly (i.e., over several decades) and to remain in a reduced-circulation state for several centuries.

Some fairly simple models of the world's oceans do simulate a rapid break down of the AMOC, when the density of the water in the North Atlantic Ocean is lowered by adding fresh water (rain) and/or by warming. Increased rainfall and warming over the North Atlantic are both expected as a result of increased greenhouse gas concentrations, and so it can be argued that global warming may cause a rapid collapse of the thermohaline circulation. The self-sustaining system described above is, however, much more complex in reality, and the more complete climate models, that take some of these complexities into account, generally simulate only a gradual weakening of the AMOC in response to global warming. Nevertheless, observations and palaeoclimate evidence both indicate that the AMOC has fluctuated both recently and in the distant past.

The oceanic heat transport in the Atlantic Ocean has an obvious and well-known impact on climate. Most of the heat transport in this basin is a consequence of the warm-to-cold water conversion associated with the thermohaline circulation. To the extent that variations of the thermohaline circulation on decadal-to-centennial time scales lead to changes in SST and ocean heat transports, they are therefore of direct interest to the RegClim project.

## **1.1 ATMOSPHERIC FORCING**

Observations have shown that the water mass distributions in the subpolar North Atlantic change on decadal time scales. In particular, convection activity in the source regions for the deep thermohaline circulation has been observed to undergo substantial changes on decadal time scales. The most likely cause of this variability is atmospheric forcing. SST-variability observed during the past decades has also been linked to variations in the thermohaline flow, although quantitative estimates of thermohaline circulation variability are lacking.

The sensitivity of the thermohaline circulation to changes in atmospheric conditions is presently not well known, and different models disagree on this issue. Little can be concluded from observations as the instrumental record so far does not allow to infer variations in thermohaline circulation intensity.

## **1.2 FEEDBACK BACK ON THE ATMOSPHERE**

Results from coupled models indicate that multi-decadal thermohaline circulation variations of moderate amplitude have a feedback on atmospheric climate. In a multi-century integration with a coupled model, Delworth et al. (1997) found pronounced oscillations of oceanic temperature and salinity in the Greenland Sea. These oscillations, with a time scale of approximately 40-60 years, involve large-scale interactions between Arctic fresh water and ice export, the intensity of the East Greenland current, and fluctuations of the intensity of the thermohaline circulation in the model North Atlantic. The mechanisms causing a feedback of thermohaline circulation variations to the atmosphere are however not well understood. In particular it is not known which pathways for propagation within the ocean are most relevant, and which factors determine the time scale of coupled oscillations. It seems however likely that long term changes in oceanic heat transport will feedback back on the long term atmospheric heat transport and that long term local SST changes in the north Atlantic will feedback on the formation and development of low-pressure systems in the north Atlantic.

### **1.3 RESPONSE DUE TO INCREASED CO<sub>2</sub>**

Most climate models predict a substantial change of atmospheric conditions towards warming and intensification of the water cycle in high latitudes during the next decades, due to anthropogenic emissions of greenhouse gases. A quantitative understanding of the dynamical response of the thermohaline circulation to changes in the fluxes at the sea surface is therefore important to assess the fate of the north European climate in an increased CO<sub>2</sub> scenario.

The sensitivity of a model's thermohaline circulation to changes in atmospheric fluxes depends on the type of model used. Coarse-resolution ocean-only models using mixed boundary conditions tend to be unrealistically sensitive to freshwater inflow in the convection areas. Both coupled models and ocean-only models that include a representation of atmospheric heat transport are much less sensitive, and agree reasonably well with each other when the same ocean model is used. Some models suggest that the present thermohaline circulation state may be close to a transition point (Tziperman et al., 1994). Furthermore, sensitivity of the thermohaline circulation appears to depend strongly on model parameters such as heat and salt diffusion, models with less diffusion being more sensitive. The model resolution potentially has also a significant impact on model sensitivity, and high-resolution ocean models with a proper representation of deep overflows have been found to be less sensitive. The dependence of the thermohaline circulation sensitivity on critical model parameters and on the mean climate state is of importance.

In this report we investigate the response of the AMOC to increased CO<sub>2</sub> and its implications for uncertainties in the climate projection for the Northern European climate. In addition the sensitivity of the initial state of the AMOC will be discussed.

## **2. MODEL SETUP**

The Bergen Climate Model (BCM) consists of the atmospheric model ARPEGE/IFS, together with a global version of the ocean model MICOM including a dynamic-thermodynamic sea-ice model. The coupling between the two models is done with the software package OASIS. The atmosphere model has a linear T<sub>L</sub>63 (2.8°) resolution with 31 vertical levels from the

surface to 0.1 hPa. MICOM has an approximately  $2.4^\circ$  resolution with 24 isopycnal vertical levels. Key quantities regarding climatic means and variability of the control integration have been evaluated against available observations in Furevik et al. (2003).

Evaluation of the variability and the stability of the thermohaline circulation in the BCM has been investigated in a series of papers (Gao et al., 2003; Nilsen et al., 2003; Dutay et al., 2002; Bentsen et al., 2002; Otterå et al., 2003a; 2003b; 2003c). In general the model's AMOC strength and variability is realistic with the AMOC being among the less sensitive to freshwater perturbations.

In this study we have conducted 4 simulations using an increase in  $\text{CO}_2$  of 1% per year in 80 years (CMIP2 integration). The simulations are started in different phases of the AMOC (max, min, increasing and decreasing phase) to investigate the sensitivity of the simulations to the initial state of the AMOC (see Figure 1). The anomalies in the AMOC where the different simulations are performed are around 2-3 Sv. More simulations are underway so this should be considered as preliminary results only.

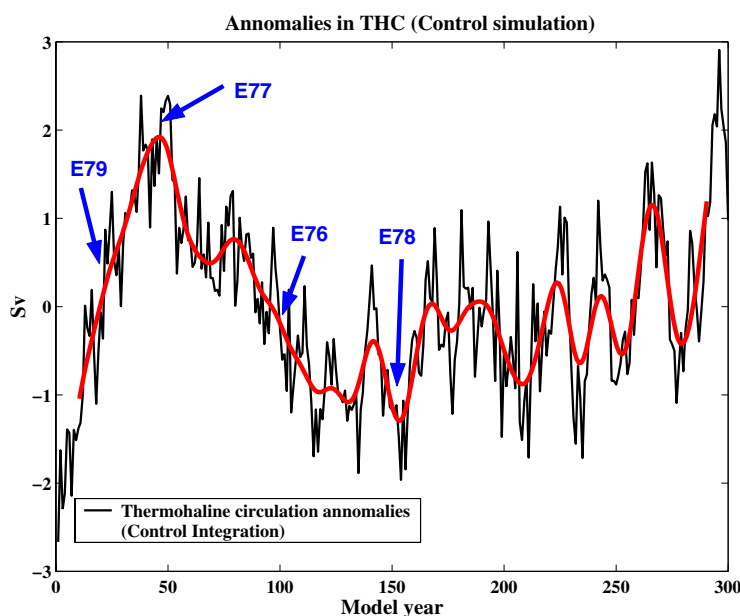


**Figure 1:** The AMOC anomalies in the control run and the initial state of the AMOC in the different CMIP2 simulations.

### 3. FATE OF THE AMOC DURING INCREASED CO<sub>2</sub>

Figure 1 shows the AMOC in the 300-year control run and the Figure 2 shows the 4 CMIP2 simulations. The responses are quite different for the two started in high initial state compared to the two started in low initial state. The two started in high initial state has a reduction of 4.1-5.7Sv during CO<sub>2</sub> doubling compared to a 0.3-0.8 Sv reduction for the two started in low initial state. However if we subtract the control run for the same time period the isolated response due to CO<sub>2</sub> is quite similar in all simulations with a reduction of 1.8-2.6 Sv at doubling of CO<sub>2</sub> (Figure 2). Thus the initial state of the AMOC seems to play an important factor in the long-time response of the AMOC. Since poleward oceanic energy transport is approximately linear to the AMOC strength the reduction in poleward oceanic energy transport is much stronger in the two simulations starting near the max AMOC. AMOC response due to increased CO<sub>2</sub> differ quite a lot from model to model ranging from no response (ECHAM4/OPYC) to a large (8-12Sv) reduction compared to the control run in some models (ECHAM3/LSG, CSIRO). Thus the THC response in the BCM is quite moderate compared to many of the other models.

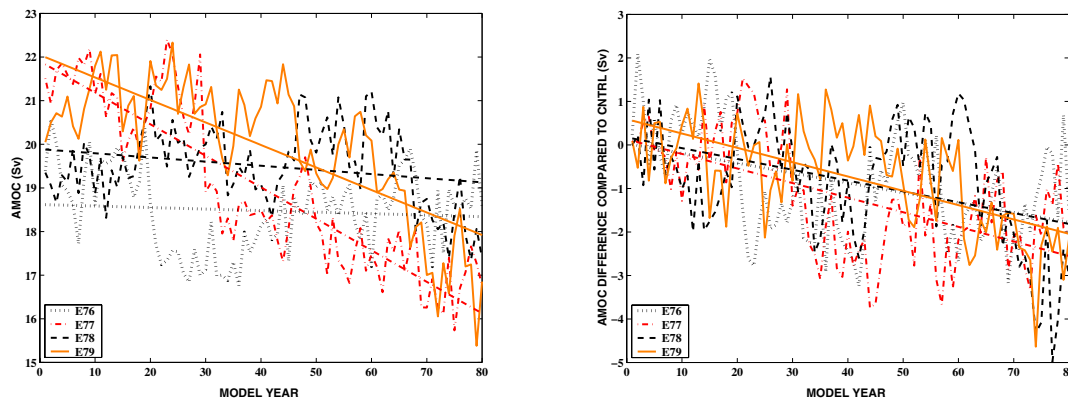


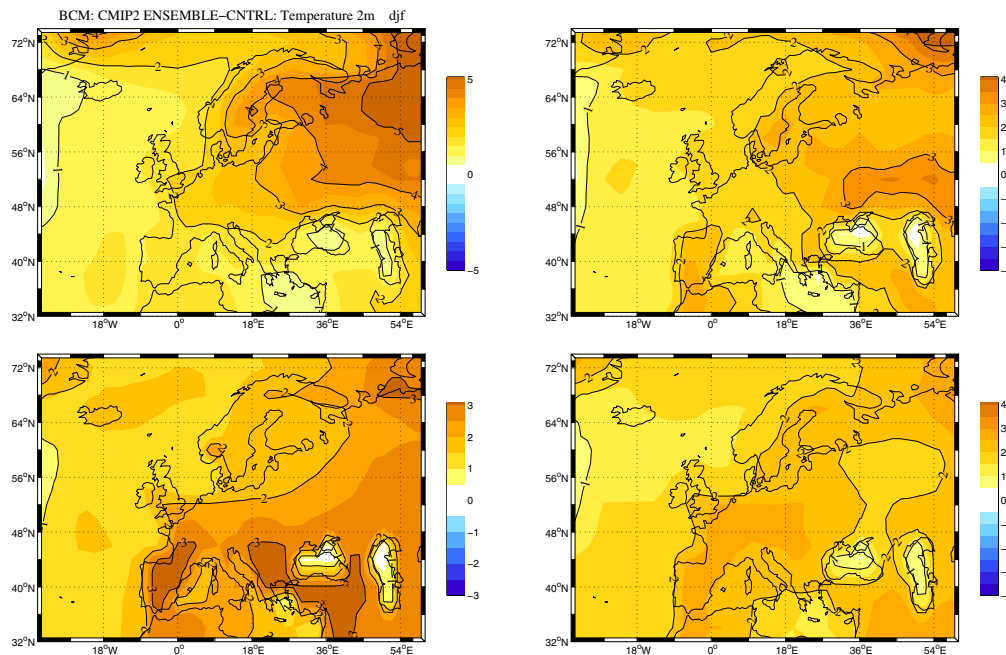
**Figure 2:** The AMOC response in the different CMIP2 runs (left). The relative response compared to the control over the same time period and the linear trend.

## 4. TEMPERATURE AND PRECIPITATION CHANGES

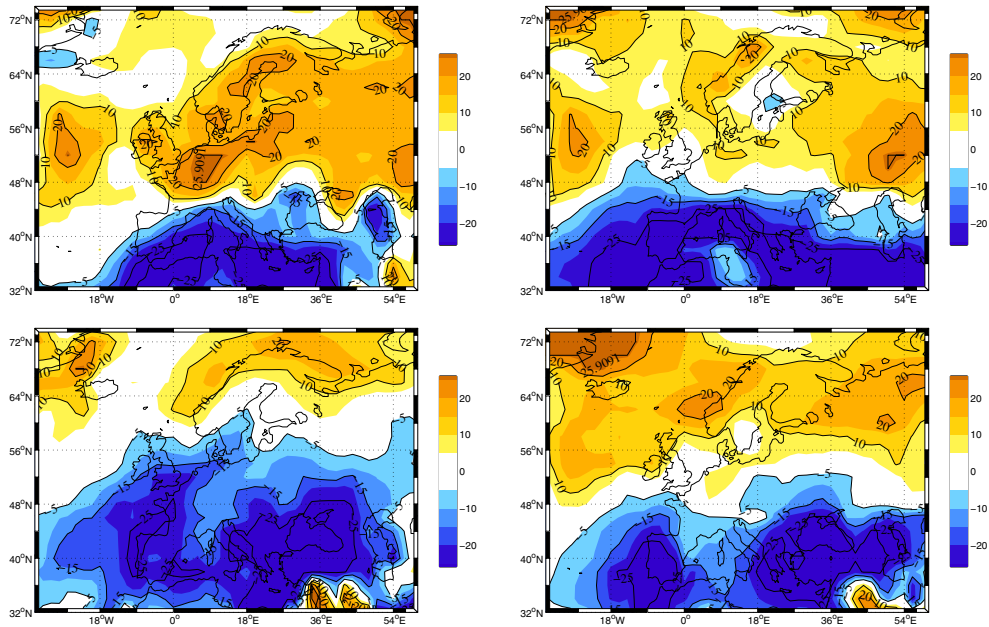
### 4.1 THE EUROPEAN AREA - ENSEMBLE MEANS

Figure 3 shows the ensemble mean changes of temperature at doubling of CO<sub>2</sub> (avg. over last 20 years) in different seasons.

The largest temperature increase was in wintertime with a gradient in temperature changes from south-west to north-east with maximum changes in north-east Russia of 4-5°C. During summer the pattern is opposite with the largest changes in southern Europe of approximately 3°C. The spring and autumn responses are somewhat lower in the order of 2-2.5°C for most of the European area. In general the western coastal areas have less warming than the inland. This is partly due to the ‘real’ influence from the ocean, but partly due to the use of fractional land/ocean in the coastal gridcells which smooths the land/ocean temperature change gradients.



**Figure 3:** Ensemble mean 2m temperature changes (°C) during doubling of CO<sub>2</sub> (mean over the last 20 years of all simulations) DJF (upper left), MAM (upper right), JJA (lower left) and SON (lower right)



**Figure 4:** Ensemble mean precipitation changes (%) during doubling of CO<sub>2</sub> (mean over the last 20 years of all simulations) DJF (upper left), MAM (upper right), JJA (lower left) and SON (lower right)

Precipitation changes (Figure 4) show a clear 'NAO-like' pattern with increased precipitation in northern Europe and reduction in southern parts. In winter time the increase is in the order of 10-25% during doubling of CO<sub>2</sub> and the reduction in the southern part is about the same amount. During summertime a reduction in precipitation is seen over all Europe except in the north-western parts.

#### 4.2 DIFFERENCES IN THE SIMULATION OVER THE NORDIC AREA COMPARED TO OTHER MODELS

To investigate more in detail the differences in the different BCM runs and compare to other global coupled model results, we have chosen three areas representative of the south-western coast of Norway, the south-eastern part of Norway/Sweden and northern Norway/Finland. Areas chosen are displayed in Figure 5. Thus the results are for mean changes over typically 3 to 8 grid squares for the different models. Note that the results are mean over both ocean and land-points.

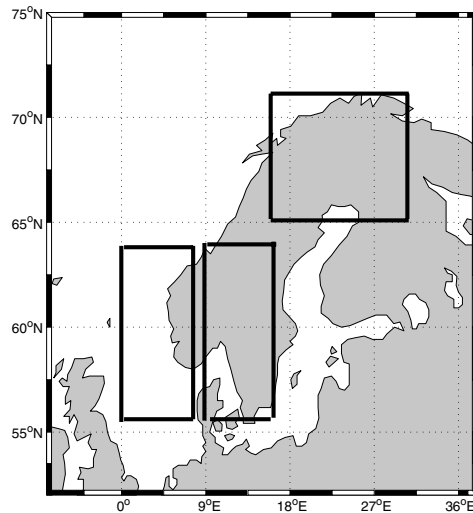


**Figure 5:** The three areas chosen for calculating mean changes. South-western Norway: 56-63°N and 0-8°E; South-eastern Norway/Sweden: 56-63°N and 9-16°E; Northern Norway/Finland: 65-71°N and 16E-29E.

Figure 6 show the mean DJF temperature and precipitation for the control runs of the different models. Compared to the observations there is a quite large scatter in both temperature and precipitation. Surprisingly the different observational estimates also differ quite much. There seems to be a tendency for underestimation of precipitation in most models over the south-western area. This is probably due to the lack of topographical resolution of the Norwegian mountains, which constitutes a large amount of the precipitation within the chosen area. More surprisingly is the 7°C spread in temperature. The simulations range from a 0 to 2.3°C increase in temperature and a 1% reduction to a 18% increase in precipitation. Figure 6 shows the mean DJF temperature and precipitation response in the different models over the region. The BCM temperature and precipitation increase in the south-western area range from 0.99 to 1.76°C and 5-14%, respectively in the 4 runs during DJF. The precipitation changes span a large part of the range of precipitation responses given by the other models with the two runs started in the low AMOC part with a low AMOC response in the upper part with high temperature and precipitation changes and the two in high AMOC initial state and high response in the lower temperature and precipitation response range. The difference related to the AMOC will be discussed in section 5.

In the south-eastern area there is no systematic underestimation of the precipitation in the control runs as seen in the western area and the different observational estimates agree quite well. The precipitation and temperature changes range from a 3-22% and 0.3-3.8 C increase,

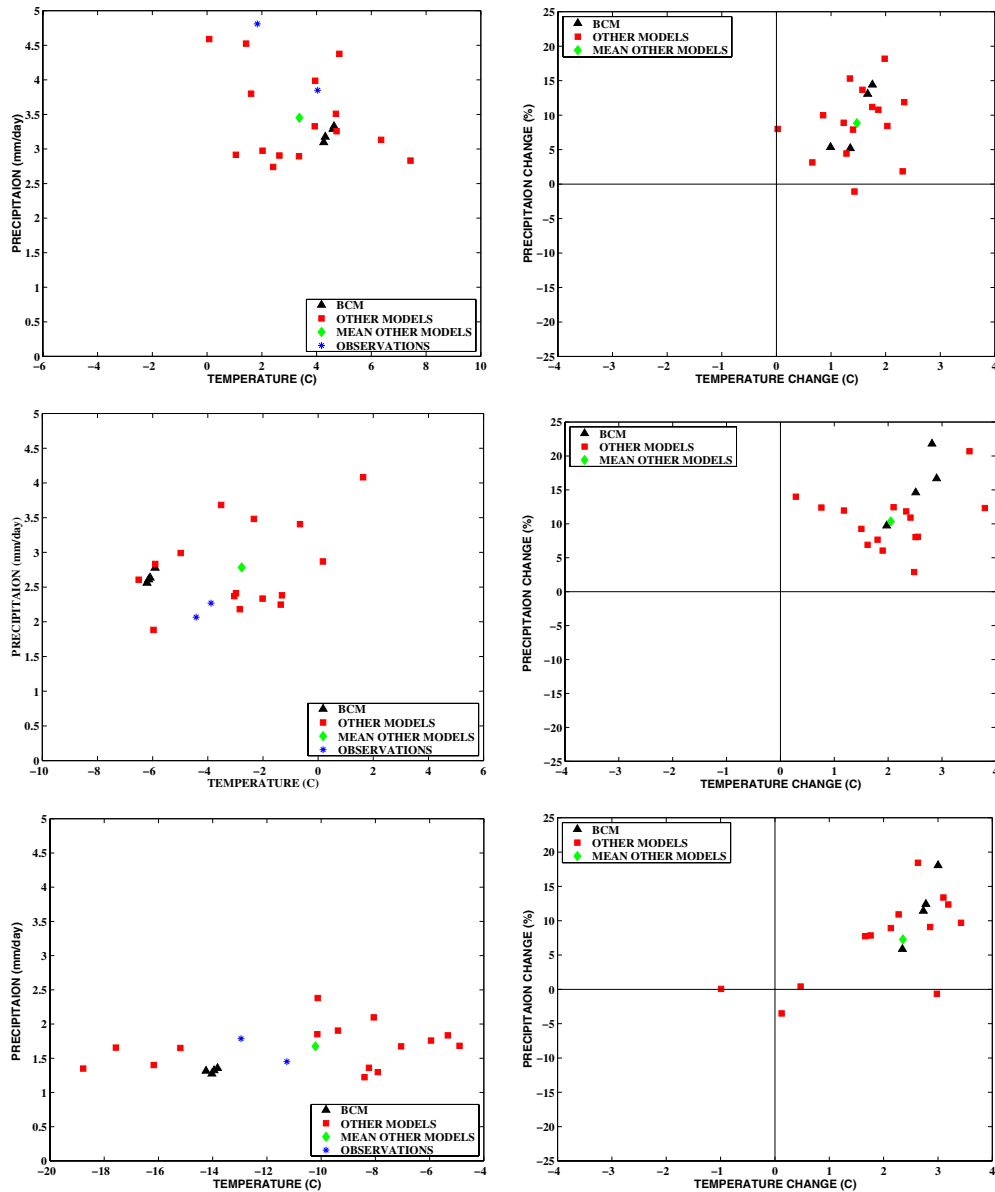


**Figure 6:** DJF temperature ( $^{\circ}\text{C}$ ) and precipitation (mm/day) from the control runs (left) in the south-western (upper), south-eastern (middle) and northern (lower) area (see figure 5 for the areas). Observations are NCEP (1950-1989 mean) and Jones (1961-1990 mean) temperatures, CMAP (1979-1999 mean) and GPCP Ver. 2 (1979-1999 mean) precipitation. DJF temperature ( $^{\circ}\text{C}$ ) and precipitation (%) changes (avg. over the last 40 years of the CMIP2 runs) (right) in the south-western (upper), south-eastern (middle) and northern (lower) area.

<b>SEASON</b>	<b>TEMPERATURE (C)</b>	<b>PRECIPITATION (MM/DAY)</b>
<b>South-western Norwegian coast</b>		
<b>DJF</b>	0.99-1.76	0.17-0.45
<b>MAM</b>	1.14-1.76	0.11-0.23
<b>JJA</b>	0.71-1.32	-0.02-0.07
<b>SON</b>	1.03-1.42	0.24-0.54
<b>South-eastern Norway/Sweden</b>		
<b>DJF</b>	1.97-2.90	0.27-0.56
<b>MAM</b>	1.63-2.52	0.10-0.40
<b>JJA</b>	0.92-1.75	-0.17-0.13
<b>SON</b>	1.41-1.79	0.19-0.27
<b>Northern Norway/Finland</b>		
<b>DJF</b>	2.35-3.00	0.08-0.24
<b>MAM</b>	1.39-1.81	0.03-0.21
<b>JJA</b>	1.26-1.95	0.04-0.28
<b>SON</b>	1.69-1.88	0.07-0.32

**Table 1:** The range of seasonal temperature (°C) and precipitation (mm/day) changes in the different BCM CMIP2 runs (avg. over the last 40 years) in the chosen areas (see figure 5).

respectively. As in the south-western area the BCM ensemble spans out a large portion of the different precipitation responses (10-22%) given by the other models, but with less spread in temperature responses (2-2.9°C increase). The models seem to estimate DJF precipitation quite well in the northern area however there are large discrepancies in the mean temperatures which spans 14°C with 11 of 16 models being too warm.

The temperature changes are also quite different ranging from a 1°C cooling in one model to a 3.3°C warming in another this is followed by a wide range of precipitation responses from a 4% reduction to a 19% increase. As seen in the two other areas the different BCM simulations have a large scatter in the precipitation response ranging from a 6-18% increase and with temperature changes ranging from 2.4-3°C. The range of BCM temperature and precipitation changes at all seasons are given in Table 1.

## **5. THE INFLUENCE OF AMOC INITIAL STATE AND FATE ON THE SIMULATED CHANGES**

### **5.1 TEMPERATURE AND PRECIPITATION CHANGES**

Figure 7 shows the precipitation and temperature differences relative to the control in the same time period for the last 40 years of the simulations for the different areas (see figure 5). The way the simulations are conducted it is difficult to assess if the changes in temperature response is a function of the initial AMOC state or the AMOC changes during the run. Note however that by subtracting the control over the same time-period as the CO<sub>2</sub> simulation itself we get rid of any drift or long term oscillations in the AMOC that is affecting both the control and the CO<sub>2</sub> simulations in that time period.

The two simulations that started near minimum AMOC and experiencing the smallest reduction (E76 and E78) both show a higher temperature change than the two started at max AMOC and having a stronger reduction, in all seasons in the south-western and south-eastern areas. The precipitation response is however less clear except in DJF where there is a higher precipitation change in both low AMOC response simulations in both areas.

Table 2 shows the mean relative change of the low response simulations (E76 and E78) compared to the mean of the high response simulations (E77 and E79) (avg. over the last 40 years) over the different areas at different seasons. Except DJF in the northern area all seasons at all the areas experienced a higher mean response in the low initial AMOC/low AMOC response case. The relative difference range from 7-193% with most responses being around 25-60% higher in the low initial AMOC/low AMOC response case.

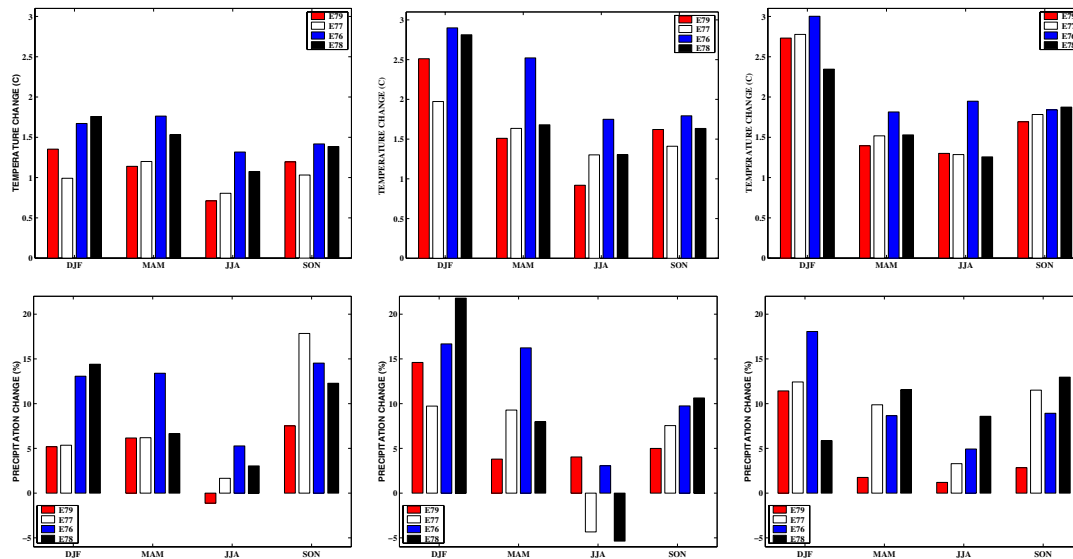


**Figure 7:** BCM Seasonal temperature ( $^{\circ}\text{C}$ ) (upper) and precipitation (%) (lower) changes (averaged over last 40 years) in the different CMIP2 runs in the south-western (left), south-eastern (middle) and northern (right) areas (see figure 5 for the areas).

SEASON	$\Delta\text{TEMP}$ (%)	$\Delta\text{PRECIP}$ (%)	$\Delta\text{TEMP}$ (%)	$\Delta\text{PRECIP}$ (%)	$\Delta\text{TEMP}$ (%)	$\Delta\text{PRECIP}$ (%)
	Norwegian west coast		Southern Norway		Northern Norway	
<b>DJF</b>	46	147	27	52	-3	3
<b>MAM</b>	41	61	34	80	15	78
<b>JJA</b>	58	*	38	*	24	193
<b>SON</b>	26	9	13	62	7	57

**Table 2:** Relative difference (mean over last 40 years) in temperature and precipitation changes between the 2 simulation in low AMOC state and low response and the 2 in high AMOC state and high response ( $(\text{mean}(E76 + E78) - \text{mean}(E77 + E79)) / \text{mean}(E77 + E79) * 100$ ) in the different areas (see figure 5). Unit: %. \*Insignificant changes in the mean( $E77 + E79$ ) response.

## 5.2 CHANGES IN WINTERTIME CIRCULATION

Figure 8 shows that the pressure difference between Iceland and Gibraltar (taken as the difference between the grid square over Iceland and Gibraltar) on average increased by approximately 2.5 hPa in the CMIP2 runs (using data for the last 40 years of the CMIP2 runs). The increase was both due to a reduction/increase in the Icelandic low/Azores high and the movement of the Icelandic low north-eastwards (Figure 8). Thus the model simulated both a movement and an intensification of the Icelandic low.

The change in pressure difference between Iceland and Gibraltar was however not the same in all simulations Figure 8 shows that the simulation started in the low AMOC initial state and with a low response (E76 and E78) had a much stronger change in the pressure difference (approximately 2-3 times stronger).

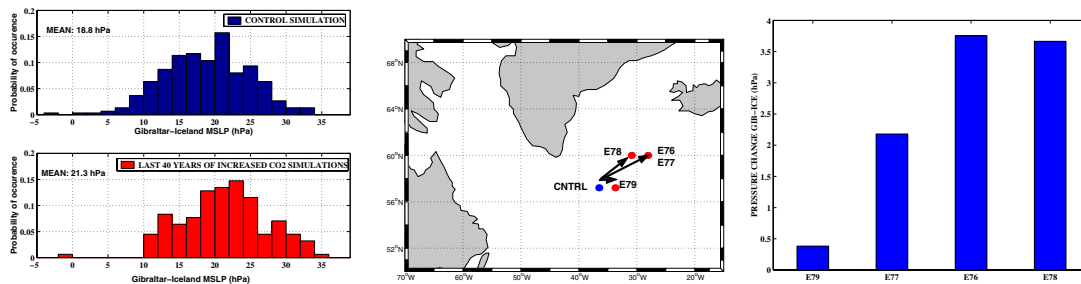


**Figure 8:** Probability of occurrence of the Gibraltar-Iceland DJF MSLP in the control run (upper, left) and in the last 40 years of the CMIP2 runs (lower, left). The mean movement of the DJF Icelandic low during the last 40 years of the CMIP2 simulations compared to the control run (middle). Mean changes in MSLP difference between Gibraltar and Iceland during the last 40 years of the different CMIP2 simulations (right).

Figure 9 shows the mean MSLP changes in the high AMOC response simulations (E77 and E79) compared to the mean MSLP changes of the low AMOC response simulations (E76 and E78) which shows that the pressure differences in the Nordic Sea area is much greater in the low AMOC response cases. This gives some indications of a long term (several decades) feedback from the changes in AMOC back on the atmospheric circulation in the Atlantic area

and might partly explain why the temperature and precipitation changes in northern Europe are higher in the low AMOC response simulations.

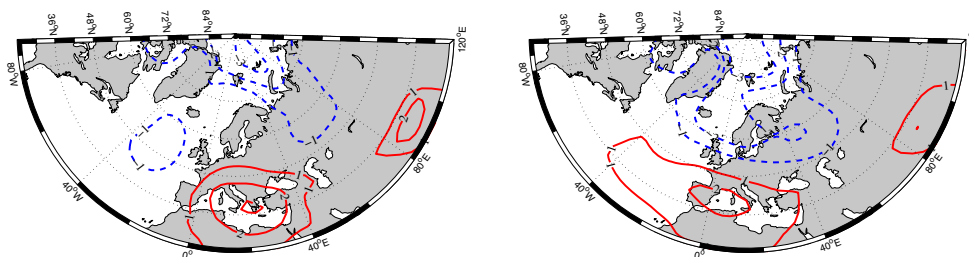


**Figure 9:** DJF mean (last 40 years) MSLP changes in high AMOC response simulations (E77 and E79) (left) and low AMOC response simulations E76+E78 (right)

## 6. REFERENCES

- Bentsen, M., H. Drange, T. Furevik and T. Zhou (2002), Variability of the Atlantic thermohaline circulation in an isopycnic coordinate OGCM, *Clim. Dynam.*, submitted
- Delworth, T. L., S. Manabe, and R.J. Stouffer, 1997: Multidecadal climate variability in the Greenland Sea and surrounding regions: a coupled model simulation. *Geophysical Research Letters*, 24(3), 257-260.
- Dutay, J.-C., J.L. Bullister, S.C. Doney, J.C. Orr, R. Najjar, K. Caldeira, J.-M. Champin, H. Drange, M. Follows, Y. Gao, N. Gruber, M.W. Hecht, A. Ishida, F. Joos, K. Lindsay, G. Madec, E. Maier-Reimer, J.C. Marshall, R.J. Matear, P. Monfray, G.-K. Plattner, J. Sarmiento, R. Schlitzer, R. Slater, I.J. Totterdell, M.-F. Weirig, Y. Yamanaka, and A. Yool (2002), Evaluation of ocean model ventilation with CFC-11: comparison of 13 global ocean models. *Ocean Modelling*, 4, 89-120
- Furevik T., Bentsen, M., Drange, H., Kindem, I.K.T., Kvamstø, N.G., and Sorteberg, A. (2003): Description and Validation of the Bergen Climate Model: ARPEGE coupled with MICOM, *Clim. Dyn.*, *in press*.
- Gao, Y., H. Drange and M. Bentsen (2003), Effects of diapycnal and isopycnal mixing on the ventilation of CFCs in the North Atlantic in an isopycnic coordinate OGCM, *Tellus*, *in press*
- Nilsen, J. E. Ø., Y. Gao, H. Drange, T. Furevik and M. Bentsen (2003): Simulated North Atlantic-Nordic Seas water mass exchanges in an isopycnic coordinate OGCM, *Geophys. Res. Lett.*, 30,
- Otterå, O. H., H. Drange, M. Bentsen, N. G. Kvamstø and D. Jiang (2003a): The sensitivity of the present day Atlantic meridional overturning circulation to anomalous freshwater input, *Geophys. Res. Letters*, submitted

- Otterå, O. H. and H. Drange (2003b): A possible coupling between the Arctic fresh water, the Arctic sea ice cover and the North Atlantic Drift. A case study ,Clim. Dyn., under revision
- Otterå, O. H. H. Drange, M. Bentsen, N. G. Kvamstø and D. Jiang (2003c): Transient response of enhanced freshwater to the Nordic Seas-Arctic Ocean in the Bergen Climate Model, Tellus, submitted
- Tziperman, E., J.R. Toggweiler, Y. Feliks, and K. Bryan, 1994: Instability of the thermohaline circulation with respect to mixed boundary conditions: is it really a problem for realistic models? J. Phys. Oceanogr., 24, 217-232.

# Climate response to anthropogenic aerosol forcing using the Oslo version of NCAR CCM3 coupled to a slab ocean

by

Jón Egill Kristjánsson<sup>1</sup>, Trond Iversen<sup>1</sup>, Alf Kirkevåg<sup>1</sup>, Øyvind Seland<sup>1</sup>,  
Jens Debernard<sup>2</sup>, Lars Petter Røed<sup>1,2</sup>

<sup>1</sup>Department of Geophysics, University of Oslo, Norway.

<sup>2</sup>Norwegian Meteorological Institute, Oslo, Norway.

## Abstract

In order to estimate the climatic impact of anthropogenic aerosols, a set of 50-year simulations have been carried out using an extended version of the NCAR CCM3 (CCM-Oslo) global climate model, coupled to a slab ocean. The extensions consist of prognostic cloud water and a new, detailed treatment of aerosols, developed in RegClim Phase II. The direct and indirect effect of sulfate and black carbon (BC) are calculated, based on a life-cycle scheme that, combined with natural continental and maritime aerosols, enables estimates of size-distributed particle properties. The size distributions account for nucleation, condensation, coagulation, cloud processing and humidity swelling, and are used both for computing optical properties and CCN activation. Separate sets of simulations have been conducted for the direct and indirect aerosol effects. The indirect effect gives a fairly large negative radiative forcing everywhere, and this leads to a globally averaged cooling of 1.3 K. The direct effect has a globally averaged cooling of 0.10 K, but it has a much more complex signature due to partly canceling effects of reflection and absorption, the latter being most pronounced in connection with BC aerosols over highly reflecting surfaces, such as low clouds or deserts. For the indirect effect the largest temperature reduction is found in the Arctic, in particular during fall and winter when the regional contribution to the forcing is small. This is a consequence of a strong ice-albedo feedback at high latitudes, augmented by a positive cloud feedback and the formation of a shallow anticyclone over the Arctic in the dark season. Another signal that is statistically significant is a southward displacement of the ITCZ, due to the inter-hemispheric differences in aerosol forcing. This leads to, e.g., reduced precipitation over the Sahelian region in Africa. Interestingly, this ITCZ displacement is also found in the experiments with the direct effect alone, even though the cooling is much weaker in that case. Finally, we present experiments in which the greenhouse gas concentrations have been altered between present-day and pre-industrial values, in addition to the corresponding assumptions on aerosol emissions for indirect effect estimations. This leads to a globally averaged warming of 0.3 K, but the Northern Hemisphere is actually cooler and drier in the present-day simulations than for the pre-industrial conditions. This indicates that our indirect effect is too strong, at least in the Northern Hemisphere. Possible remedies are discussed, and will be pursued further in the NFR-funded AerOzClim and COMBINE projects.

## 1. Introduction

In this investigation we describe results from simulations of the climate system response to the anthropogenic aerosol forcing that was computed in RegClim Phase II (Iversen and Seland, 2002; Kirkevåg and Iversen, 2002; Kristjánsson, 2002). The purpose is to provide information about the degree of uncertainty in climate change estimates related to aerosol forcing. This uncertainty is due to a combination of uncertainties concerning aerosol burdens and types, chemical processes, transport, aerosol-cloud interactions and radiative processes.

## 2. Experimental setup

All the simulations were carried out using “the Oslo version” of the NCAR CCM3 atmospheric global climate model, coupled to a slab ocean model (see Kiehl et al., 1996, for details). In this way a realistic thermal inertia is obtained for the climate system on multi-decadal time scales. Potential changes in ocean currents due to changes within the climate system are not taken into account. The open (i.e. ice-free) ocean component of the slab ocean model is taken from Hansen et al. (1983). It consists of a prognostic equation for the ocean mixed layer temperature, subjected to fluxes to and from the atmosphere ( $F$ ) and horizontal and vertical heat fluxes within the ocean ( $Q$ ). The ocean mixed layer depth varies according to climatological seasonally varying observational data by Levitus (1982).

For the ice-covered ocean, the mixed layer  $Q$  flux below sea ice is specified so as to yield approximately a present-day sea ice distribution from observations. Furthermore, to avoid excessive ice growth in experimental simulations, the  $Q$  flux is constrained in a globally conserving manner. Sea ice is divided into four layers of uniform thickness, and in each layer a separate heat transfer equation is solved. In the horizontal the sea ice is assumed to completely cover a CCM grid cell. Sea ice is assumed to form at  $-1.9^{\circ}\text{C}$  and to melt at  $0^{\circ}\text{C}$ . Snowfall and consequent variations in snow depth on top of the sea ice are taken into account, but changes in snow depth by compaction over time and by sublimation are ignored. A minimum sea ice thickness of 0.25 m is assumed, to avoid numerical difficulties. In the Arctic the sea ice thickness is not allowed to exceed 3 m, while the maximum ice thickness in the Antarctic is 0.50 m.

The atmospheric model component NCAR CCM3 is described in Kiehl et al. (1998). CCM3 is a state-of-the-art global climate model, run at T42 spectral truncation and with 18 levels in the vertical. Our version of the model contains prognostic cloud water, according to the scheme of Rasch and Kristjánsson (1998).

During earlier phases of RegClim, modules for computing aerosol evolution and the radiative forcing of aerosols through direct and indirect forcing were developed and implemented in NCAR CCM3. The aerosol modules, as well as results from the radiative forcing simulations were described in Iversen and Seland (2002), Kirkevåg and Iversen (2002) and Kristjánsson (2002). Background aerosols, consisting of sea salt, mineral and water-soluble non-sea salt particles are prescribed and size distributed. These size distributions are then modified by adding natural and anthropogenic sulfate and black carbon (BC) into an internal mixture, brought about by condensation, coagulation in clear and cloudy air, and wet-phase chemical processes in clouds. A normally minor fraction of sulfate and BC is externally mixed, produced by clear-air oxidation followed by nucleation, and by emission of primary particles. Starting from emissions of sulfate precursor gases (SO<sub>2</sub>, DMS), sulfate particles (SO<sub>4</sub>) and black carbon (BC), chemical reactions, transport and deposition are computed at every grid point. The largest emission sources are fossil fuel combustion, biomass burning and industrial releases. In the present study, the aerosol forcing modules are allowed to interact with the dynamics of the climate system, enabling calculations of the response to the aerosol forcing.

The simulations are of 50-year duration. There is a spin-up period covering the first 5-10 years, during which the climate gradually changes, especially in the runs with present day aerosol conditions. After this, the model's climate has reached a new equilibrium (Figure 1), and we consequently use the last 40 years of each 50-year simulation in the analysis that follows. In all the simulations the concentrations of sulfate and black carbon are obtained from monthly mean output of 5-year simulations of the present day climate. In reality also the distribution of aerosols will change when the circulations change and adjust during equilibration. This would in turn affect the radiative forcing and hence the dynamic response.

In addition to simulating the climate using present and pre-industrial aerosol emissions, we will also show results from simulations where the greenhouse gas concentrations are allowed to vary between present and pre-industrial conditions. In this way, a crude estimate of anthropogenic climate change is obtained. However, these results cannot be compared directly

to observations, since today's climate is not in equilibrium, because of the large thermal inertia of the oceans.

All the results have been subjected to a t-test, in order to check their statistical significance. We do not show the results of this test explicitly in what follows, but in general all the main features are significant at the 95% level, while many weaker signals, as well as signals near 65-70°S and 160-110°W are not.

### 3. Main results

Kristjánsson (2002) found the indirect forcing to be negative everywhere, and much larger in the northern ( $-2.61 \text{ W/m}^2$ ) than in the southern ( $-1.06 \text{ W/m}^2$ ) hemisphere, because of inter-hemispheric differences in anthropogenic emissions. The globally averaged radiative forcing was  $-1.83 \text{ W/m}^2$ . The direct forcing can be either positive or negative, due to competition between

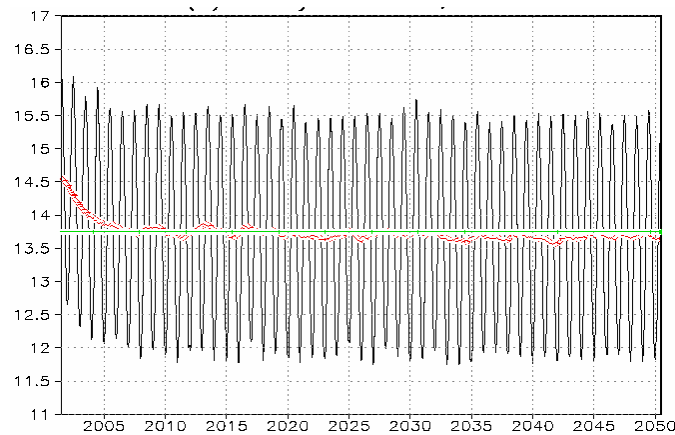


**Figure 1:** Variation in the globally averaged surface temperature, illustrating the 5-10 year spin-up and then a new quasi-equilibrium.

absorbing aerosols (e.g., BC) and reflecting aerosols (e.g.,  $\text{SO}_4$ ). Furthermore, the albedo of the underlying surface is important, as the effect of absorbing aerosols is larger over reflective underlying surfaces than over absorbing surfaces. Kirkevåg and Iversen (2002) found a globally averaged forcing of  $-0.11 \text{ W/m}^2$ , but with values ranging from  $+1.1 \text{ W/m}^2$  over the biomass burning regions, to  $-1.1 \text{ W/m}^2$  in air masses dominated by sulfate at mid-latitudes.

The average value in the Northern Hemisphere was  $-0.19 \text{ W/m}^2$ , while the Southern Hemisphere value was  $-0.04 \text{ W/m}^2$ . At the surface, the globally averaged forcing was more negative, i.e.,  $-0.60 \text{ W/m}^2$ , because aerosols that absorb solar radiation reduce solar radiation impinging on the surface (e.g., Ramanathan et al., 2001).

### 3.1 Temperature response and non-linear feedback

Figure 2a shows the simulated temperature change due to the indirect effect alone, while figure 2b shows the corresponding result for the direct effect. The indirect effect causes a globally averaged cooling of  $-1.28 \text{ K}$ , corresponding to a climate sensitivity of  $0.7 \text{ K per W/m}^2$ . Even though the negative radiative forcing is most pronounced in the low to mid-latitudes of the northern hemisphere and is quite weak in the Arctic, the cooling effect is largest in the Arctic. This is due to ice-albedo feedback, and is reminiscent - apart from the sign - to what has been found in simulations of global warming due to increased greenhouse gas concentrations. We have not made an extensive investigation of whether this feedback mechanism is of the right amplitude in our model, but we note that this result is similar to those obtained in the Hadley Centre GCM (Williams et al., 2001) and the Australian CSIRO model (Rotstayn and Lohmann, 2002). In addition to the ice-albedo feedback, there is a positive cloud feedback that amplifies the Arctic signal. This is seen by investigating the water path (liquid + ice) in the two simulations. It turns out (Figure 3) that this quantity is significantly reduced in the Arctic in the colder climate, hence contributing to further cooling, since clouds at those latitudes tend to have a warming (longwave) effect, due to the low sun angle. The fact that the NCAR CCM3 overestimates low clouds in the Arctic during winter (Rasch and Kristjánsson, 1998) may amplify this effect.

The temperature response due to the direct effect (Figure 2b) is much weaker than from the indirect effect, because of the weaker forcing. Although the cooling effect dominates, there are in this case also regions of statistically significant warming. In particular this can be ascribed to BC aerosols above high-albedo surfaces such as low clouds or deserts, e.g., off the coast of Namibia and over eastern Australia. In the direct effect simulations, the ice-albedo feedback in the Arctic is much less pronounced than it was for the indirect effect. The reasons are probably both that the globally averaged net negative radiative forcing is much weaker, and that locally in the Arctic the direct radiative forcing is slightly positive due to BC over the

highly reflective ice and snow. The globally averaged cooling effect in this case is  $-0.10$  K, which would correspond

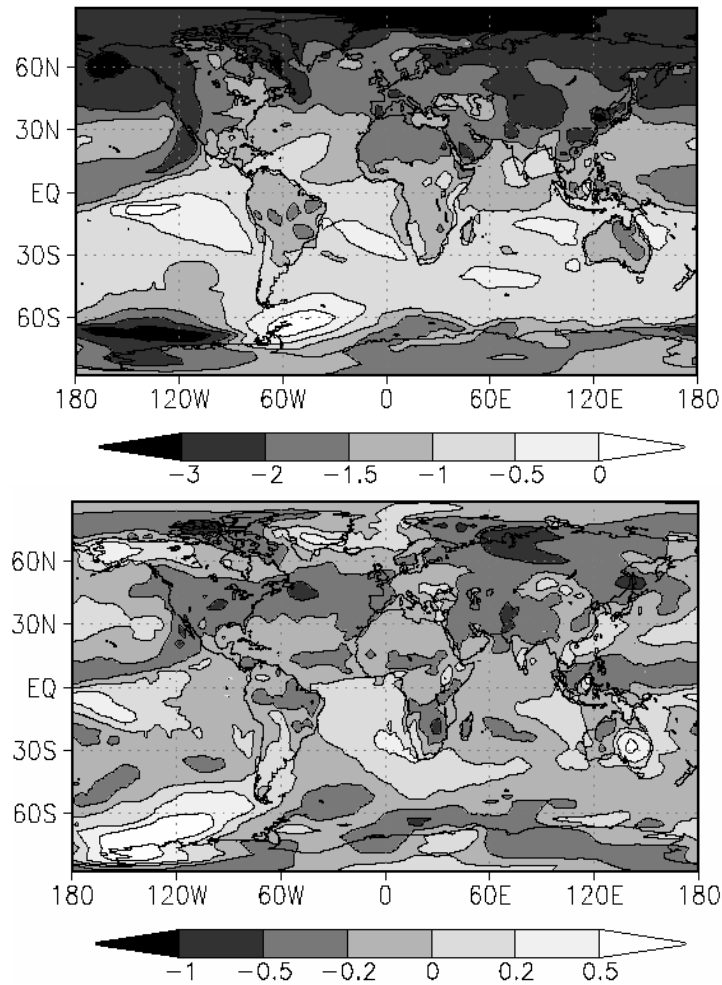


**Figure 2:** Simulated near-surface temperature change due to aerosol forcing. a) Indirect effect. b) Direct effect.

to a rather large climate sensitivity of  $1.0$  K per  $\text{W}/\text{m}^2$ . This may be partly related to the aforementioned difference in forcing magnitude between the top-of-the atmosphere and the surface, and partly to the fact that the direct forcing pattern has pronounced regional contrasts.

### 3.2 Underpinning the ice-albedo feedback

A set of sensitivity experiments in which the ice-albedo feedback was spuriously suppressed by setting the albedo over sea ice to equal that over ocean, gave a different geographical distribution of the cooling effect, with enhanced cooling in regions of large negative radiative forcing and reduced cooling over the Arctic (Figure 4). Nevertheless, the globally averaged

cooling was almost as large as in the simulations with the ice-albedo feedback included. Hence, the Arctic ice-albedo feedback does not influence the global climate sensitivity in our case, but mainly causes a geographical redistribution of the regional response patterns.

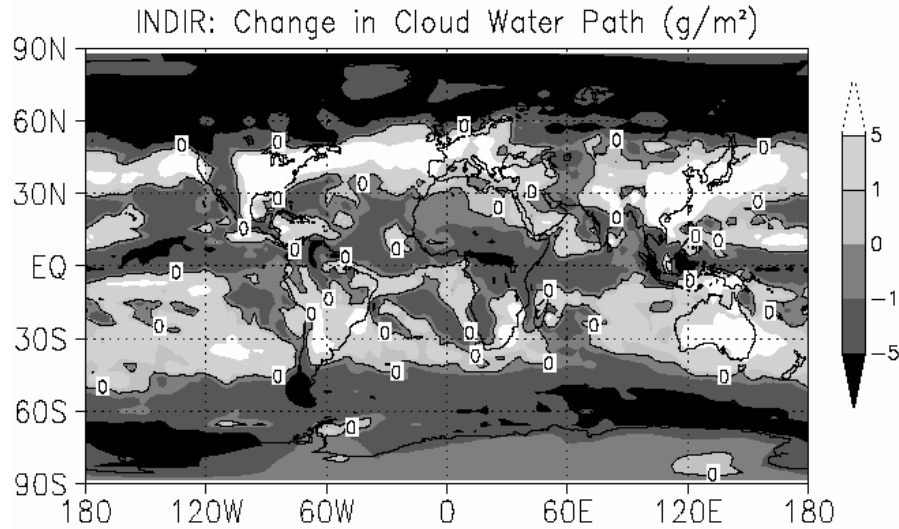


**Figure 3:** Change in integrated cloud water path (liquid + ice) due to indirect effect. Units:  $\text{g/m}^2$ .

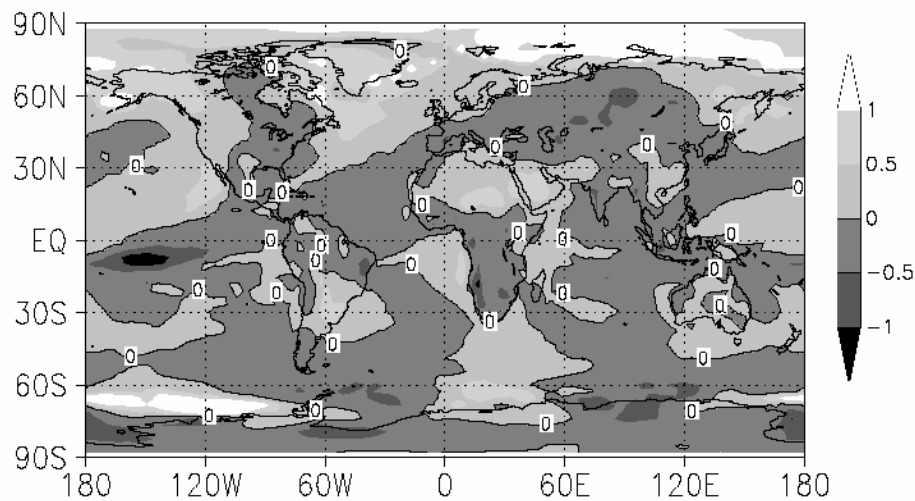


**Figure 4:** Change in temperature response due to indirect effect when ice-albedo feedback is suppressed. Units: K.

### 3.3 Precipitation response

Figure 5 shows the changes in precipitation due to the aerosol forcing. The indirect effect (Figure 5a) gives a strong and coherent signal, its main features being a southward displacement of the intertropical convergence zone (ITCZ) by a few degrees of latitude and some regional changes, e.g., a drying over much of North Africa. Both these features resemble the findings of Rotstayn et al. (2000), Williams et al. (2001) and Rotstayn and Lohmann (2002). The reason for the ITCZ displacement is the large inter-hemispherical difference in radiative cooling, and there are strong signals of this shift also in other variables, e.g., longwave cloud forcing and cloud fraction. The drying over North Africa was discussed in detail by Rotstayn and Lohmann (2002), who went on to suggest that the Sahelian drought in the 1970s and 1980s might have been largely caused by aerosol induced cooling, rather than by natural variability or soil water feedback due to overgrazing, as had previously been suggested. After 1985 or so, sulfate aerosol concentrations over North America and Europe have decreased significantly (Lelieveld et al., 2002), hence bringing precipitation in Sahel back to near-normal conditions, assuming that this hypothesis is correct (Leon Rotstayn, pers. comm.).

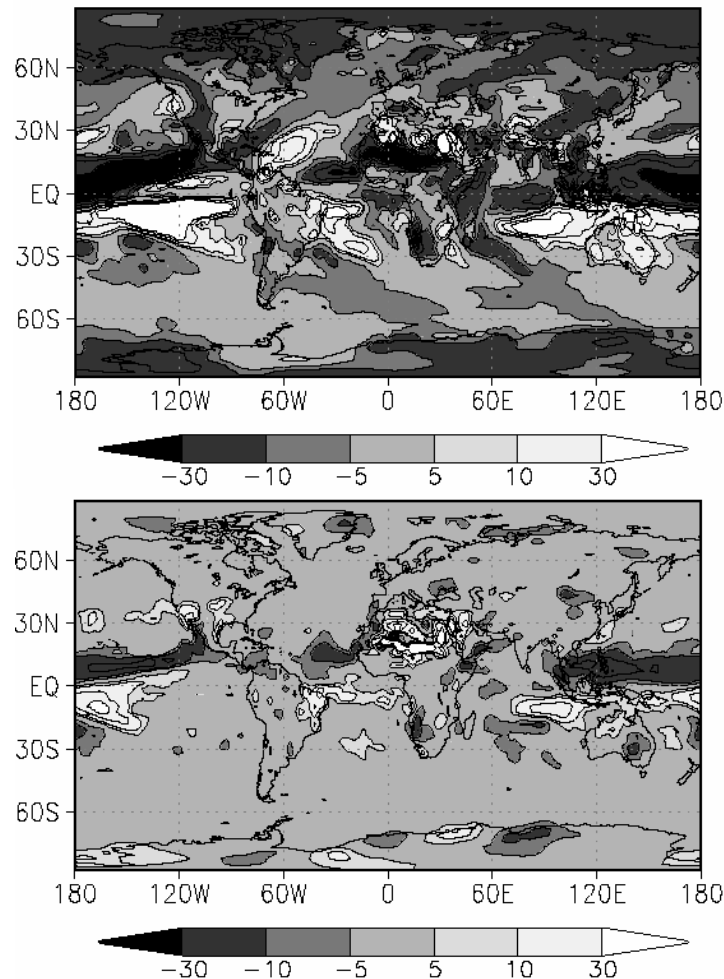


**Figure 5:** Simulated relative change in precipitation (%) due to aerosol forcing. a) Indirect effect. b) Direct effect.

There is a general reduction in precipitation, mainly because of the colder climate, but also due to the second indirect effect. The indirect effect also produces significant changes in extratropical regions such as over western parts of North America. Over Northern Europe there are also weak regional signals which physical relevance needs to be further studied by regional downscaling. Even though the inter-hemispheric cooling difference is much weaker for the direct than the indirect effect, a statistically significant southward shift of the ITCZ is produced also in this case (Figure 5b). Elsewhere, the precipitation signal from the direct effect is weak and largely insignificant.

### 3.4 Surface pressure

As a result of the aerosol forcing, there are significant changes in sea-level pressure, especially due to the indirect effect. The main change (Figure 6) is a 1-2 hPa increase in sea-

level pressure over the Arctic, most pronounced in the autumn and early winter. The cooling in this region is largest in the winter, even though the radiative forcing is strongest in summer (Kristjánsson, 2002). What apparently happens is that the reduction in summer insolation leads to increased sea ice extent, hence reducing the heat flux from the ocean to the atmosphere. As a result, a shallow anticyclone tends to form, blocking the intrusion of low-pressure systems that would normally have brought warm air masses towards the Arctic in the fall and early winter.

### **3.5 Indirect effect combined with greenhouse gas warming**

In order to realistically simulate historical climate variations, one needs to consider several forcing factors, i.e., changes in greenhouse gas concentrations, changes in tropospheric and stratospheric (volcanic) aerosol amounts, changes in stratospheric ozone amounts, etc. It is beyond the scope of this study to include all these effects. However, to get a first-order impression of how realistic our aerosol simulations are, we have carried out simulations in which both aerosol concentrations and greenhouse gas concentrations were varied between pre-industrial and present-day values.

In a globally averaged sense, these simulations give qualitatively the expected results with a global warming of 0.26 K and a noticeable increase in precipitation. However, annually averaged, the northern hemisphere experiences a net cooling and a net drying (Figure 7). This seems to suggest that, at least in the Northern Hemisphere, the cooling due to the indirect effect is exaggerated in our simulations. Varying greenhouse gas concentrations and keeping aerosols fixed gives a globally averaged warming of 1.54 K, corresponding to a climate sensitivity of 0.66 K per  $\text{W/m}^2$ , similar to what was obtained for the indirect effect alone. Hence, the Northern Hemisphere cooling that we see in Figure 7 is probably caused by the indirect forcing and not non-linearities associated with, e.g., changes in sea ice amount or thickness.

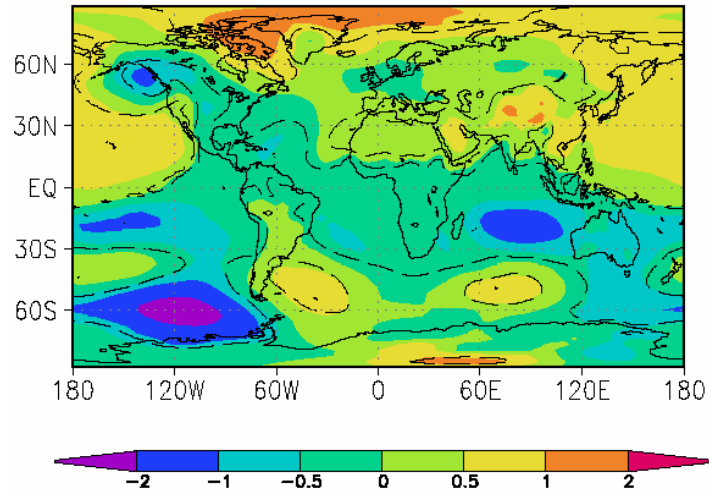


**Figure 6:** Simulated change in surface pressure (hPa) due to indirect aerosol forcing. Areas within dashed lines are statistically significant at the 95% level.

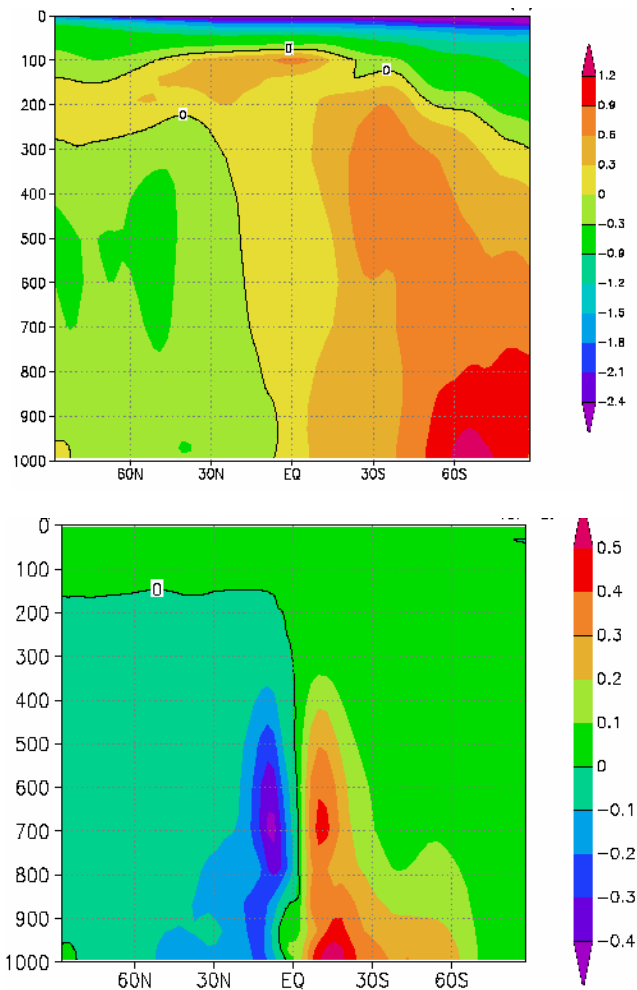


**Figure 7:** Simulated zonally averaged changes due to forcing from anthropogenic greenhouse gases and indirect effect of aerosols: a) Change in temperature (K). b) Change in specific humidity (g/kg).

It remains to be seen whether feedback from the dynamics on the aerosol distribution may reduce the indirect response. Other possible explanations include: a) Competition for water vapor between sea salt and sulfate aerosols in heavy wind conditions (O'Dowd et al., 1999) over the ocean is currently not taken into account; b) Vertical transport of aerosols by deep moist convection is neglected (Iversen and Seland, 2002), probably leading to too large concentrations of sulfate at levels where water clouds are located; c) The impact on the CCN population of sulfate produced through wet-phase processes may be overestimated in our calculations.

#### **4. Concluding remarks**

Through the simulations conducted so far, we have demonstrated that anthropogenic sulfate and black carbon aerosols may have had a substantial impact on temperature and precipitation distributions in the 20<sup>th</sup> century. A similar conclusion was recently drawn from an observationally-based study by Schneider and Held (2001), who found a considerable summertime cooling over the Northern Hemisphere continents in the 20<sup>th</sup> century in their analysis.

As mentioned in the last section, there are indications that our indirect cooling effect is too strong, at least in the Northern Hemisphere. This will be investigated carefully in the near future in RegClim in cooperation with the AerOzClim and COMBINE projects, supported by the Research Council of Norway. Also, in the near future, the simulations presented here will be repeated with the aerosol life-cycle model interactive, yielding more realistic interactions between the meteorology and climate dynamics on the one hand, and the aerosol production, transport, and deposition on the other.

#### **References**

- Hansen, J., Lacis, A., Rind, D., Russell, G., Stone, P., Fung, I., Ruedy, R., and Lerner, J., 1983. Climate sensitivity: analysis of feedback mechanisms in climate processes and climate sensitivity. *Geophysical Monograph*, **29**, 130.
- Iversen, T., and Seland, Ø., 2002. A scheme for process-tagged SO<sub>4</sub> and BC aerosols in NCAR-CCM3. Validation and sensitivity to cloud processes. *J. Geophys. Res.* **107**, (D24), 4751, doi:10.1029/2001JD000885.

- Kiehl, J. T., Hack, J. J., Bonan, G. B., Boville, B. A., Briegleb, B. P., Williamson, D. L., and Rasch, P. J., 1996. *Description of the NCAR Community Climate Model (CCM3)*. NCAR Technical Note, NCAR/TN-420+STR, 152 pp.
- Kiehl, J. T., Hack, J. J., Bonan, G. B., Boville, B. A., Williamson, D. L., and Rasch, P., 1998. The National Center for Atmospheric Research Community Climate Model: CCM3. *J. Climate*, **11**, 1131-1149.
- Kirkevåg, A., and Iversen, T., 2002. Global direct radiative forcing by process-parameterized aerosol optical properties. *J. Geophys. Res.* **107**, (D20), 4433, doi:10.1029/2001JD000886.
- Kristjánsson, J. E., 2002. Studies of the aerosol indirect effect from sulfate and black carbon aerosols. *J. Geophys. Res.* **107**, (D15), 4246, doi:10.1029/2001JD000887.
- Lelieveld, J., and co-authors, 2002. Global air pollution crossroads over the Mediterranean. *Science*, **298**, 794-799.
- Levitus, S., 1982. *Climatological atlas of the world ocean*. NOAA Professional paper 13.
- O'Dowd, C. D., Lowe, J. A., Smith, M. H., and Kaye, A. D., 1999. The relative importance of non-sea-salt sulphate and sea-salt aerosol to the marine cloud condensation nuclei population: An improved multi-component aerosol-cloud droplet parameterization. *Q. J. R. Meteorol. Soc.*, **125**, 1295-1313.
- Ramanathan, V., Crutzen, P. J., Kiehl, J. T., and Rosenfeld, D., 2001. Aerosols, climate and the hydrological cycle. *Science*, **294**, 2119-2124.
- Rasch, P. J., and Kristjánsson, J. E., 1998. A comparison of the CCM3 model climate using diagnosed and predicted condensate parameterisations. *J. Climate*, **11**, 1587- 1614.
- Rotstayn, L. D., Ryan, B. F., and Penner, J. E., 2000. Precipitation changes in a GCM resulting from the indirect effects of anthropogenic aerosols. *Geophys. Res. Lett.*, **27**, 3045-3048.
- Rotstayn, L. D., and Lohmann, U., 2002. Tropical rainfall trends and the indirect aerosol effect. *J. Climate*, **15**, 2103-2116.
- Schneider, T., and Held, I. M., 2001. Discriminants of twentieth-century changes in earth surface temperature. *J. Climate*, **14**, 249-254.
- Williams, K. D., Jones, A., Roberts, D. L., Senior, C. A., and Woodage, M. J., 2001. The response of the climate system to the indirect effects of anthropogenic sulfate aerosol. *Climate Dyn.*, **17**, 845-856.



# Optimal Forcing Perturbations for the Atmosphere

by

Trond Iversen<sup>1</sup>, Jan Barkmeijer<sup>2</sup> and Tim N. Palmer<sup>3</sup>

<sup>1</sup>) Department of Geosciences, University of Oslo, Norway

<sup>2</sup>) Royal Dutch Meteorological Institute, De Bilt, The Netherlands

<sup>3</sup>) European Centre for Medium-Range Weather Forecasts, Reading, United Kingdom

## Abstract

We generalize the adjoint of the tangent-linear model for atmospheric developments to forcing adjoints, singular vectors to forcing singular vectors, and sensitivities to forcing sensitivities. Thus instead of finding optimal initial state perturbations, optimal forcing perturbations that are constant over some optimization interval are estimated. We have used the T21 3-level quasi-geostrophic model of Marshall and Molteni (1993) to calculate forcing perturbations that in different ways are optimal over 5 days. Forcing perturbations that optimally alter the atmospheric flow over 5 days can be important for climate change. 5 days is a longer time than typical for transitions between quasi-permanent atmospheric flow patterns defined from monthly data, and time-slots with high forcing sensitivity are typically 5 days or shorter. In response to an external forcing that intermittently project onto forcing sensitivity patterns, the preference of quasi-permanent flow patterns may be altered and thus climate will change globally and regionally. Optimal forcing perturbations such as forcing singular vectors have larger scales, do not evolve upscale, and is less remotely controlled than optimal initial state perturbations. These results need to be confirmed with full-scale atmospheric GCMs and with oceanic feedbacks investigated.

*To be submitted for publication, please do not quote or cite.*

## 1 Introduction

Deterministic weather prediction (of the first kind, Lorenz (1975)) is limited by the fundamental divergence of states in the climate system phase space (Lorenz, 1963). The situation is caused by intrinsic instabilities present under governing planetary conditions. Climate scenarios are predictions of the second kind, for which the initial conditions by definition are irrelevant. Changes in the probability density function (pdf) for climate state variables are predicted in response to perturbed external forcing. Palmer (1999) suggested a conceptualization of climate change which implies that considerable changes in the pdf can be forced by small perturbations to which the atmosphere is intermittently sensitive. The idea is that sensitivity is predominantly lower when the system is in quasi-permanent states or in predictable transitions between them (Palmer, 1996), than during intermittent transitions characterized by highly diverging states. Quasi-permanent and predictable transitions are relative terms that refer to states in the climate system for which growth rates of small perturbations are relatively small. Variations in growth rates with respect to actual states follow from nonlinearities in the climate system (Palmer, 1993). During the relatively infrequent time-slots when sensitivity is high, small perturbations may alter the selection of subsequent quasi-permanent states and thus the pdf. The time used for transitions between quasi-permanent flow regimes depends on which compartments of the climate system are involved, but it is typically considerably shorter than the residence time of the flow regimes. A switch between zonal and blocked flows in the mid-latitude atmosphere may occur during a few days (Rex, 1950; Lejenäs and Økland, 1983; Kanestrøm *et al.* 1985, Blackmon, 1976). For coupled flow regimes like ENSO the time-scale may be weeks to a few months (Moore and Kleeman, 1999), and switches off and on of the oceanic overturning thermohaline circulation may take decades.

In this paper we study perturbations that efficiently change northern hemispheric winter-time atmospheric flows. Based on results of Oortwijn and Barkmeijer (1995), Corti and Palmer (1997), and earlier studies of atmospheric flow regimes, we assume 5 days as a time-range for extratropical flow switches. Atmospheric climate change may stem from a perturbed radiation balance or lower boundary conditions, although the latter can be feedbacks triggered by the atmosphere itself. With a simple global circulation model for the atmosphere, Corti and Palmer (1997) showed that the relative occurrence of flows with a high Pacific-North-

American (PNA) index can be efficiently increased by perturbing the forcing with a pattern proportional to the average over a large sample of 5-day tangent-linear adjoints (Talagrand and Courtier, 1987) applied to the PNA flow-pattern. Similar results are inferred for the North-Atlantic Oscillation (NAO) pattern. They used the same T21 3-level quasi-geostrophic model (T21L3QG) of the global atmosphere developed by Marshall and Molteni (1993) as we have used in the present paper, and showed that state perturbations that efficiently trigger transitions to a flow pattern do not necessarily resemble the flow pattern itself. This is a consequence of the non-normality of the tangent-linear equations, and similar results were found by Oortwijn and Barkmeijer (1995) for northern hemispheric blocking.

The adjoint of the tangent-linear propagator over a time interval  $[0, T]$  applied to a selected state of the climate system such as a quasi-permanent flow pattern, is an estimate of the most efficient way to perturb the initial state (at time 0) in order to produce a maximum projection onto the flow pattern at final time  $T$ . We shall generalize the sensitivity with respect to initial state perturbations to sensitivity with respect to forcing. There are several ways to do this (Moore and Kleeman, 1999; Barkmeijer *et al.*, 2003). We estimate a constant forcing over  $[0, T]$  that yields maximum state projection onto the flow pattern at time  $T$ , by applying the adjoint of the integral of all tangent linear propagators that start any time  $t$  in  $[0, T]$  and end on  $T$ , to the state pattern.

Flow pattern sensitivities constitute a manifestation of the instabilities present in the climate system. The degree of divergence of state developments can also be studied independently of any predefined flow patterns. Keeping the assumption of tangent-linearity, singular vectors and associated singular values are useful tools. As for sensitivity patterns, singular vectors can be defined for initial conditions or for forcing. Singular vectors (SVs) are orthogonal initial perturbations (at time 0) that are ranked according to their norm in a target domain after tangent-linear evolution over the interval  $[0, T]$  (e.g. Buizza, 1994; Molteni *et al.* 1996). Just as for sensitivities, we generalize SVs to forcing singular vectors (FSVs) by defining orthogonal forcing perturbations that are constant over  $[0, T]$  in stead of initial perturbations.

Even though anthropogenic climate forcing can be sufficiently modest to defend use of tangent-linear theory to estimate optimal forcing patterns, errors in the climate models and

their boundary conditions may be considerably larger and cause wrong feedbacks (e.g. IPCC (2001), p430). Some studies even indicate that this problem should be further addressed also in weather forecasting (Orrel et al, 2001). Numerical truncation and misrepresentation of forcing terms in atmospheric global climate models (AGCMs) may distort instability properties and lead to different perturbation growth than in the real atmosphere. In weather prediction, the preliminary experience from using forcing sensitivity to correct 2-day forecasts by Barkmeijer *et al.* (2003) indicates that correcting for potential model forcing errors has a larger impact than correcting potential initial errors. This emphasizes the need for model improvements. However, since the successful method is entirely based on tangent-linearity, substantial properties of large-scale instability mechanisms are well replicated in the ECMWF IFS model.

We will summarize findings from the calculations of FSVs and forcing sensitivities using the simple T21L3QG-model developed by Marshall and Molteni (1993). The QG-model's forcing terms have so far only been determined for northern hemispheric winters, and our results are only applicable to such atmospheric flows. FSVs and forcing sensitivities are calculated for daily fields analyzed at ECMWF for 6 recent winters (December through February defines each winter). Results are compared with regular SVs and initial sensitivities respectively. The model represents global atmospheric dynamics simplistically, but due to the forcing-residual procedure of Roads (1987) realistic internal low-frequency variability is produced. However, instability mechanisms and associated growth rates are probably biased, and results needs to be further investigated with full AGCMs such as the ECMWF IFS. Some preliminary results for 2-day FSVs were presented in Barkmeijer *et al.* (2003). An even further step is to study optimal forcing perturbations in coupled climate models. Due to the large differences in time-scales between atmospheric and oceanic dynamics this is yet an unresolved problem that deserves attention.

Forcing perturbations are not entirely connected with predictions of the second kind. Inadvertent misrepresentations of atmospheric processes in numerical models cause errors in weather forecasts in similar ways as initial state errors (e.g. Palmer, 2001). Inaccurate atmospheric forcing thus produces forecast spread that grows (Houtekamer *et al.*, 1996; Buizza *et al.*, 1999; Mylne *et al.*, 2002; Barkmeijer *et al.*, 2003). Modern weather forecasting

predicts forecast uncertainty and risks of extreme events. Prediction spread originates from imperfections in initial values, boundary values, and model forcing.

## 2 Forcing Adjoint and Forcing Singular Vectors and Values

Consider a nonlinear system of deterministic equations that are first order in time, written in matrix form as

$$\frac{d\mathbf{x}}{dt} = \mathbf{M}(\mathbf{x}) + \mathbf{F} \quad (1)$$

$\mathbf{M}$  are internal and  $\mathbf{F}$  external forcing terms, and  $\mathbf{x}(t)$  are time-dependent state variables. Note that  $\mathbf{F}$  encompasses boundary conditions that define the spatial extension of the physical system.

Assume that  $\mathbf{X}(t)$  is a solution (a “trajectory”) that satisfy initial conditions  $\mathbf{X}(0)$ . The system’s predictability is characterized by the rate at which trajectories close to  $\mathbf{X}(0)$  diverge from  $\mathbf{X}(t)$  as  $t$  increases, and the time elapsed from  $t=0$  until the time when divergence averaged over a large number of realizations vanishes (the predictability limit). Taking into account that numerical models are imperfect, this definition can be extended to include divergence between model trajectories and true trajectories that start from identical initial states  $\mathbf{X}(0)$ . The same extension applies for trajectories both starting in  $\mathbf{X}(0)$  but exposed to slightly different forcing.

### 2.1 Singular vectors extended to forcing

With the mentioned extension in mind, the linear stability of  $\mathbf{X}$  with respect to perturbations in forcing ( $\delta\mathbf{F}$ ) as well as initial conditions ( $\delta\mathbf{x}(0)$ ) are investigated, where  $\delta\mathbf{F}$  can represent model errors and changes in external forcing. The tangent-linear model is then:

$$\frac{d}{dt} \delta\mathbf{x} = \mathbf{J}\delta\mathbf{x} + \delta\mathbf{F}; \quad \text{where} \quad \mathbf{J} = \left[ \frac{d\mathbf{M}}{d\mathbf{x}} \right]_{\mathbf{x}=\mathbf{X}(t)} \quad (2)$$

The validity of the tangent-linear model is limited by the size of excluded non-linear terms. If  $\delta\mathbf{F}$  is large this may occur quickly even if  $\delta\mathbf{x}(0)=0$ . Due to advection terms,  $\mathbf{J}$  is a non-normal matrix:  $\mathbf{J}^* \mathbf{J} \neq \mathbf{J}\mathbf{J}^*$ , where  $\mathbf{J}^*$  is the adjoint with respect to an inner product, which implies that  $\langle \mathbf{J}\mathbf{x}, \mathbf{y} \rangle \equiv \langle \mathbf{x}, \mathbf{J}^* \mathbf{y} \rangle$  for any  $\mathbf{x}$  and  $\mathbf{y}$ . Non-normality means that eigenvectors of  $\mathbf{J}$  (normal modes) are not orthogonal. The norm of  $\delta\mathbf{x}(t)$  may then grow over finite time intervals  $[0, T]$ , even in cases when the norms of normal modes all decrease (Farrel and Ioannou, 1996). Suppose that  $\delta\mathbf{F}$  is constant over  $[0, T]$ . The solution to (2) can then be expressed as

$$\delta\mathbf{x}(T) = \mathbf{R}(T, 0)\delta\mathbf{x}(0) + \mathfrak{R}(T, 0)\delta\mathbf{F};$$

$$\text{where } \mathbf{R}(T, 0) = \exp\left\{\int_0^T \mathbf{J} dt\right\}, \text{ and } \mathfrak{R}(T, 0) = \int_0^T \mathbf{R}(T, t) dt \quad (3)$$

Assume first that  $\delta\mathbf{F} = 0$  and that we wish to find the perturbation  $\boldsymbol{\xi}(0)$  of unit length at time 0 that maximizes the norm of the perturbation  $\boldsymbol{\xi}(T)$  evolved tangent-linearly to time  $T$  according to (3). Since  $\mathbf{R}^* \mathbf{R}$  is a positive definite hermitian operator, we get

$$\|\boldsymbol{\xi}(T)\|^2 = \langle \mathbf{R}\boldsymbol{\xi}(0), \mathbf{R}\boldsymbol{\xi}(0) \rangle = \langle \mathbf{R}^* \mathbf{R} \boldsymbol{\xi}(0), \boldsymbol{\xi}(0) \rangle = \sigma^2, \quad (4)$$

where  $\boldsymbol{\xi}(0)$  is the eigenvector of  $\mathbf{R}^* \mathbf{R}$  with maximum eigenvalue  $\sigma^2$ . All eigenvalues, their square root being the *singular values*, are distinct and positive, and the eigenvectors, *the singular vectors*, are orthogonal. They can be ordered according to the size of the singular values:  $\boldsymbol{\xi}_i(0)$  and  $\sigma_i$ . Singular vectors are used routinely at e.g. ECMWF to construct initial perturbations for ensemble weather prediction from approximately equally valid initial conditions (e.g. Buizza *et al.* 1993).

Assume instead that  $\delta\mathbf{x}(0)=0$  and we seek the unit length constant forcing pattern,  $\boldsymbol{\varepsilon}$ , that maximizes the norm of the resulting state-vector perturbation  $\boldsymbol{\xi}(T)$  at the optimization time  $T$ :

$$\|\boldsymbol{\xi}(T)\|^2 = \langle \mathfrak{R}\boldsymbol{\varepsilon}, \mathfrak{R}\boldsymbol{\varepsilon} \rangle = \langle \mathfrak{R}^* \mathfrak{R}\boldsymbol{\varepsilon}, \boldsymbol{\varepsilon} \rangle = s^2 \quad (5)$$

where  $\boldsymbol{\varepsilon}$  now is the eigenvector of the positive definite hermitian operator  $\mathfrak{R}^*\mathfrak{R}$  with maximum eigenvalue  $s^2$ . The operator  $\mathfrak{R}^*$  is the *forcing adjoint*, and the orthogonal eigenvectors  $\boldsymbol{\varepsilon}_i$  are called *forcing singular vectors* and the corresponding  $s_i$  the *forcing singular values*.

## 2.2 Sensitive perturbations extended to forcing

One aspect of a notoriously unstable and non-linear dynamical system is that the divergence of adjacent state trajectories varies across the attractor (e.g. Palmer, 1993). States in regions of phase space with modest divergence are less unstable than others and likely to be associated with quasi-persistent flow patterns. Flow patterns normally show up by suitable time-averaging and time-correlation between states at separate geographical areas (teleconnections; Wallace and Gutzler, 1981). The concept is frequently used in geophysical fluid dynamics, and we do not address the fundamental question to what extent the concept is physically sound.

An interesting question is to what extent transitions to and from the flow patterns can be altered by initial state perturbations. The answer has a consequence for the predictability of the onset or decay of the flow patterns. For the atmosphere this was addressed by Oortwijn and Barkmeijer (1995) and by Corti and Palmer (1997) using the adjoint of the flow patterns over finite time-intervals. If a perturbed forcing efficiently can trigger such transition changes, the climate in regions influenced by the flow patterns can change considerably. In this case the forcing adjoint may be used to estimate the sensitivity with respect to forcing, but the climate response in the form of changed relative occurrence of the flow patterns must be investigated non-linearly.

Let  $\mathbf{P}$  be a state vector that defines a flow pattern as a deviation from some average development (e.g. a seasonal cycle). We want to maximize the projection  $\Delta$  of the perturbed state vector with a specified norm valid at time  $T$  on  $\mathbf{P}$ , given that the system's evolution is  $\mathbf{X}(t)$  over the interval  $[0, T]$ .

$$\Delta = \langle \delta \mathbf{x}(T), \mathbf{P} \rangle \quad (6)$$

To achieve this by perturbing only the initial state and keeping the forcing terms unchanged, we get  $\Delta = \langle \mathbf{R} \delta \mathbf{x}(0), \mathbf{P} \rangle = \langle \delta \mathbf{x}(0), \mathbf{R}^* \mathbf{P} \rangle$ . Hence *the initial sensitivity* of  $\mathbf{P}$  over  $[0, T]$  is:

$$S_I = \frac{\|\mathbf{R}^* \mathbf{P}\|}{\|\mathbf{P}\|}, \quad (7)$$

see Corti and Palmer (1997). This is easily generalized to *forcing sensitivity*:

$$S_F = \frac{\|\mathfrak{R}^* \mathbf{P}\|}{\|\mathbf{P}\|} \quad (8)$$

The vectors  $\delta \mathbf{x}(0) = \alpha \mathbf{R}^* \mathbf{P}$  and  $\delta \mathbf{F} = \alpha \mathfrak{R}^* \mathbf{P}$  are initial and forcing sensitivity patterns respectively. The coefficient  $\alpha$  is chosen in order to achieve a desired norm of the tangent linearly evolved sensitivity patterns:  $\|\mathbf{R} \delta \mathbf{x}(0)\|$  for initial sensitivity and  $\|\mathfrak{R} \delta \mathbf{F}\|$  for forcing sensitivity.

### 3 Singular Vectors

As described in the introduction, we use the T21L3QG of Marshall and Molteni (1993). Daily estimates of SVs, FSVs, and sensitivities are made for six consecutive winter seasons December through February, starting with 1995/96 and ending with 2000/01. This comprises 542 daily results.

The structure of the perturbations and growth of their norm depend of the unperturbed non-linear development ( $\mathbf{X}(t)$ ), the length of the time interval ( $[0, T]$ ), and the inner product that

defines the perturbation norm ( $\|\xi\| = \langle \xi, \xi \rangle^{1/2}$ ). In the T21L3QG model, long-term perturbation growth can only occur to the extent that the model represent the dynamics behind combined barotropic and baroclinic instability typical for large-scale extra-tropical atmospheric flows. Systematic errors in quasi-geostrophic theory are due to neglected ageostrophic and vertical advection. The properties of the singular vectors are influenced both by this, by the simplified forcing terms which neglect important tropical dynamics, and by numerical truncation in the T21L3QG model.

### 3.1 Basic properties

Figure 1 shows the RMS of leading FSVs and SVs for the 542 winter days based on the kinetic-energy inner product without targeting, i.e.  $\langle \psi, \psi \rangle$  is proportional to the global kinetic energy. The energy amount involved in baroclinic-barotropic instability is larger in the winter hemisphere, and the patterns in figure 1 are thus almost confined to the northern hemisphere. The two sets of tangent-linearly evolved vectors ( $\xi(T)$ ) have very similar patterns with a maximum over the Northern Pacific Ocean that extends westwards over the Asia and further to Northern Africa. A secondary maximum extends over North America and the North Atlantic Ocean. The amplitude increases with height. Initially, however, the FSVs ( $\epsilon$ ) and SVs ( $\xi(0)$ ) differ in many respects. Both amplitudes peak in the mid-troposphere, but whilst SVs dominate over central and North-East Eurasia, maxima for the FSVs occur over the North Pacific and North Atlantic Oceans. Regions close to Himalaya are origins for perturbation growth in both cases. Figure 2 indeed confirms that energy spreads upwards from mid-troposphere to upper levels. Spectrally, the SVs develop upscale from small to large scales over the optimization interval, in contrast to the consistently large-scale FSVs. Also the evolved FSVs are slightly larger in scale than SVs.

Singular values are the ratios between the norm of evolved and initial singular vectors. The degree of instability, measured by singular values, clearly varies with the actual flow (Figure 3). The high covariance shows that the flow dependent instability is similarly diagnosed by the two types of singular values, but the values differ considerably more for SVs than for FSVs. More interesting is the relatively short duration and rare occurrence of situations with large singular values. This supports the perception that the atmosphere is only intermittently susceptible to small perturbations. Unstable flow change may occur abruptly and

unpredictable, although significant flow change also may occur when predictability is higher (Corti and Palmer, 1997).

Figure 4 shows a composite over days with the 5% highest singular values, of the basic flow ( $\mathbf{X}(t)$ ) as streamfunction anomalies relative to the 6-winters average. At final time (T=5 days, lower panels) the basic flow is similar for the high SV days and the high FSV days. Negative anomalies occur over northern North America, Eurasia and the Pacific Ocean. Positive anomalies are seen over the European - North Atlantic sector, over the ocean south-west of Alaska, and over Japan (in the case of high FSVs). The positive anomalies are reminiscent of anticyclone blocking, and similar anomalies are also present at initial time. Due to the relatively little activity for SVs in the Western Hemisphere, the basic flow in that region should not be interpreted as significant for the development. At initial time over areas where SVs peak (see Figure 1), there are weaker westerly winds than average, indicating weak baroclinicity in the basic flow for the most unstable cases. This may appear as a contradiction, but is related to the fact that when baroclinicity is high in the basic flow, the development is large in the first place. When baroclinicity is low, however, there is little development in the basic flow and a well-designed perturbation (i.e. a leading SV) can make a considerable difference. In areas where initial FSVs peak, there are only small anomalies in the basic flow, but adding forcing (e.g. heating or cooling) in the subtropics of the Northern Hemisphere may effectively change the baroclinicity of the westerly flows at mid-latitudes.

### **3.2 Remote vs. local forcing of regional climate**

In order to prepare for regional impact studies, improved spatial resolution by downscaling of climate change scenarios from GCMs is now common (Giorgi *et al.* (2001)). One approach is to run limited area atmospheric models with higher resolution over the region than in the GCMs, using data from the coarse-resolution global calculations as driving conditions at open lateral boundaries.

Since FSVs are large-scale with minor upscale development, large-scale forcing processes need to be improved in order to correct errors in e.g. North Atlantic storm tracks, which influence wind and precipitation climates in Northern Europe. The relative importance of

remote versus local forcing determines the required size of the integration domain that influences the climate in a target area. If the regional climate is mainly locally controlled, improving the large-scale forcing processes in a limited area is potentially beneficial. Otherwise little improvement beyond local adjustment to better geographical detail can be expected. It remains to investigate the local vs. remote forcing control, and we provide a first approach using the FSVs over 5 days. We are less worried by the possibility that the regional model's climate may deviate from that of the GCM, than several other authors (e.g. Jones *et al.*, 1995; Kida *et al.*, 1991; Denis *et al.*, 2002).

Here we only discuss pure atmospheric dynamical adjustment to improved forcing. We emphasize, though, that it is not straightforward to improve large-scale forcing structures in a region, and probably coupled regional models with high resolution of the ocean and sea-ice components are needed. IPCC (2001) documented that the simulated climate over the North Atlantic Ocean and in the Arctic by GCMs has a considerable spread. Pure atmospheric downscaling can not significantly reduce this overall uncertainty. For GCMs with reasonable present-climate North-Atlantic SST and sea-ice, however, resolution-based improvements of baroclinic disturbances and of pure atmospheric processes associated with clouds and precipitation, should have a positive impact. Nevertheless, without the possibility to improve SST and sea-ice, reduction of crucial errors in features like the North Atlantic storm-tracks will be limited. Very few regional climate models include the possibility to improve oceanic and sea-ice dynamics. Such models are designed to improve large-scale atmospheric forcing, but their potential success is still not known.

In order investigate the feasibilities of improved atmospheric forcing in regional climate models, we have run 5-day SVs and FSVs for 6 winters with a local projection operator (Buizza, 1994) that ensures the evolved singular vectors to have maximal norms in a target region. Our target is Northern Europe and a sector of the adjacent North Atlantic Ocean, and Figure 5 show the results for targeted SVs and FSVs. Many features are similar to Figure 1. The perturbations start in the mid-Atmosphere and develop upwards; at final time ( $t=T$ ) SVs and FSVs are similar, but they are initially ( $t=0$ ) very different. The initial SVs peak over North-East North America, indicating that perturbing initial conditions in that region effectively trigger baroclinic instability: The FSVs, on the other hand, point to forcing

perturbations over the North Atlantic Ocean as effective. Hence, the climate control by small changes in forcing appears not particularly remote, and much less than would be inferred from regular SVs. Based on these quasi-geostrophic estimates there should be a potential for improvement in the target region if forcing features over the North Atlantic Ocean is better described.

Also in the case of targeted singular vectors, the basic flow ( $\mathbf{X}(t)$ ) anomaly patterns associated with the 5% leading SVs and FSVs are similar at final time ( $t=T$ ). Initially, however, the basic flow differs considerably (Figure 6), with that for the FSVs having considerably larger scales. In this case the activities are large over the North Atlantic Ocean due to the targeting, and we focus the attention to that sector. Both basic flows have blocking-type anomalies at final time, whilst initially there are dipole patterns indicating weaker than normal westerly winds over north-western parts of the North Atlantic Ocean where initial SVs peak. This is in principle the same as found for the basic flows of untargeted singular vectors.

## 4 Flow Pattern Sensitivities

The sensitivity pattern to a spatial flow pattern is either the adjoint (the initial sensitivity; eq. 7) or the forcing adjoint (the forcing sensitivity; eq. 8) of the pattern divided by its norm. It depends on length of the optimization interval and the basic state trajectory. As for the singular vectors we use 5-day optimization, use the T21L3QG model, and calculate daily results for 6 winters.

### 4.1 Flow Regimes

We use the flow patterns defined by de-trended monthly anomalies of the 500 hPa geopotential heights fields by Corti *et al.* (1999). The flow patterns are extended to the three pressure levels used in the global QG-model. This is done by using the daily projections of normalized 500 hPa anomalies onto the normalized flow regimes as expansion coefficients for the anomaly fields in the 200 and 800 hPa levels. Only days when the absolute value of the 500 hPa projections exceed 0.5 (i.e angle smaller than  $60^\circ$ ) are included. For the sake of consistency also the 500 hPa patterns are thus re-constructed, and they differ slightly from the original. Finally, the norm is adjusted so that the norm of the northern hemispheric 500 hPa

anomaly equals the norm of the original anomaly. Figure 7 shows the present flow patterns in 500 hPa generalized from the original Corti *et al.* (1999) 500 hPa patterns. We have alternatively generalized the flow patterns by linear regression of the geo-potential height anomaly in any point with the 500 hPa flow projection, with similar results.

#### 4.2 Linear sensitivities to initial conditions and forcing

We focus our attention to flow patterns A (NAO and COWL-indices positive) and D (AO-index negative). Both these patterns are associated with recent climate trends. It can be shown that pattern A in Figure 7 is correlated with higher temperature anomalies in the atmospheric boundary layer over continents than over oceans in the Northern Hemisphere. Thus it is named Cold Ocean Warm Land or simply COWL (Wallace *et al.* 1996).

Corti *et al.* (1999) demonstrated that pattern A occurred more and pattern D less frequently over the period 1971-94 compared to 1949-71. It is therefore particularly interesting to estimate the forcing sensitivity of these two patterns. Figure 8 shows the initial and forcing sensitivity patterns for flow patterns A and D averaged over the 5% (27) most sensitive cases. Whilst initial sensitivity patterns are relatively small scaled, the forcing sensitivity patterns are more reminiscent of the original flow patterns. The initial sensitivity patterns are more confined to the lower and middle troposphere and the Eastern (for pattern A) and Western (for pattern D) Hemisphere. The forcing pattern is more evenly spread. Furthermore, the forcing patterns for patterns A and D are of opposite sign in several regions, whilst the initial patterns have very little resemblance to each other. A forcing that favor transition to pattern A tends to hamper transition to pattern D.

As found by Corti and Palmer (1997) the flow pattern index has a considerably slower variability than both the initial and the forcing sensitivity (Figure 9). Similar to singular values, the sensitivities are moderate to low most of the time and high only intermittently. Provided a forcing perturbation has a considerable positive (negative) projection onto the sensitivity pattern, transitions to (from) the flow pattern is probable when sensitivity is high. When the sensitivity is low or moderate, larger projections are needed to force transition. Figure 9 also shows that on several occasions the QG model predicts 5-day transitions when the sensitivity is high (e.g. day 510 for pattern A; day 242 for pattern D). Shifts also occur

with low sensitivity (day 67 for pattern A; day 30 for pattern D). Furthermore, transitions do not necessarily occur when sensitivity is high. Actual transitions during high sensitivity also require an appreciable projection onto the sensitivity pattern. There is therefore no clear relation between sensitivity and actual transition.

A necessary requirement for the validity of the sensitivity patterns is that the response produced by non-linear integration of the quasi-geostrophic model is close to the flow pattern. For initial sensitivity, the sensitivity pattern is added to the initial conditions. For forcing sensitivity initial conditions are unchanged and forcing terms are incremented with the forcing sensitivity. The amplitude of the sensitivity patterns are chosen so that a tangent-linear evolution yields the norm of the flow pattern. Results for the 5% most sensitive cases are given in Figure 10. The match with the original flow patterns is close in both cases, but slightly better for the evolved forcing sensitivities. This is confirmed by Figure 11, which shows the projection of the normalized evolved sensitivity pattern on the normalized flow pattern for each day. For initial sensitivity the average value is about 0.3 and for forcing sensitivity it is 0.4 but there are considerable variations from day to day.

Figure 12 shows composites of mid-atmospheric streamfunction anomalies for the time-dependent basic flow ( $X(t)$ ) during the 5% most sensitive dates for flow patterns A and D. The basic flow at the end of the 5-day interval tends to be spatially anti-correlated with the respective flow pattern. This is more pronounced for flow pattern A than for D. The basic flow at initial time ( $X(0)$ ) have little resemblance with the flow patterns, and the anomalies during cases with high initial sensitivity are very similar to those associated with high forcing sensitivity. Since there is a considerable temporal correlation between the associated sensitivity values, many of the days are common.

#### **4.3 On limitations posed by non-linearity**

An important question to address when using adjoints is to what extent tangent-linear theory is valid. We seek perturbations that optimally trigger flow pattern transitions over 5 days. This is not by nature a linear problem, but our method to estimate these perturbations are linear. One way to investigate the errors introduced by linearity is to evolve the sensitivity patterns

both nonlinearly and tangent-linearly and compare the results. The quality increases with decreasing difference.

The degree of nonlinear behavior depends strongly on the amplitudes of the perturbations in the state variables. We have chosen two values for the amplitudes of the sensitivity patterns of A and D. One yields the same norm after tangent-linear evolution as the original flow pattern, and the other a 4 times larger norm. We measure the degree of nonlinearity by the norm of the difference between the normalized tangent-linear evolution and the normalized nonlinear evolution. When the nonlinear model behaves perfectly linearly this value is zero. This quantity does not measure the nonlinear effects on the norm of the evolved patterns. This effect is not as serious as the effect on phase-space direction, since the result is perfect to a constant factor if the direction in phase-space is correct.

Figure 13 shows that the nonlinear model behaves quasi-linearly for the original flow pattern amplitudes. Nonlinearity is less pronounced for forcing sensitivity than for initial sensitivity. Our flow patterns have amplitudes representative of monthly data. Oortwijn and Barkmeijer (1995) calculated initial sensitivities for a blocking-pattern anomaly that typically lasts between 1 and 3 weeks. They found nonlinearity to be important for optimization times longer than 3 days, and designed an iterative procedure to extend the optimization into nonlinearity. By multiplying our flow patterns A and D with 4, the amplitudes are more typical for weekly time-scales. However, the patterns would not emerge from an eof-analysis of weekly data, so this test is purely to check the robustness of the quasi-linearity found for original amplitudes. In this case, nonlinearity is important, but tangent-linearity still is approximately valid for forcing sensitivities.

## 5 Discussion and Conclusions

Based on the results Corti and Palmer (1997) and the conceptualization of climate change put forward by Palmer (1999), we have advocated that forcing perturbations that optimally alter the atmospheric flow over 5 days can be important for climate change. We have seen that 5 days is a longer time than the typically needed for transition between quasi-permanent atmospheric flow patterns defined from monthly data. We have also seen that the atmosphere

is sensitive to forcing perturbations during time-slots of 5 days or shorter. Depending on the spatial pattern and temporal variation of an actual external forcing perturbation in relation to forcing sensitivity patterns associated with flow patterns, flow pattern transitions can be triggered during such short time-slots. In response to this, the atmospheric flows will show other long-term flow patterns than without the external forcing perturbation. Thus the pdf of atmospheric states, and thus climate, is changed. To the extent that the quasi-permanent flow patterns have significant regional signatures, regional climate change may differ considerably from the global average. We have not made a long-term climate experiment with a forcing perturbation based on an average over a large set of forcing sensitivities, but such a run was successfully made by Corti and Palmer (1997) using the same model and forcing perturbation based on 5-day initial sensitivity patterns. Here we have only calculated nonlinear 5-day integrations based on forcing sensitivities, and these result in even more efficient 5-day flow pattern transitions than using initial sensitivities. We have also seen that the developments are quasi-linear for pattern amplitudes representative for monthly data.

Our forcing sensitivity patterns resemble the flow pattern more than initial sensitivity patterns. The integral of the tangent-linear propagators that start from any time in  $[0, T]$  and end on  $T$ , is probably closer to normality than the single propagator from 0 to  $T$ . Another signature of the same is the larger spatial scales of the forcing sensitivity patterns than the initial sensitivity patterns. This is further emphasized by the forcing singular vectors which are both less remote and develop less upscale than regular singular vectors.

To the extent that the linearity of singular vectors are approximately valid for physical amplitudes of forcing perturbations, and the QG results can be generalized to full atmospheric physics and dynamics, the potential consequence for regional climate models are positive. If means to improve large-scale forcing patterns over the North Atlantic Ocean are provided, the climate in the region and in Northern Europe can be improved by regional climate models. Coupled regional climate modeling with improved resolution and description of oceanic and sea-ice processes should have good prospects for downscaling of GCM-results. Pure atmospheric downscaling of results from GCMs that simulate present-day conditions in the North Atlantic Ocean and the Arctic, likewise has a considerable potential.

The use of a globally net radiative forcing of the global climate, and to compare contributions to this net forcing from different sources, is not consistent with the conceptual ideas of climate change inherent in this paper. If the different contributions to the radiative forcing have similar spatial structure and the sign of the forcing is predominantly the same in all areas, global values are comparable and meaningful. The main problem occurs when some contributions have considerably different spatial patterns than others, or have both signs. The projection of the radiative forcing onto forcing sensitivity may then vary between the contributions, and a contribution with zero net global radiative forcing may have a considerable forcing onto a sensitivity pattern and thus provoke both global and regional climate response.

Since we address the atmosphere only, external forcing is not only radiative forcing but also forcing from changes in the ground surface, including ocean, sea-ice and snow cover etc. These types of forcing perturbations are not entirely external, since they may partly result from feedback from atmospheric change. The QG model is too simplistic to be able to separate these two types of forcing, however. Our results are thus preliminary first tests of the calculations of optimal forcing patterns. The next step is to perform similar studies of forcing singular values and forcing sensitivities in a full AGCM. Further on, oceanic feedbacks need to be studied in a coupled GCM.

## **Acknowledgements**

This work was initiated during a one-year guest visit of T. Iversen at ECMWF supported by the Norwegian Research Council, University of Oslo, and The Norwegian Meteorological Institute. We are grateful to Dr. S. Corti who provided the flow patterns in digital form, and to Dr. T. Jung for valuable discussions.

## **References**

- Barkmeijer, J., Iversen, T. and Palmer, T. N. (2003) Forcing singular vectors and other sensitive model structures. *Quart. J. Roy. Meteor. Soc.*, **129**, 2401-2423.
- Blackmon, M. L. (1976) A climatological spectral study of the 500 mb geopotential height of the Northern Hemisphere. *J. Atmos. Sci.*, **33**, 1607-1623.

- Buizza, R. (1994) Localization of optimal perturbations using a projection operator. *Quart. J. Roy. Meteor. Soc.*, **120**, 1647-1681.
- Buizza, R., Tribbia, J., Molteni, F., and Palmer, T. (1993) Computations of unstable structures for a numerical weather prediction model. *Tellus*, **45A**, 388-407.
- Buizza, R., Miller, M. and Palmer, T. N. (1999) Stochastic representation of model uncertainties in the ECMWF ensemble prediction system. *Quart. J. Roy. Meteor. Soc.*, **125**, 2887-2908.
- Corti, S. and Palmer, T. N. (1997) Sensitivity analysis of atmospheric low-frequency variability. *Quart. J. Roy. Meteor. Soc.*, **123**, 2425-2447.
- Corti, S., Molteni, F. and Palmer, T. N. (1999) Signature of recent climate change in frequencies of natural atmospheric circulation regimes. *Nature*, **398**, 799-802.
- Denis, B., Laprise, R., Caya, D. and Côté, J. (2002) Downscaling ability of one-way nested regional climate models: the big-brother experiments. *Climate Dyn.*, **18**, 627-646.
- Farrell, B. F. and Ioannou, P. J. (1996) Generalised stability theory. Part II: Nonautonomous systems. *J. Atmos. Sci.*, **53**, 2042-2053.
- Giorgi, F., Hewitson, B., Chridtensen, J., Hulme, M., von Storch, H., Whetton, P., Jones, R., Mearns, L., and Fu, C. (2001): Regional climate information – Evaluation and projections. In: *Climate Change 2001: The Scientific Basis. Contribution of Working Group I to the Third Assessment Report of the Intergovernmental Panel of Climate Change*. Houghton, J.T., D.J. Griggs, M. Noguer, P.J. van der Linden, X. Dai, K. Maskell, and C.A. Johnson (eds.). Cambridge University Press, Cambridge, United Kingdom.
- Houtekamer, P. L., Lefaivre, L., Derome, J., Ritchie, H. and Mitchell, H. L. (1996) A system simulation approach to ensemble prediction. *Mon. Wea. Rev.*, **124**, 1225-1242.
- IPCC (2001) *Climate Change 2001: The Scientific Basis. Contribution of Working Group I to the Third Assessment Report of the Intergovernmental Panel of Climate Change*. Houghton, J.T., D.J. Griggs, M. Noguer, P.J. van der Linden, X. Dai, K. Maskell, and C.A. Johnson (eds.). Cambridge University Press, Cambridge, United Kingdom.
- Jones, R.G., Murphy, J.M. and Noguer, M. (1995): Simulation of climate change over Europe using a nested regional-climate model. I: Assessment of control climate, including sensitivity to location of lateral boundaries. *Q.J.R. Meteorol. Soc.*, **121**, 1413-1449.
- Kanestrøm I., Pedersen, K. and Skåtun, H. (1985) Major stationary ridges and troughs at 500 mb. *Geophysica Norvegica*, **33**, 1-40.
- Kida, H., Koide, T., Sasaki, H., and Chiba, M. (1991): A new approach to coupling a limited area model with a GCM for regional climate simulation. *J. Met. Soc. Japan*, **69**, 723-728.
- Lejenäs, H. and Økland, H. (1983) Characteristics of northern hemispheric blocking as determined from long time-series of observational data. *Tellus*, **35A**, 350-362.
- Lorenz, E. N. (1963) Deterministic nonperiodic flow. *J. Atmos. Sci.*, **20**, 130-141.
- Lorenz, E. N. (1975) Climate predictability: The physical basis for climate modeling. *WMO, GARP Pub. Ser.*, **16**, 132-136. WMO, Geneva, Switzerland.
- Marshall, J. and Molteni, F. (1993) Toward a dynamical understanding of planetary-scale flow regimes. *J. Atmos. Sci.*, **50**, 1792-1818.

- Molteni, F., Buizza, R., Palmer, T. N., and Petroliagis, T. (1996) The ECMWF ensemble prediction scheme: Meteorology and validation. *Quart. J. Roy. Meteor. Soc.*, 122, 73-119.
- Moore A. M. and Kleeman, R. (1999) Stochastic forcing of ENSO by the intraseasonal oscillation. *J. Climate*, **12**, 1199-1220.
- Mylne, K. R., Evans, R. E. and Clark, R. T. (2002) Multi-model multi-analysis ensembles in quasi-operational medium-range forecasting. *Quart. J. Roy. Meteor. Soc.*, 128, 361-384.
- Oortwijn, J. and Barkmeijer, J. (1995) Perturbations that optimally trigger weather regimes. *J. Atmos. Sci.*, **52**, 3932-3944.
- Orrell, D., Smith, L., Barkmeijer, J. and Palmer, T. N. (2001) Model error in weather forecasting. *Nonl. Processes in Geophys.*, **8**, 357-371.
- Palmer, T. N. (1993) A nonlinear dynamical perspective on climate prediction. *Weather*, 48, 313-348
- Palmer, T. N. (1996) Predictability of the atmosphere and oceans: from days to decades. In: *Decadal climate variability – dynamics and predictability*. NATO ASI Series, **44**, pp. 83-155.
- Palmer, T. N. (1999) A nonlinear dynamical perspective on climate prediction. *J. Climate*, **12**, 575-591.
- Palmer, T. N. (2001) A nonlinear dynamical perspective on model error: A proposal for non-local stochastic-dynamic parameterization in weather and climate prediction models. *Quart. J. Roy. Meteor. Soc.*, 127, 279-304.
- Rex, D. F. (1950) Blocking action in the middle troposphere and its effects upon regional climate – II. The climatology of blocking action. *Tellus*, 2, 275-301.
- Roads, J. O. (1987) Predictability in the extended range. *J. Atmos. Sci.*, **44**, 1228-1251.
- Talagrand, O. and Courtier, P. (1987) Variational assimilation of meteorological observations with the adjoint vorticity equation. Part I: Theory. *Quart. J. Roy. Meteor. Soc.*, **113**, 1311-1328.
- Wallace, J. M. and Gutzler, D. S. (1981) Teleconnections in the geopotential height field during the Northern Hemispheric winter. *Mon. Wea. Rev.*, **109**, 784-812.
- Wallace, J.M., Zhang, Y., and Bajuk, L. (1996) Interpretation of interdecadal trends in Northern Hemispheric surface air temperature. *J. Climate.*, **9**, 249-259.

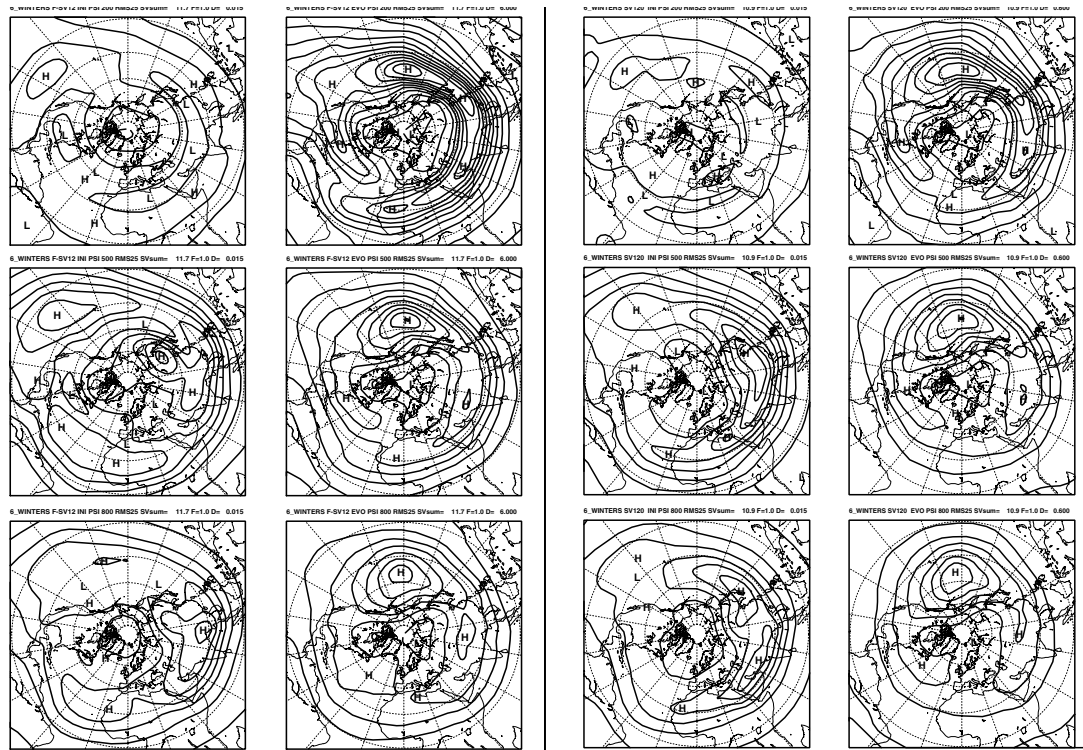


**Figure 1.** Columns 1 and 2 (from left) show initial and evolved FSVs, and columns 3 and 4 show initial and evolved SVs, for QG model levels 200 (top), 500 (middle), and 800 hPa (bottom). The figures show the RMS for the streamfunction  $\psi$  of the vectors belonging to the 25 largest singular values for each day in the 542 days of the six winters. Each normalized initial vector and each evolved vector is weighted with the associated singular value when calculating RMS. The inner product produces the global kinetic energy when applied to  $\psi$ , and there is no targeting.

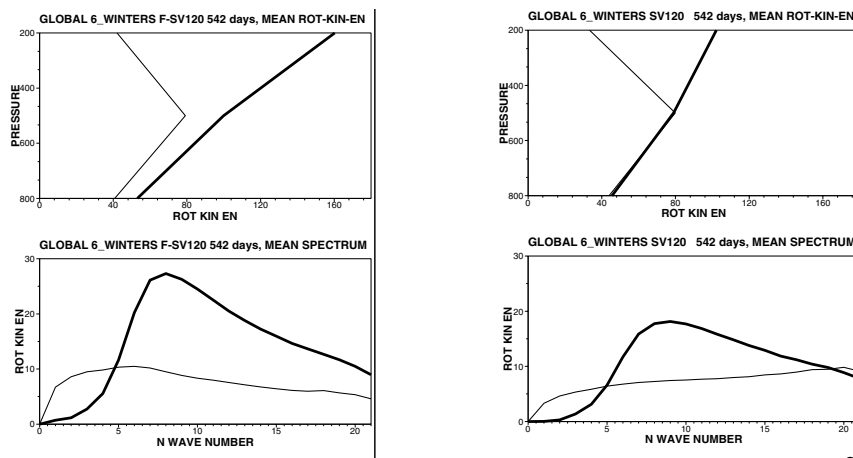


**Figure 2.** Vertical (upper) and spectral (lower) distribution of kinetic energy averaged over the 25 leading FSVs (left) and SVs (right). Thin lines are for initial vectors and thick lines for evolved. Kinetic energy is scaled and units are arbitrary. Only the shapes of the curves are relevant.

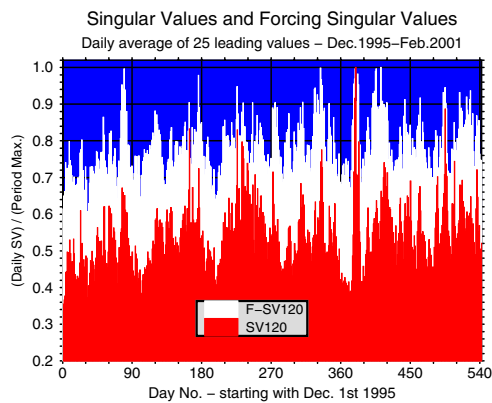


**Figure 3.** Daily average of the 25 leading singular values (red columns) and forcing singular values (white columns) for the 542 winter days, optimization time: 5 days and kinetic energy inner product without targeting. The values are normalized by the period maximum value in each case. Note that singular values vary more with respect to the flow situation than the forcing singular values.

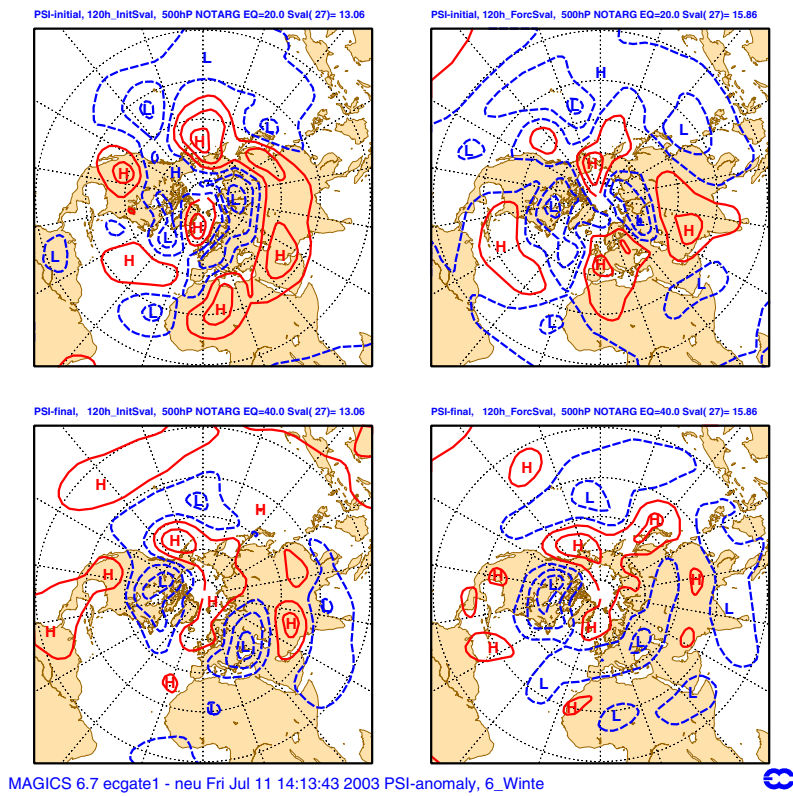


**Figure 4.** Composite of 500 hPa streamfunction ( $\psi$ ) anomaly for the 27 dates with 5% largest singular values without targeting, for initial conditions (left) and forcing (right). Upper panels are the analyzed fields for the actual dates ( $t=0$ , equidist. $=20 \cdot 10^5 \text{m}^2/\text{s}$ ), and lower panels are the  $t=5$  days non-linear forecasts by the QG-model (end of optimization interval, equidist. $=40 \cdot 10^5 \text{m}^2/\text{s}$ ).



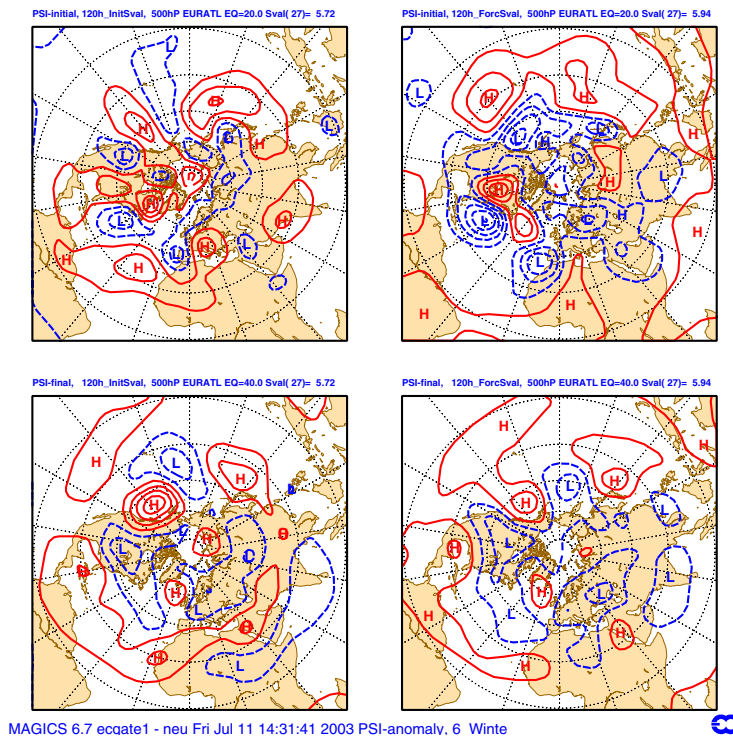


**Figure 6.** Same as Fig. 4, except that anomalies are calculated for the 27 dates with the 5% largest singular values, targeted to a region covering Europe and parts of the North-Atlantic Ocean.

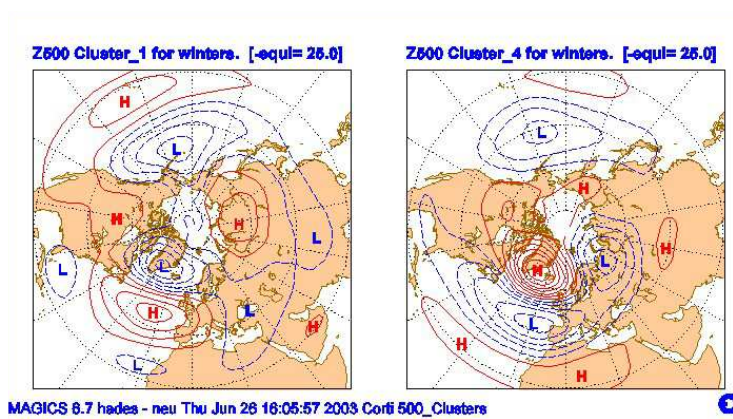


**Figure 7.** 500 hPa anomaly pattern for geopotential height for two of the four winter-time flow regimes generated from the patterns of Corti *et al.* (1999) for monthly averaged data. *Left:* flow pattern A associated with the Cold Ocean Warm Land (COWL) pattern and a positive index for the North Atlantic Oscillation. *Right:* flow pattern D with a negative index for the Arctic Oscillation.

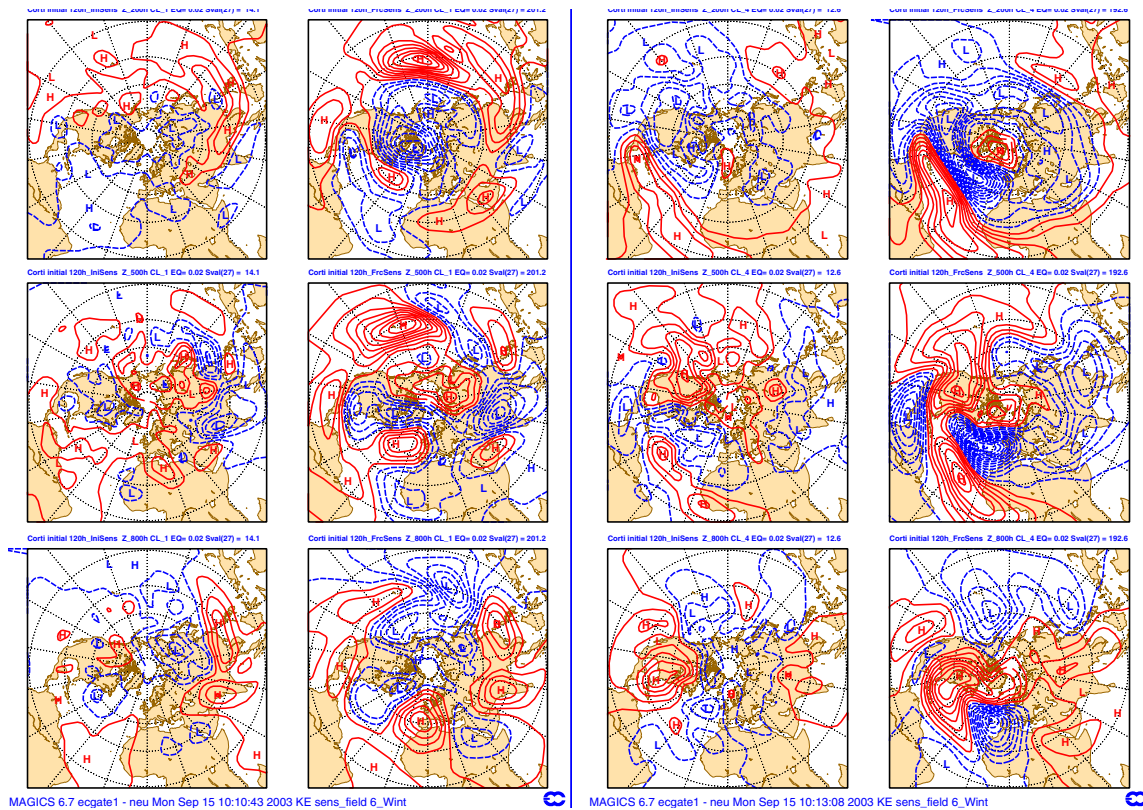


**Figure 8.** 5 day sensitivities w.r.t. kinetic energy inner product of flow patterns generalized from Corti et al. (1999). Anomalies in streamfunction  $\psi$  averaged over the 5% most sensitive dates (27 cases) are shown. Upper, middle and lower rows are 200, 500, and 800 hPa respectively. First column from left is initial sensitivity of pattern A, second is forcing sensitivity of pattern A, third column is initial sensitivity of pattern D, and fourth column is forcing sensitivity of pattern D. The sensitivity amplitude is chosen so that the norm of the tangent-linearly evolved pattern equals that of the flow pattern.

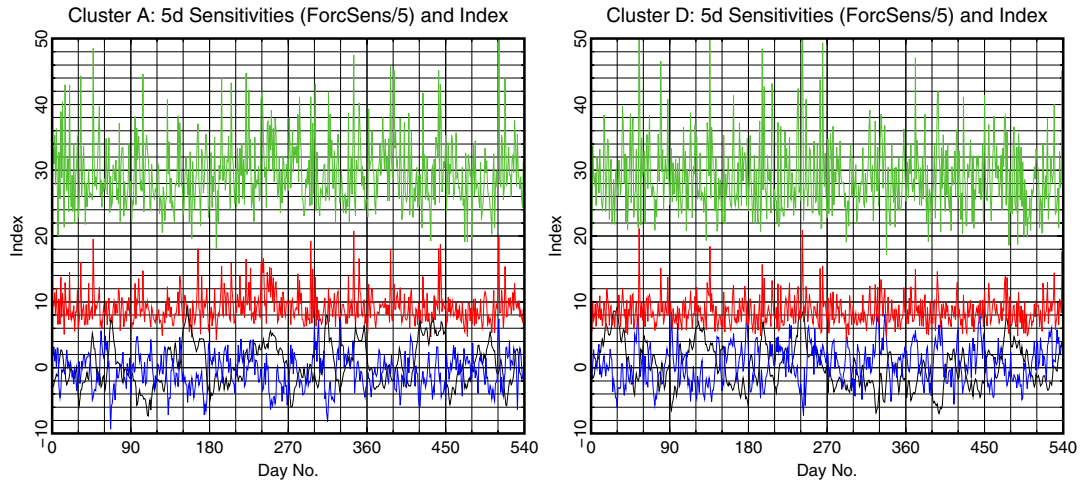


**Figure 9.** Daily values of 5-day forcing sensitivity (green, divided by 5) and initial sensitivity (red). Black line is the daily value of the flow pattern index estimated as the daily anomaly in streamfunction  $\psi$  projected onto the flow pattern by the kinetic energy inner product. The blue line is the 5-day change in the index calculated by the quasi-geostrophic model. *Left:* flow pattern A. *Right:* flow pattern D.

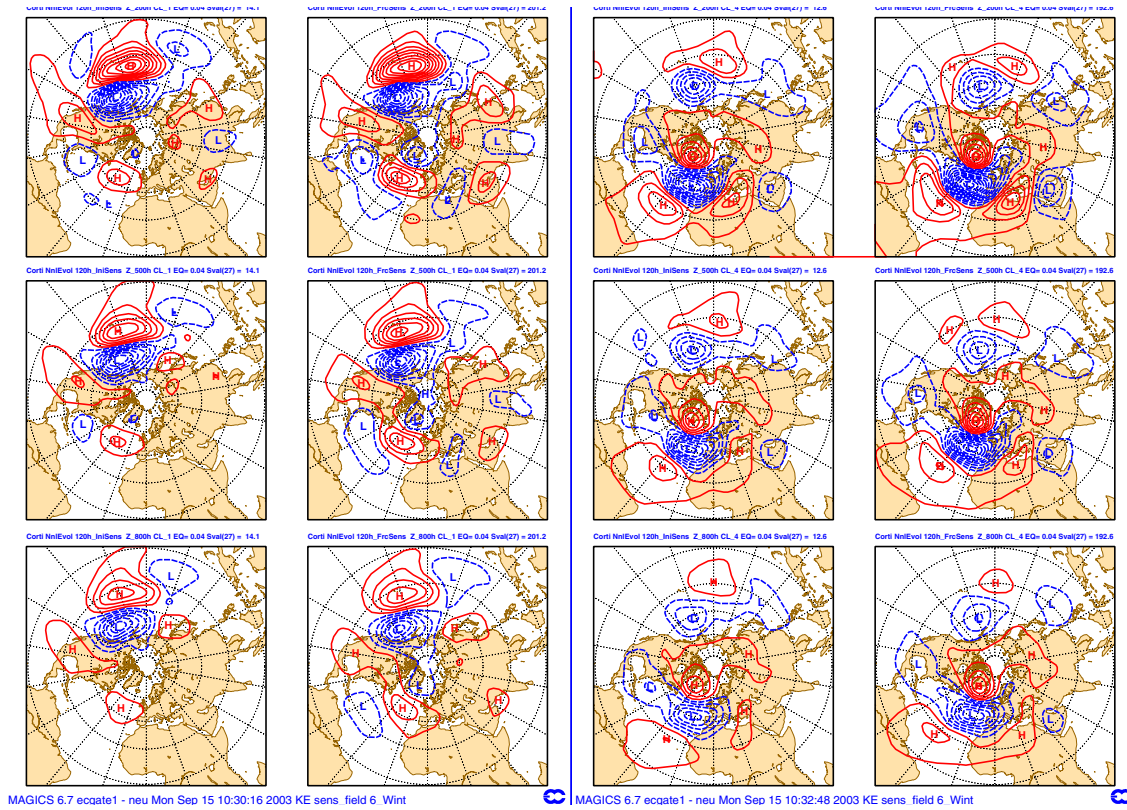


**Figure 10.** Panels similar to Fig. 8, except that these are the evolved sensitivities by the full non-linear QG model. Scales are determined so that the norm targeted to the NH is equal to the norm of the patterns.

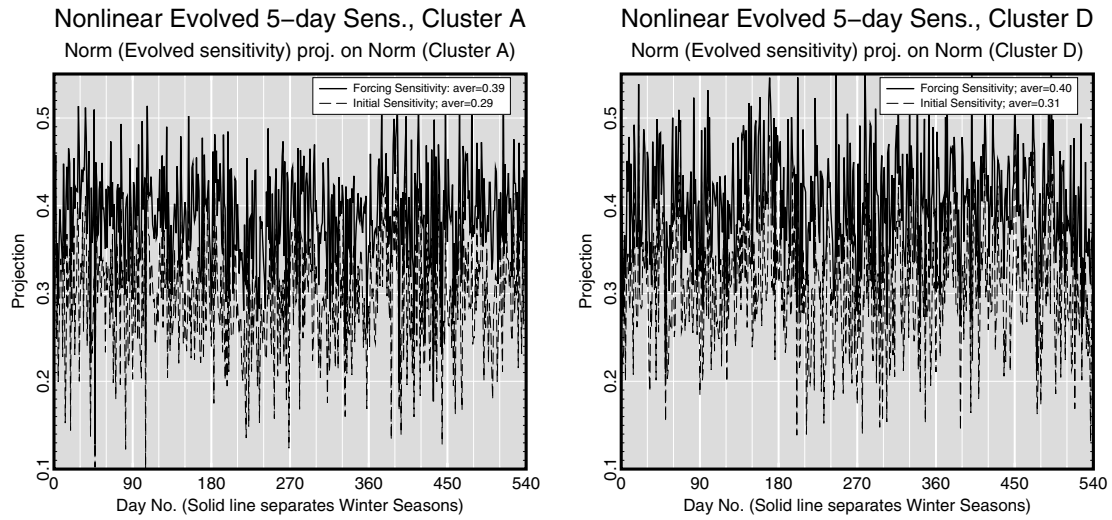


**Figure 11.** Daily values of the projection of the normalized evolved sensitivity pattern onto the normalized flow pattern. Continuous line is for forcing sensitivity and dashed for initial sensitivity. *Left:* flow pattern A; *Right:* flow pattern D.

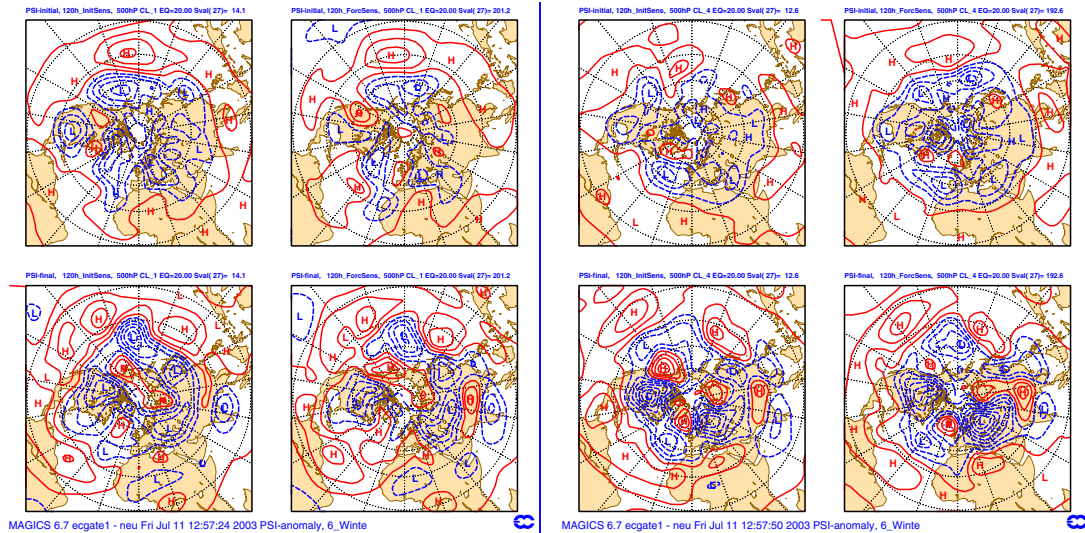


**Figure 12.** Nonlinear development of the regular QG-trajectories in phase space averaged over the 5% most sensitive of the 542 cases over 5 days. Only the 500 hPa streamfunction is shown. Upper row is for initial time whilst lower row is for time 5 days. First column from left is for the 27 largest initial sensitivity of flow pattern A, the second for forcing sensitivity of pattern D, the third for initial sensitivity of pattern D, and the fourth for forcing sensitivity of pattern D.

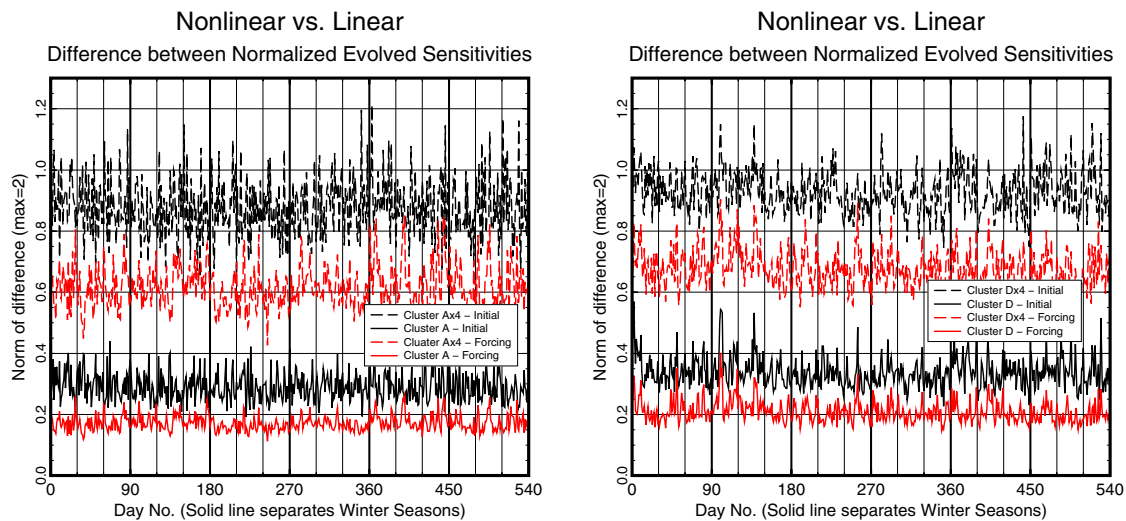


**Figure 13.** The degree of nonlinearity for flow patterns A (left) and D (right) of Corti *et al.* (1999) over the 5-day optimization time interval. For each day nonlinearity is estimated by the norm of the difference between the normalized nonlinear and the normalized tangent-linear evolution of the sensitivity patterns. 2 is maximum for which the two state vectors point in opposite directions. A value 1 corresponds to  $60^\circ$ , 0.77 to  $45^\circ$ , 0.52 to  $30^\circ$ , and 0.25 to  $14^\circ$ . Results for regular pattern amplitudes and quadrupled amplitudes are shown.



## **Appendix A**

### **Seminar Programme**



## RegClim Phase III Spring Seminar, 15-16 May 2003

University of Oslo,

Administration Building, 9<sup>th</sup> floor, BL 01-1003

### PROGRAMME

#### THURSDAY 15<sup>TH</sup> MAY 2003

13.00 – 14.00 Lunch at the Administration Building

14.00 – 14.10 Welcome and introduction  
Trond Iversen, University of Oslo

#### PM 3 – presentations:

14.10 - 14.25 "Status of PM3"  
Nils Gunnar Kvamstø, University of Bergen

14.25 – 14.45 "Sensitivity to the Atlantic Meridional Overturning  
Circulation"  
Asgeir Sorteberg, University of Bergen

14.45 – 15.10 " Evaluation of 3 model configurations with the NERSC  
version of MICOM"  
Helge Drange, Nansen Environmental and Remote  
Sensing Center

15.10 - 15.30 Coffee

#### PM 5 – presentation:

15.30 – 16.00 "Optimal forcing perturbations for the atmosphere"  
Trond Iversen, University of Oslo. Presented by Inger-  
Lise Frogner, Norwegian Meteorological Institute

#### Guest Lecture:

16.00 – 16.30 "Simulation of the last interglacial with the coupled  
ocean atmospheric circulation model ECHO-G and  
comparison with reconstructed data"  
Ulrich Cubasch, The Free University in Berlin, Germany

19.30 Dinner at „Restaurant Oriental“, Arbeidergata 2 (around  
the corner from the hotel)

**FRIDAY 16<sup>TH</sup> MAY 2003****PM 4 – presentations:**

- 09.00 – 09.10 “Progress report from PM4”  
Jon Egill Kristjansson, University of Oslo
- 09.10 – 09.30 “Climate response to anthropogenic aerosol forcing using the NCAR  
CCM3 coupled to a slab ocean”  
  
Alf Kirkevåg, University of Oslo

**PM 1 – presentations:**

- 09.30 – 09.45 “Overview of status within PM1”  
Eirik Førland, met.no
- 09.45 – 10.30 “Evaluation of MPI and Hadley simulations with HIRHAM, and  
sensitivity to integration domains”  
Jan Erik Haugen and Viel Ødegaard, met.no
- 10.30 – 10.50 Coffee
- 10.50 – 11.15 “An evaluation of the most recent A2 and B2 SRES  
climate scenarios from various GCMs.  
Rasmus Benestad, met.no
- 11.15 – 11.30 “Application of downscaled daily values of temperature  
and precipitation for water balance studies”  
Torill Engen Skaugen, met.no

**PM 2 – presentations:**

- 11.30 – 11.50 “Model setup and preliminary results for the North Sea  
shelf model”  
Bjørn Ådlandsvik, Institute of Marine Research
- 11.50 – 12.10 “Implementing an ice model in ROMS and basin scale  
simulations”  
Paul Budgell, Institute of Marine Research
- 12.10 – 12.30 Coffee
- 12.30 – 12.50 “Development of coupled ocean-ice system with  
MICOM/MI/IM (including improvements in  
thermodynamics and a new model domain)  
Jens Debernard, met.no
- 12.50 – 13.05 “Parameterization of sea ice albedo in climate models”  
Morten Ø. Køltzow, met.no

13.05 – 14.15 Lunch in the Administration Building

**Internal Meeting:**

14.15 – 16.00 **Project Leaders, PIs, and Scientific Advisory Group**

PIs:

to present a status compared to target schedule,  
scientific and technical problems,  
and propose results that deserve to be highlighted in a  
press release.

Advisory Group to comment on all aspects of RegClim.

Project Leader to conclude.

16.00 Adjourn



# **Appendix B**

## **List of Participants**



## Participants to RegClim Phase III Spring Seminar in Oslo 15-16 May 2003

Benestad, Rasmus Norwegian Meteorological Institute P.O.Box 43 Blindern, 0313 Oslo, Norway	E-mail: rasmus.benestad@met.no
Bjørge, Dag Norwegian Meteorological Institute P.O.Box 43 Blindern, 0313 Oslo, Norway	E-mail: dag.bjorge@met.no
Budgell, Paul Institute of Maritime Research P.O.Box 1870 Nordnes, 5817 Bergen, Norway	E-mail: paul.budgell@imr.no
Christensen, Ole Bøssing Danish Meteorological Institute, Danish Climate Centre Lyngby vej 100, DK-2100 Copenhagen, Denmark	E-mail: obc@dmi.dk
Cubasch, Ulrich Institute for Meteorology FU Berlin, Carl-Heinrich-Becker-Weg 6-10, D-12165 Berlin, Germany	E-mail: cubasch@zedat.fu-berlin.de
Debernard, Jens Norwegian Meteorological Institute P.O.Box 43 Blindern, 0313 Oslo, Norway	E-mail: jens.debernard@met.no
Drange, Helge Nansen Environmental and Remote Sensing Center Edv. Griegsv. 3A, 5059 Bergen. Norway	E-mail: helge.drange@nersc.no
Döscher, Ralf Swedish Meteorological and Hydrological Institute Folkborgvägen 1, 60176 Norrköping, Sweden	E-mail: ralf.doescher@smhi.se
Frogner, Inger Lise Norwegian Meteorological Institute P.O.Box 43 Blindern, 0313 Oslo, Norway	E-mail: inger.lise.frogner@met.no
Førland, Eirik Norwegian Meteorological Institute P.O.Box 43 Blindern, 0313 Oslo, Norway	E-mail: eirik.forland@met.no

Grønås , Sigbjørn  
University of Bergen, Geophysical Institute  
Allégaten 70, 5007 Bergen, Norway

E-mail: sigbjorn@gfi.uib.no

Hanssen-Bauer, Inger  
Norwegian Meteorological Institute  
P.O.Box 43 Blindern, 0313 Oslo, Norway

E-mail: inger.hanssen-bauer@met.no

Haugen , Jan Erik  
Norwegian Meteorological Institute  
P.O.Box 43 Blindern, 0313 Oslo, Norway

E-mail: jan.erik.haugen@met.no

Heino, Raino  
Finnish Meteorological Institute  
P.O.Box 503, FIN – 00101 Helsinki, Finland

E-mail: raino.heino@fmi.fi

Iversen , Trond  
University of Oslo, Institute of Geophysics  
P.O. Box 1022 Blindern, 0315 Oslo, Norway

E-mail: trond.iversen@geofysikk.uio.no

Kirkevåg, Alf  
University of Oslo, Institute of Geophysics  
P.O. Box 1022 Blindern, 0315 Oslo, Norway

E-mail: alf.kirkevag@geofysikk.uio.no

Kristjansson, Jon Egill  
University of Oslo, Institute of Geophysics  
P.O. Box 1022 Blindern, 0315 Oslo, Norway

E-mail: j.e.kristjansson@geofysikk.uio.no

Kvamstø, Nils Gunnar  
University of Bergen, Geophysical Institute  
Allégaten 70, 5007 Bergen, Norway

E-mail: nilsg@gfi.uib.no

Källen, Erland  
University of Stockholm, Arrheniuslaboratory  
SE-106 91 Stockholm, Sweden

E-mail: erland@misu.su.se

Køltzow, Morten Ødegaard  
Norwegian Meteorological Institute  
P.O.Box 43 Blindern, 0313 Oslo, Norway

E-mail: morten.odegaard@met.no

Lystad, Magne  
Norwegian Meteorological Institute  
P.O.Box 43 Blindern, 0313 Oslo, Norway

E-mail: magne.lystad@met.no

Martinsen , Eivind A.  
Norwegian Meteorological Institute  
P.O.Box 43 Blindern, 0313 Oslo, Norway

E-mail: eivind.martinsen@met.no

Røed, Lars Petter  
Norwegian Meteorological Institute  
P.O.Box 43 Blindern, 0313 Oslo, Norway

E-mail: lars.petter.roed@met.no

Seland, Øyvind  
University of Oslo, Institute of Geophysics  
P.O. Box 1022 Blindern, 0315 Oslo, Norway

E-mail: oyvind.seland@geofysikk.uio.no

Skaugen, Torill Engen  
Norwegian Meteorological Institute  
P.O.Box 43 Blindern, 0313 Oslo, Norway

E-mail: torill.engen.skaugen@met.no

Sorteberg, Asgeir  
University of Bergen, Geophysical Institute  
Allégaten 70, 5007 Bergen, Norway

E-mail: asgeir@gfi.uib.no

Wyser, Klaus  
Swedish Meteorological and Hydrological Institute, Rossby Centre  
Folkborgvägen 1, 60176 Norrköping, Sweden

E-mail: klaus.wyser@smhi.se

Ødegaard, Viel  
Norwegian Meteorological Institute  
P.O.Box 43 Blindern, 0313 Oslo, Norway

E-mail: viel.odegaard@met.no

Ådlandsvik, Bjørn  
Institute for maritime research  
P.O.Box 1870 Nordnes, 5817 Bergen, Norway

E-mail: bjorn@imr.no